POLITECNICO DI TORINO

Department of Mechanical and Aerospace Engineering

Master's Degree Thesis in Aerospace Engineering

Manipulation of a Turbulent Boundary Layer Through Plasma Actuators

Supervisors

Prof. Jacopo SERPIERI

Prof. Gioacchino CAFIERO

Ing. Edoardo FRACCHIA

Candidate

Luca PELLA

April 2026

Abstract

The global aviation industry currently faces the urgent challenge of mitigating its environmental impact by reducing pollutant emissions. One of the most effective strategies to minimize the carbon footprint of aircraft is the reduction of skin friction drag. It accounts for a significant portion of the total drag on commercial aircraft and it is intrinsically linked to the dynamics of the turbulent boundary layer.

A well-established technique for drag reduction, validated by both numerical simulations and experimental studies, is spanwise wall oscillation. Despite its potential, this technique remains challenging to implement in practical applications. Consequently, this thesis represents a continuation of an ongoing characterization project, focusing on two distinct approaches to emulate this technique through plasma actuators, which were custom-fabricated via manual deposition of conductive paint over laser-cut stencils.

The first approach consists of generating a time-dependent spanwise forcing using a three-electrode layout, while the second exploits a sinusoidal electrode geometry to generate a standing wave. The experimental campaign was conducted at the 'M. Panetti' Aeronautics Laboratory of Politecnico di Torino. It involved stereoscopic PIV measurements in cross-flow at several locations relative to the actuator: specifically, at the minimum/maximum and at the mid-point of the sinusoid, as well as approximately 1000 viscous units downstream of the actuator's trailing edge. Furthermore, measurements were carried out at three different free-stream velocities, investigating both the Reynolds number effect and the effect produced by two different supply voltages, previously identified through an electrical characterization of the device. The measurements show that the plasma actuator generates wall jets in the spanwise direction that collide with each other, resulting in wall-normal plumes. Therefore, the controlled flow exhibits regions of upwash in the central area between the electrodes and downwash aligned with the electrodes, where the flow is drawn towards the wall. As the supply voltage increases, the actuator induces higher velocities, therefore exerting a higher control authority also at the highest Reynolds number considered ($Re_\tau = 2300$). The results obtained provide a better understanding of the phenomenology of sinusoidal plasma actuators and establish a benchmark for comparison with three-electrode actuators.

Acknowledgements

Table of Contents

List of Tables

List of Figures

Nomenclature

DNS	Direct Numerical Simulation
TBL	Turbulent Boundary Layer
PDE	Partial Differential Equation
TKE	Turbulent Kinetic Energy
PA	Plasma Actuator
DBD	Dielectric Barrier Discharge
PIV	Particle Image Velocimetry
S-PIV	Stereoscopic Particle Image Velocimetry
POD	Proper Orthogonal Decomposition
HV	High Voltage
NI-DAQ	National Instruments Data Acquisition
PCB	Printed Circuit Board

Chapter 1

Introduction

Flow control is one of the promising fields of fluid dynamics that has garnered significant attention from engineers in recent years, resulting in rapid growth. It attempts to introduce perturbations into the flow field to alter the natural development path toward an ideal state and to achieve desired goals. The aim is to enhance surface performance in terms of drag reduction, aerodynamic efficiency improvement, vibration suppression, noise reduction, fuel and heat transfer enhancement, and so on. The most important application of flow control is in aviation, where it aims to improve the performance of aircraft. However, engineering applications extend far beyond the aeronautical field; for instance, the automotive industry exploits flow control techniques to reduce fuel consumption, while in civil engineering, different techniques are used to suppress wind-induced vibrations and noise in tall structures. In a historical period where environmental impact is a driving factor for technological innovation, and with the aviation sector in rapid expansion, flow manipulation techniques have become essential.

The major motivation behind this thesis is the potential to reduce the carbon footprint of aircraft, which represents one of the key targets of the ACARE Flightpath 2050 program [1]. Three main approaches have been identified to mitigate pollutant emissions: optimizing the aerodynamic design of airframes, reducing overall aircraft weight and improving aero-engines efficiency; this thesis will focus on the first one. Regarding the reduction of aircraft drag to improve aerodynamic performance, some preliminary considerations must be taken into account. The major drag component is due to skin friction, which is mainly generated in the region where turbulence occurs; therefore, research must focus on near-wall dynamics. As illustrated in Figure 1.1, more than 50% of total drag is due to viscous drag, which is caused by the interaction between the flow and the aircraft surface. It has been demonstrated through both experiments and Direct Numerical Simulation (DNS) that flow control techniques can reduce skin friction by more than 40%, which is equivalent to approximately a 15% reduction in total drag. Indeed, this drag component offers the highest potential for overall reduction.

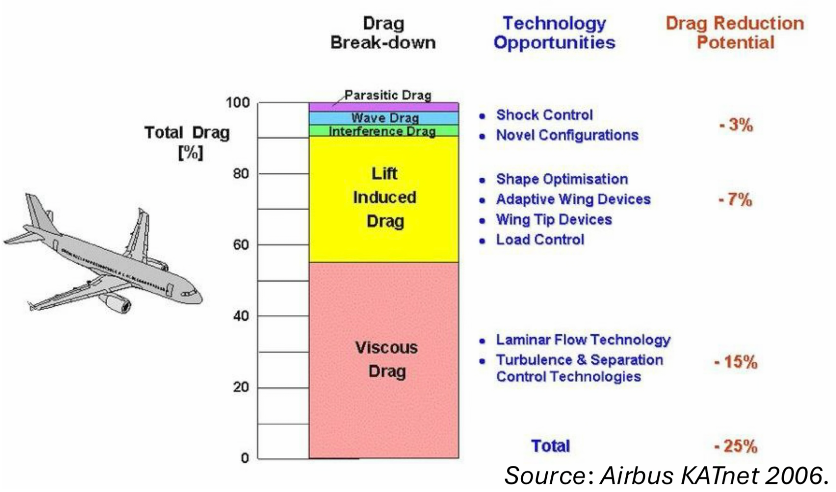

Source: *Airbus KATnet 2006.*

Figure 1.1: Drag components and corresponding drag reduction potentials.

A further consideration is that the boundary layer is inherently turbulent since aircraft typically operate at high Reynolds numbers. Consequently, the study of Turbulent Boundary Layer (TBL) manipulation techniques emerges as one of the most effective approaches to achieving a significant reduction in total drag. Numerous studies have shown that even a minimal improvement in the aerodynamic performance of an aircraft would lead to significant economic and environmental benefits, such as reducing the maximum take-off weight, increasing the transportable payload, reducing fuel consumption or increasing the achievable distance.

1.1 Boundary Layer Theory

The concept of the boundary layer was introduced in 1904 by Ludwig Prandtl, who succeeded in reconciling experimental reality with the mathematical theory of the time, which until then had been stuck at d'Alembert's paradox, according to which a body immersed in a perfect fluid experiences no drag. Analyzing flows at high Reynolds numbers, Prandtl hypothesized the existence of a thin layer of fluid near the wall, called the boundary layer, where viscous stresses dominate over inertial forces. According to this theory, the flow can be considered non-dissipative and irrotational throughout the entire domain external to the boundary layer, whereas within the layer itself, the motion is dissipative and rotational. In this region, the velocity components transition from zero at the wall, due to the no-slip condition, to the local values of the external potential flow at the boundary layer edge. This layer is characterized by strong normal gradients and, therefore, high shear stresses.

Consider a semi-infinite flat plate at zero incidence, immersed in a freestream with velocity U_∞; the boundary layer originates at the leading edge of the plate and increases in thickness along the direction of motion, as schematized in Figure 1.2. According to convention, the boundary layer thickness δ_{99} is defined as the distance from the wall at which the velocity reaches 99% of the local external potential flow velocity (U_e). As the thickness of the boundary layer grows along the plate, the internal structure of the flow undergoes a significant transition. The boundary layer can exhibit either a laminar or turbulent nature depending on the local Reynolds number, which is correlated with the streamwise position x. Near the leading edge, where the local Reynolds number is relatively low, the boundary layer is laminar. This regime is characterized by a well-organized flow, where fluid particles move along streamlines that remain parallel to the surface. However, when the critical Reynolds number is reached, the boundary layer transitions from a laminar to a turbulent regime, which is characterized by eddies.

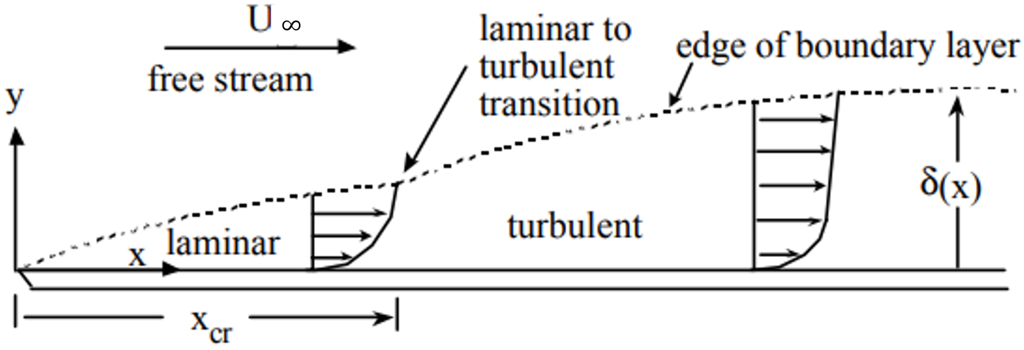

Figure 1.2: The development of a boundary layer over a flat plate [2].

1.1.1 Laminar Boundary Layer

Considering again a semi-infinite flat plate at zero incidence, with a constant freestream velocity parallel to the x-axis, the boundary layer equations can be written as follows:

$$u\frac{\partial u}{\partial x} + v\frac{\partial u}{\partial y} = \nu\frac{\partial^2 u}{\partial y^2} \tag{1.1}$$

$$\frac{\partial u}{\partial x} + \frac{\partial \nu}{\partial y} = 0 \tag{1.2}$$

$$\frac{\partial p}{\partial y} = 0 \tag{1.3}$$

where u and v represent, respectively, the velocity components in the streamwise and wall-normal directions, and ν is the kinematic viscosity of the fluid. These equations are subject to the following boundary conditions, which take into account the no-slip condition at the wall and the recovery of the freestream velocity at an infinite distance from the surface:

$$y = 0 : \quad u = 0 \quad v = 0 \tag{1.4}$$

$$y \to \infty : \quad u = U_\infty \tag{1.5}$$

By introducing the similarity variable $\eta = y\sqrt{\frac{U_\infty}{\nu x}}$ and a dimensionless stream function $f(\eta)$, such that $f'(\eta) = \partial f/\partial \eta = u/U_\infty$, the governing Partial Differential Equations (PDEs) are reduced to the Blasius equation:

$$f''' + ff'' = 0 \tag{1.6}$$

This third-order ordinary differential equation is subject to the following transformed boundary conditions:

$$\eta = 0 : \quad f = 0 \quad f' = 0 \tag{1.7}$$

$$\eta \to \infty : \quad f' = 1 \tag{1.8}$$

The local shear stress is:

$$\tau_w(x) = \mu \left(\frac{\partial u}{\partial y} \right)_w = \mu U_\infty \sqrt{\frac{U_\infty}{2\nu x}} f''_w \tag{1.9}$$

where the numerical value for f''_w for a flat plate at zero incidence is approximately 0.4696, as reported by Schlichting[3].

1.1.2 Turbulent Boundary Layer

When the Reynolds number exceeds the critical threshold, the flow transitions into a turbulent regime. Turbulence is a random and intrinsically three-dimensional process that operates as a continuum phenomenon. This state is characterized by a wide range of different scales, where the diffusive nature of the flow leads to significant energy dissipation. Moreover, turbulence is unpredictable in detail, but its statistical properties are reproducible. The flow is space and time dependent, with a very large number of spatial degrees of freedom. Since the velocity and pressure at a fixed point in space do not remain constant over time, it is useful to decompose the motion into a mean component and a fluctuating one as follows:

$$u = \overline{u} + u$$

$$v = \overline{v} + v$$

$$w = \overline{w} + w$$

$$p = \overline{p} + p$$

The time averages of fluctuating quantities are zero by definition. By applying this decomposition to the boundary layer Navier-Stokes equations, it is observed that the turbulent regime introduces an additional transport mechanism: the momentum transfer induced by turbulent fluctuations. Consequently, the total shear stress includes a supplemental term compared to the laminar case:

$$\tau = \mu \frac{\partial \overline{u}}{\partial y} - \rho\, \overline{u'v'} \tag{1.10}$$

The term $-\rho\overline{u'v'}$ is an apparent shear stress known as the Reynolds stress. The leading negative sign defines a positive Reynolds stress when the fluid layer, at a certain distance y from the wall, is accelerated by the external flow through momentum exchange. In proximity to the wall, the viscous shear stress contribution is predominant in the total shear stress; however, the Reynolds stresses rapidly become the dominant term in momentum transport as the distance from the wall increases.

Within a TBL, it is possible to identify spatio-temporal regions characterized by uniform physical properties, known as coherent structures. The comprehension of these structures is fundamental for developing drag reduction techniques.

The boundary layer is characterized by the presence of streaks, elongated low-speed regions whose life cycle is described by the bursting process. During this process, the streaks slowly lift away from the wall until they reach a critical point where they accelerate outward; this phenomenon is known as ejection. Subsequently, the streak becomes unstable and breaks up into small-scale motions. Due to mass conservation, this outward fluid motion draws high-speed fluid toward the wall, a phenomenon known as a sweep event. Both ejections and sweeps constitute the primary mechanisms for Turbulent Kinetic Energy (TKE) production near the wall.

Moving away from the wall, vortical structures such as hairpin vortices can be found. These hairpin-shaped vortices that originate at the wall are composed of two counter-rotating legs in the streamwise direction, joined by a vortex that develops in the spanwise direction, referred to as the head. Recent studies have highlighted how these structures are responsible for an increase in velocity variance within the logarithmic region. At high Reynolds numbers, this phenomenon breaks the previously hypothesized theoretical plateau, demonstrating the development of a second peak of TKE far from the wall, which significantly influences the flow dynamics in the outer regions.

To quantitatively describe these phenomena, Wallace introduced Quadrant Analysis [4], classifying velocity fluctuations (u', v') into four distinct categories based on their signs:

- Q1 ($u' > 0, v' > 0$) → outward interaction;

- Q2 ($u' < 0, v' > 0$) → ejection;
- Q3 ($u' < 0, v' < 0$) → inward interaction;
- Q4 ($u' > 0, -v' < 0$) → sweep.

Q2 and Q4 events are the primary contributors to the Reynolds stresses and dominate the turbulent dynamics; closer to the wall, sweeps prevail, whereas further away, ejections become dominant.

The TBL can be divided into two regions: the inner layer and the outer layer. The former can be further subdivided into three regions:

- Viscous sublayer; this is the layer closest to the wall, extending up to $y^+ \lesssim 5$. Since in this region, the mean velocity gradient is intense and the turbulent fluctuations are negligible, the viscous shear stress is dominant and the velocity profile is linear.

  $$u^+ = y^+$$

- Buffer layer; this is the transition layer between the viscous sublayer and the logarithmic region, where complex phenomena develop. Coherent structures exist within the viscous sublayer. This region is dominated by longitudinal streaks of high and low velocity, which are significantly elongated, unstable, and have an average spacing of approximately 100 viscous units. Quasi-streamwise vortices are particularly prevalent; they appear tilted upwards and are closely associated with ejection events and sweep events. These vortical motions are considered responsible for the formation and maintenance of the streaks themselves. In fact, turbulent kinetic energy production reaches its peak in this region.

- Logarithmic layer; this region extends for $30 \lesssim y^+ \lesssim 150$, although the upper limit depends on the Reynolds number and features a logarithmic velocity profile:

  $$u^+ = \frac{1}{\kappa} \ln(y^+) + B$$

  where κ and B are constants depending on the flow type. Here, incomplete hairpin vortices or parts of their legs are observed; these are generated near the wall and subsequently pushed outward, and they are also partially responsible for turbulence production.

Regarding the outer layer, the viscous shear stress is negligible compared to the turbulent stress. The flow dynamic in this region are governed by Large-Scale Motions and Very-Large-Scale Motions; these coherent structures are significantly larger than those found in the inner layer. According to Coles[5], the velocity profile in the outer layer can be expressed by the aforementioned log-law, supplemented by a correction function known as the Law of the Wake, which accounts for the profile's deviation from the logarithmic trend:

$$u^+ = \frac{1}{\kappa}\ln(y^+) + B + \frac{2\Pi}{\kappa}\omega\left(\frac{y}{\delta}\right) \tag{1.11}$$

where Π is the wake parameter, which depends significantly on the external pressure gradient and $\omega(y/\delta)$ is the wake function.

The typical velocity profile of a TBL is shown in Figure 1.3; by convention, the profile is plotted using non-dimensional variables scaled by viscous units, with the wall distance y^+ presented on a semi-logarithmic scale.

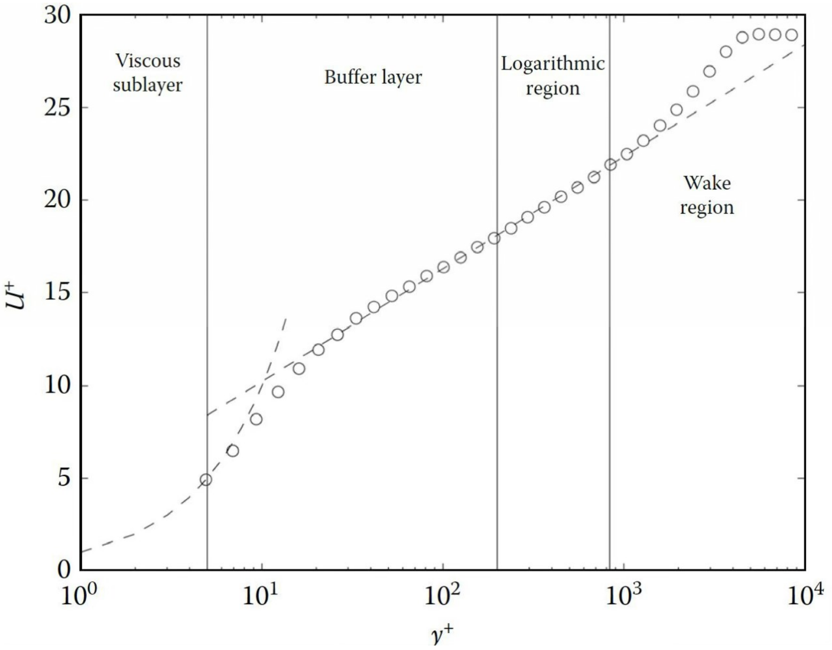

Figure 1.3: Velocity profile of turbulent boundary layer.

1.1.3 Unsteady Plane Flows

Before proceeding, it is useful to introduce the concept of the Stokes boundary layer, which is fundamental to boundary layer manipulation mechanisms such as oscillating walls and plasma actuators. The Stokes boundary layer is an exact solution to the equations when velocity and pressure are subjected to time-dependent boundary conditions. In other words, for example, it represents an exact solution to the Navier-Stokes equations that describes the motion of a viscous fluid near a wall subjected to a periodic oscillation in time.

Consider a flow over a semi-infinite flat plate in zero pressure gradient conditions that lies on the xz plane. The following hypotheses apply:

$$\frac{\partial w}{\partial z} = 0 \tag{1.12}$$

$$\frac{\partial v}{\partial z} = 0 \tag{1.13}$$

Under these hypotheses, the Navier-Stokes equations reduce to the following equation:

$$\frac{\partial w}{\partial t} = \nu \frac{\partial^2 w}{\partial y^2} \tag{1.14}$$

Now, consider a flat plate oscillating harmonically; the boundary conditions are defined as follows:

$$y = 0 : \quad w(0,t) = \begin{cases} 0 & \text{se} \quad t \leq 0 \\ w_0 \cos \omega t & \text{se} \quad t > 0 \end{cases} \tag{1.15}$$

$$y \to \infty : \quad w = 0 \tag{1.16}$$

With these boundary conditions, the analytical solution to the equation 1.14 is:

$$w(y,t) = w_0 \exp\left(-\sqrt{\frac{\omega}{2\nu}} y\right) \cos\left(\omega t - \sqrt{\frac{\omega}{2\nu}} y\right) \tag{1.17}$$

The shape of the velocity profiles is shown in Figure 1.4.

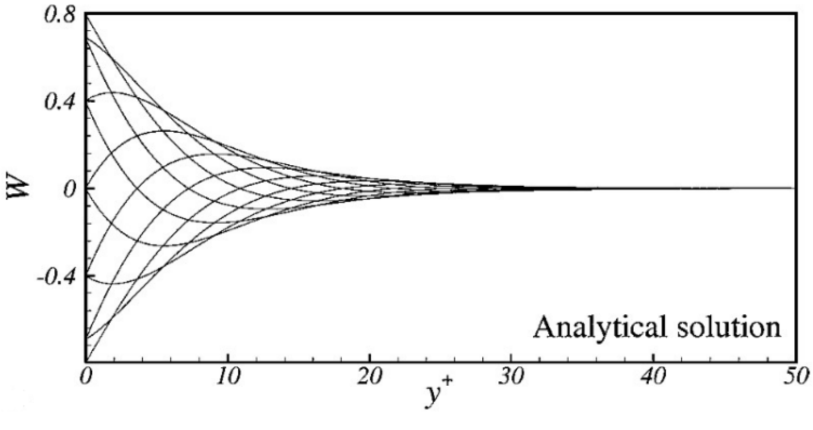

Figure 1.4: Mean spanwise velocity profiles; different curves represent different instances in time during an oscillating period [6].

Quadrio & Ricco [7] demonstrated that the Stokes layer plays a fundamental role in the mechanism of drag reduction. In particular, the induced spanwise velocity disrupts the near-wall coherent structures and interferes with the turbulence regeneration cycle. Quadrio and Ricco's analysis highlighted a linear proportionality between the reduction in resistance and the product of the maximum acceleration reached by the layer during the cycle and the wall-normal distance at which this peak occurs.

1.2 Flow Control Techniques

There are many flow control techniques that could be classified into different groups according to certain criteria. As shown in Figure 1.5, the most common classification distinguishes between passive and active methods based on energy input. Passive techniques do not require an external energy supply, while active techniques require an additional energy input. The former are easy to implement but cannot be dynamically adjusted; the latter, on the other hand, can adapt to the flow in real-time through control mechanisms. This dynamic adaptability generally makes active techniques more effective and efficient than passive ones; indeed, active techniques typically achieve up to 40% drag reduction, compared to 10% for passive ones.

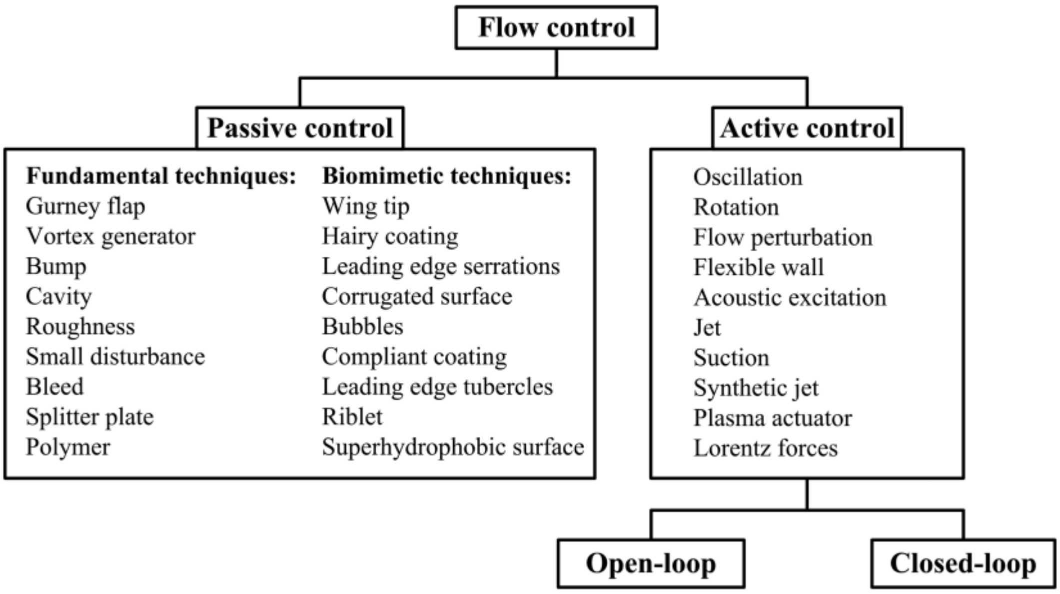

Figure 1.5: Flow control techniques classification.[8]

There are several kinds of passive flow control methods, which can be further classified into two categories. One group, called fundamental techniques, originates from basic insights into flow physics; the other, termed biomimetic techniques, is inspired by biological systems.

Active flow control techniques represent an interdisciplinary research field. Their fundamental principle consists of the targeted introduction of perturbations into the flow by integrating various physical mechanisms, for example, through mechanical actuators, electromagnetic devices or a combination of both. Active flow control can be applied using either an open-loop or closed-loop approach. An open-loop system is based on a pre-established program, and its parameters are not influenced by any control results. Conversely, the closed-loop system, as shown in Figure 1.6, uses information gathered from post-actuator sensors to adjust the forcing in real-time, making the system more reactive.

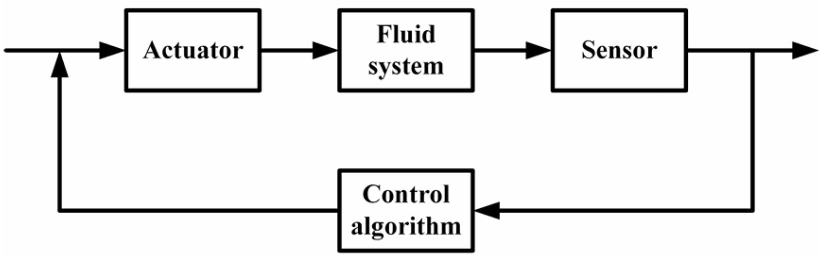

Figure 1.6: Closed-loop control algorithm.[8]

To quantitatively evaluate the performance of different flow manipulation techniques, the following key parameters are defined.

- Drag reduction rate (DR): this parameter measures the reduction in pumping power compared to the unmanipulated flow, representing the effectiveness of the control technique;
- Net energy saving (S): this accounts for the power input required to activate the control. A positive saving is achieved only when $S > 0$, indicating that the power saved through drag reduction exceeds the power consumed by the control system;
- Gain (G): this expresses the system's performance as the ratio between the power saved and the power required for control. The value $1/G$ represents the minimum efficiency threshold the physical actuator must reach to ensure a positive net energy saving.

1.2.1 Oscillating Walls

Regarding active flow control techniques, a particularly well-studied and promising approach for skin friction drag reduction is called oscillating walls. This method is based on introducing a perturbation into the flow, also called the forcing function, which is generated directly by surface motion. The choice of the direction in which to apply the wall forcing has been largely heuristic, or rather, based on experience. Since the flow near the wall is highly anisotropic, the effect of the forcing depends strongly on the direction of application. Jovanović & Bamieh[9] analyzed the problem in terms of the frequency response of a perturbed linear laminar flow. They found that the system responds strongly to both spanwise and wall-normal forcing, particularly in the streamwise velocity component. However, their results are not quantitatively applicable to fully developed turbulence. In general, it has been proven that a forcing applied streamwise is quite ineffective, in contrast to a wall-normal forcing, which is the most effective but causes strong perturbations to the natural wall turbulence. On the other hand, it has been observed that forcing applied in the spanwise direction are particularly effective and currently the subject of numerous studies. First introduced in the 1990s, the spanwise oscillating wall technique has been extensively researched; theoretical studies and Direct Numerical Simulations have shown that the sinusoidal oscillation of a wall in the transverse direction can reduce skin friction by up to 50%, which was later confirmed experimentally. A significant result was obtained by Baron & Quadrio[10] when they demonstrated that, with the correct combinations of amplitude, period, and maximum displacement, a positive net energy saving can be achieved.

Spanwise-Traveling Waves

Although uniform wall oscillation allows for significant drag reduction, research has shifted towards spatially non-uniform configurations to enhance energy efficiency. The idea of non-uniform forcing functions in space and time was introduced by Du & Karniadakis[11] when they proposed a forcing modulated in time and in the spanwise direction. The concept is to apply spatiotemporally varying body force, thereby generating waves that propagates transversely. Through DNS simulations, drag reductions of up to 30% were achieved. However, no practical experiments exist for this type of forcing, as they do not represent a real physical wall movement; furthermore, these studies resulted in negative net energy savings.

Streamwise-Traveling Waves

Similarly to waves propagating in the spanwise direction, Quadrio[12] proposed a transverse forcing modulated in the streamwise direction, generating streamwise-traveling waves. Quadrio focused on conducting an extensive parametric study to determine the conditions for maximum drag reduction. The results, reported in Figure 1.7, show that the maximum DR achieved is 45%. Moreover, the DNS simulations revealed a triangular region where, for those specific parameter combinations, there is an increase in drag.

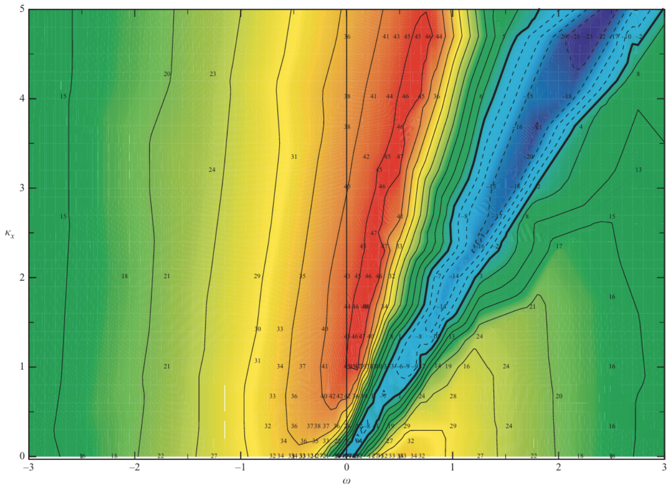

Figure 1.7: Skin-friction changes via streamwise-travelling waves[12].

The following figure illustrates some applications of Quadrio's concept. The left one represents the work carried out by Auteri et al.[13], who applied Quadrio's idea to a circular pipe; he essentially divided the surface into discrete sections, each characterized by different rotational velocities. The right one illustrates the recent experimental investigation by Knoop et al.[14], who explored the spatial evolution of a TBL subjected to a steady, square-wave (SqW) transverse wall-forcing. In this setup, the continuous sinusoidal wave is approximated by a series of streamwise-periodic belts moving in spanwise directions. This configuration allowed the authors to achieve a significant drag reduction of up to 38%, demonstrating that impulsive forcing can be as effective as traditional smooth traveling waves while offering a more feasible architecture for practical engineering applications.

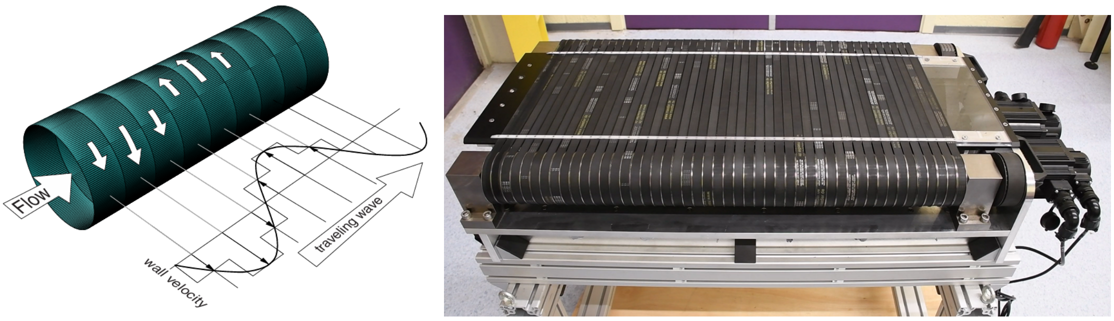

(a) Auteri's experiment[13].

(b) Knoop's experiment[14].

Figure 1.8: Streamwise-travelling waves experiment.

1.2.2 Plasma Actuators

Research on Plasma Actuators (PAs) for flow control has seen significant development since the 1990s. The interest in this type of actuator is due to the lack of moving parts, low cost, weight and power consumption, and its overall mechanical simplicity. Furthermore, their high frequency response allows for effective real-time flow modulation, making them an excellent alternative to other techniques such as oscillating walls, which involve significantly higher mechanical complexity. There are several types of plasma actuators that differ in geometry, functioning principle, and application; the most widely adopted are Dielectric Barrier Discharge (DBD) plasma actuators, which will be the subject of study in this thesis.

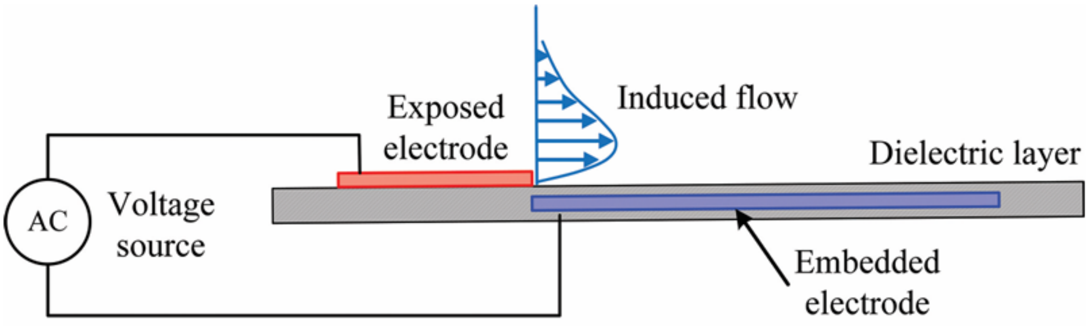

Figure 1.9: Scheme of a DBD actuator.[8]

The typical configuration consists of two long and thin electrodes: one exposed to the flow and the other encapsulated within a dielectric layer. When a high potential difference between the electrodes is applied, a region of plasma is generated near the exposed one. The charged particles are accelerated by the electric field in a direction determined by the actuator's layout, and through collisions, they transfer momentum to the neutral molecules of the surrounding air. These are zero-net-mass-flux actuators, meaning that they transfer momentum without the need for mass injection. Thus, the induced tangential force accelerates the particles toward the encapsulated electrode and, consequently, by mass conservation, the fluid ejected is replaced by the fluid from above the active surface. The actuator produces a body force that can modify flow velocity profiles or generate air jets in quiescent conditions.

During the discharge, electrons are transferred to and from the dielectric surface, thereby regulating the discharge. The accumulation of charge on the dielectric surface is the fundamental reason why the discharge is self-limiting and does not degenerate into an arc. The discharge initially ignites near the edge of the exposed electrode and then propagates along the surface until it is extinguished. Optical observations have shown that the electron density is non-homogeneous and spatially and temporally complex, with maximum densities localized precisely near the exposed electrode edge. The propagation of the discharge depends on the amplitude and frequency of the applied voltage and is limited by the extent of the encapsulated electrode. Since the electric field is confined to the region between the two electrodes, the plasma is restricted in that area as well; this limitation affects the actuator's efficiency. Furthermore, beyond a certain length, an increase in electrode size yields no further improvements. In other words, for a given voltage, there is a specific length of the insulated electrode beyond which the electrode's effect on the flow becomes negligible. A possible configuration to achieve a broader effect is to place several DBDs side-by-side and sufficiently close to one another.

The geometry of the exposed electrode plays a crucial role. Although the global properties of the discharge, such as dissipated power, are independent of the electrode thickness, the efficiency with which the actuator transfers momentum to the air depends strongly on this parameter. Indeed, experiments have highlighted that thinner electrodes provide a greater thrust for the same power input.

The electrodes are asymmetric, and it is precisely this asymmetry that introduces a preferential direction for momentum transfer. Moreover, electrons cannot transfer significant momentum to the fluid due to their negligible mass; whereas ions are able to impart it because they are heavier. Overall, a tangential air jet originates at the wall and it is called *ionic wind*. When the actuators are AC-driven, during each half-cycle, some of the charges remain trapped on the insulating material, creating what is termed *charge memory*. This phenomenon breaks the symmetry between the two half-cycles, resulting in different intensities for each one. Consequently, the sum of these effects does not cancel out, so a unidirectional net mean force is generated.

In the early 2000s, Jukes[15] hypothesized that plasma actuators could be used as an alternative to oscillating walls for the reduction of turbulent drag. The idea stems from the fact that spanwise wall oscillations, as studied in the literature, are capable of reducing friction by up to 40–45% but require complex mechanical systems that are difficult to implement on a large scale. In his experiments, conducted in quiescent air, Jukes demonstrated that plasma is indeed capable of imparting momentum to the air and producing a laminar wall jet, with velocities reaching approximately 2 m/s. Furthermore, he verified that the thrust can be modulated by varying electrical parameters, such as frequency and voltage. However, the results remain preliminary and do not guarantee that this technique can replicate the effects of oscillating walls.

Further progress was made by Choi & Jukes[16]. The measurements were conducted using hot-wire anemometry and optical techniques to obtain both temporal and spatial information. Naturally, particular attention was paid to the near-wall region where low-speed streaks and streamwise vortices originate and self-sustain cycles of turbulence. The results demonstrate that plasma actuators are capable of significantly modifying the dynamics of the turbulent boundary layer. The wall jet induces spanwise forcing that interacts with the streaks, destabilizing them and reducing their spatial coherence. As noted, an increase in wall-normal vorticity and a tendency toward the fragmentation of longitudinal structures results in a reduction of local turbulent intensity.

Figure 1.10 below shows the adopted configuration; furthermore, it illustrates the dynamic of the near-wall region in quiescent air when the actuators are activated alternately. When the plasma is activated on black electrodes, thrust is generated in the positive spanwise direction. In this case, counter-clockwise rotating vortices are formed, which grow in size as they move along the wall, driven by the transverse jets generated by the plasma. Conversely, when white electrodes are activated, the thrust is in the opposite direction, generating clockwise vortices. By periodically alternating the activation of these electrodes, a spanwise oscillation of the flow is achieved. The interaction between "new" and "old" vortices causes the flow to oscillate regularly in the spanwise direction, achieving a drag reduction of up to 40%.

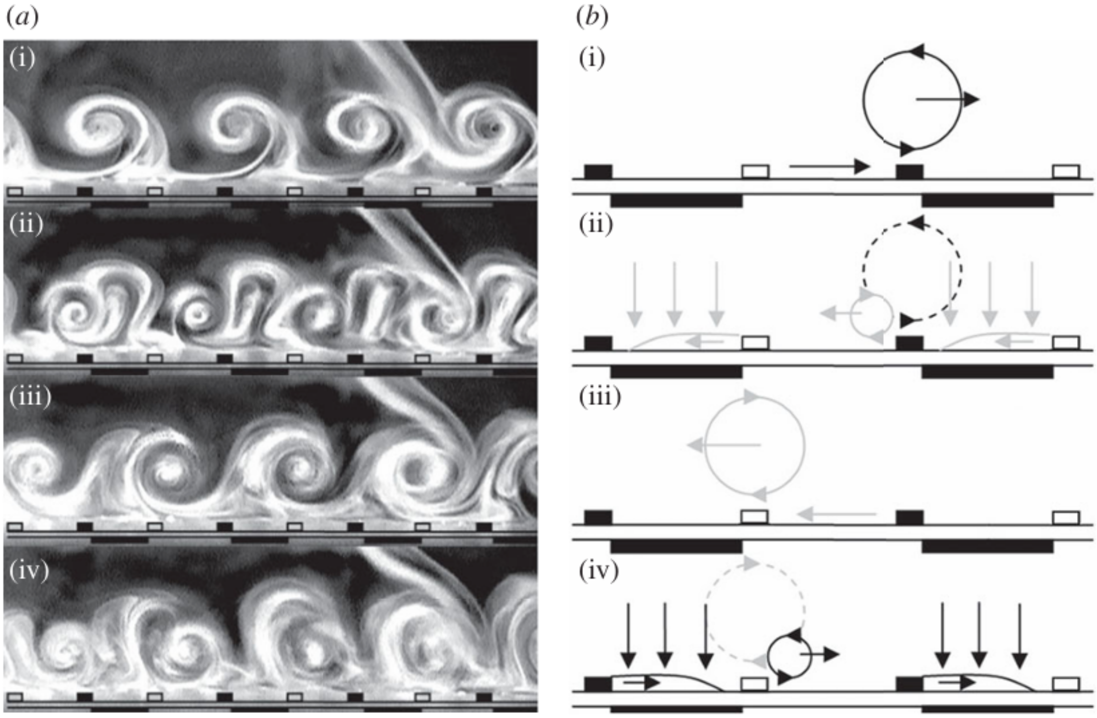

Figure 1.10: Choi and Jukes's configuration and flow visualization in quiescent air[16].

Experiments showed that the effectiveness of plasma actuators in reducing aerodynamic resistance depends strongly on both the non-dimensional oscillation period (T^+) and the normalized electrode spacing (s^+). It was observed that higher oscillation frequencies, and so lower T^+ values, generate a marked velocity deficit in the buffer and logarithmic regions of the boundary layer, associated with the formation of streamwise vortices; this reduces the velocity gradient near the wall and the effect is optimal as T^+ approaches 100. Regarding the distance between electrodes, it emerged that drag reduction occurs only for small s^+; for larger spacings, an increase in drag is observed. This behavior is attributed to the fact that the plasma-generated vortices must be sufficiently close for the upwash and downwash motions to balance each other; if the distance increases, this interaction is lost, and the transport of high-momentum fluid toward the wall increases, thereby increasing resistance. The aforementioned results are presented in Figure 1.11.

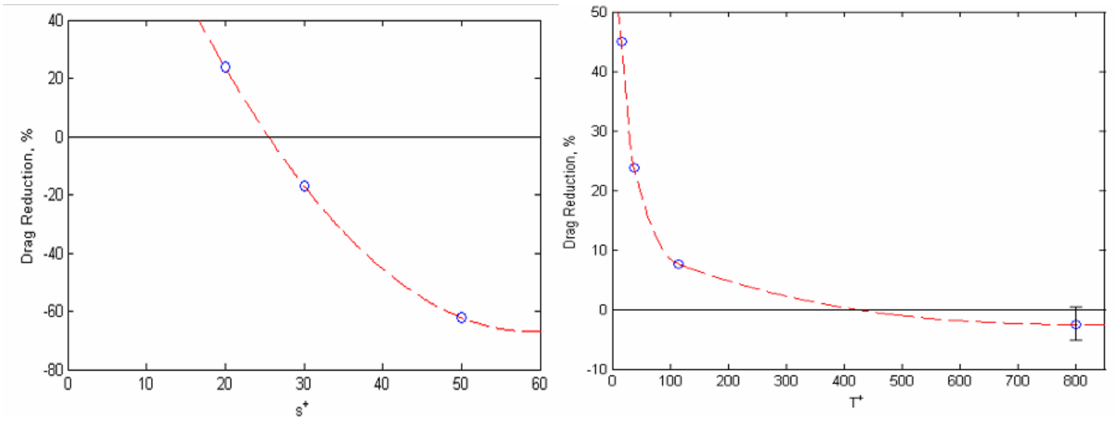

Figure 1.11: Drag reduction as a function of s^+ and T+[16].

A significant and more recent study was conducted by Zong et al.[17] in 2022. They studied the interaction between plasma jets and a TBL by measuring the flow field using Stereoscopic Particle Image Velocimetry (S-PIV) at different streamwise positions. For their experiments, they investigated three distinct working modes of the plasma actuator:

- Mode A: this configuration produces a steady unidirectional jet by activating a single high-voltage electrode. This induces a single streamwise vortex that grows within the actuation zone and decays rapidly downstream;
- Mode B: this configuration involves two high-voltage electrodes powered continuously. The two resulting wall jets collide in the middle and form a vertical jet column;
- Mode C: this configuration produces spanwise oscillating jets by switching the two electrodes alternately. Zong and his team analyzed the effect of modulation across three different frequencies.

As shown in Figure 1.12, the study revealed that in Mode C, a periodic alteration of two opposite wall jets is achieved only at the lowest frequency. At higher frequencies, the jets collide to produce a meandering vertical column, while at even higher modulation frequencies, the flow becomes nearly identical to the steady crashing jet of Mode B due to fluid inertia.

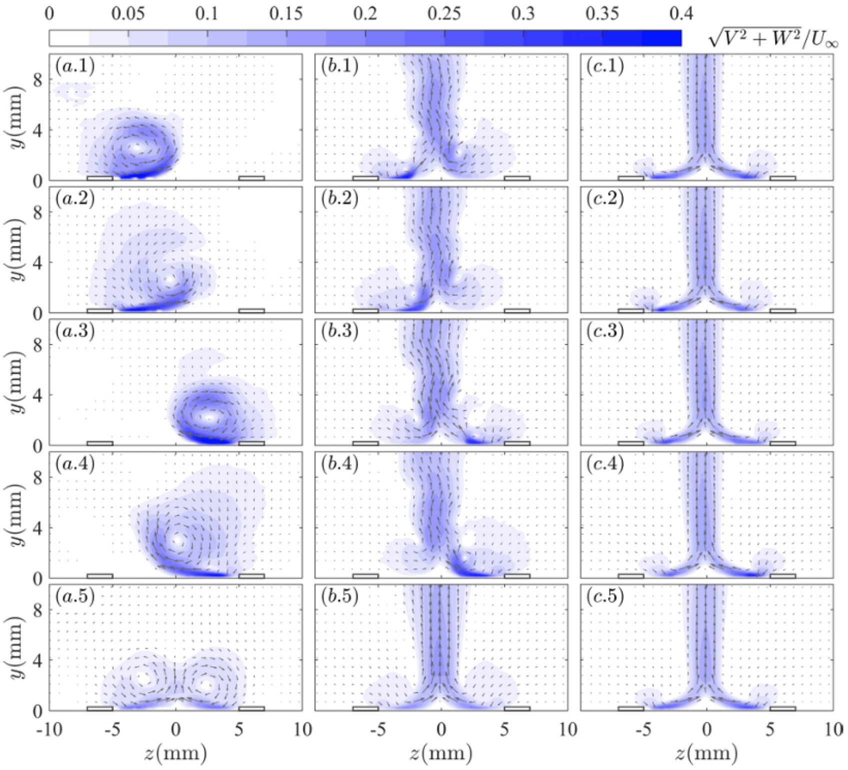

Figure 1.12: Phase- and time-averaged velocity fields for Mode C. Columns show increasing modulation frequencies (left to right), while rows 1–4 display discrete phases within the cycle. The bottom row shows the time-averaged fields[17].

Regarding the spatial distribution of relative skin friction drag variation, a high skin friction drag region is generated beneath the downwash zone. The maximum value of skin friction variation is reached just downstream of plasma actuation, after which a weak drag reduction region is induced by upwash motions. By averaging the relative drag variation along the spanwise direction, as illustrated in Figure 1.13, it is possible to observe the net impact of the actuation at various streamwise locations. Moving downstream from the actuator's leading edge to its trailing edge, the net friction drag increases approximately linearly with x^+ in all cases. Further downstream, a drag reduction region emerges due to the decay of the streamwise vortices and, extrapolating from these decreasing trends, a significant magnitude of drag reduction is expected further downstream.

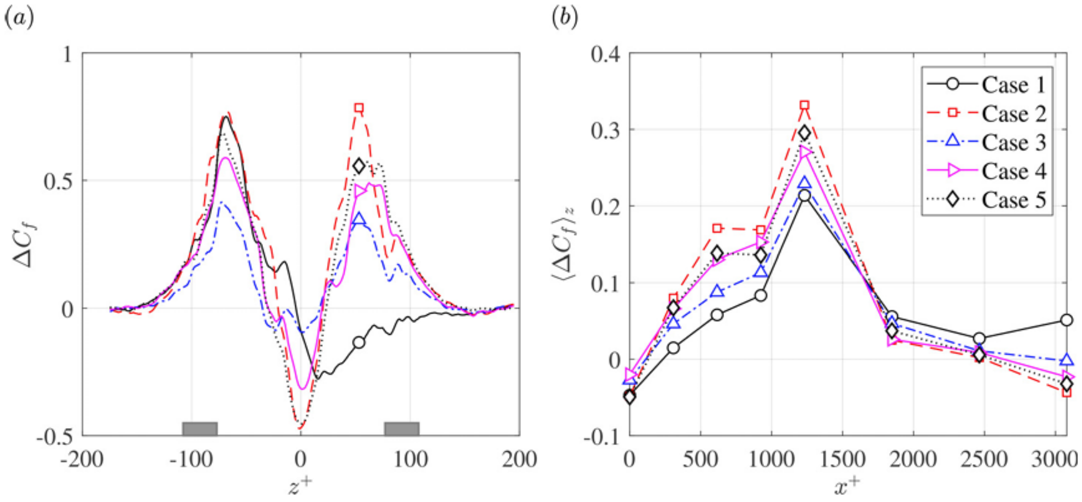

Figure 1.13: a) Spanwise distributions of the relative skin-friction drag variation at a given x^+. b) Streamwise variation of the spanwise-averaged skin-friction drag[17].

A different actuation approach was proposed by Benard and co-workers [18]. In their study, the modulation of the forcing is not achieved through temporal variation of the input signal, but rather through the geometry of the actuator itself, thus introducing a spatial modulation instead of a temporal one. Their objective was to experimentally reproduce the effect of a wall-parallel standing wave using a plasma actuator, thereby avoiding any mechanically moving components. To achieve this, the researchers designed a DBD actuator featuring an innovative electrode configuration. In particular, the grounded electrode was shaped with a semi-sinusoidal profile. The configuration of the actuator array is shown in Figure 1.14, while the geometric properties of the imposed sinusoidal waveform are summarized in Table 1.1.

Table 1.1: Geometric properties of the sinusoidal waveform [18].

λ_x^+	A^+	S^+
1035	287	575

This geometric choice is not arbitrary. The sinusoidal shape constrains the plasma discharge to develop with spatial modulation along the streamwise direction, generating an ionic wind that alternates between accelerations and decelerations. In this way, an oscillatory near-wall velocity field is created that mimics a standing wave

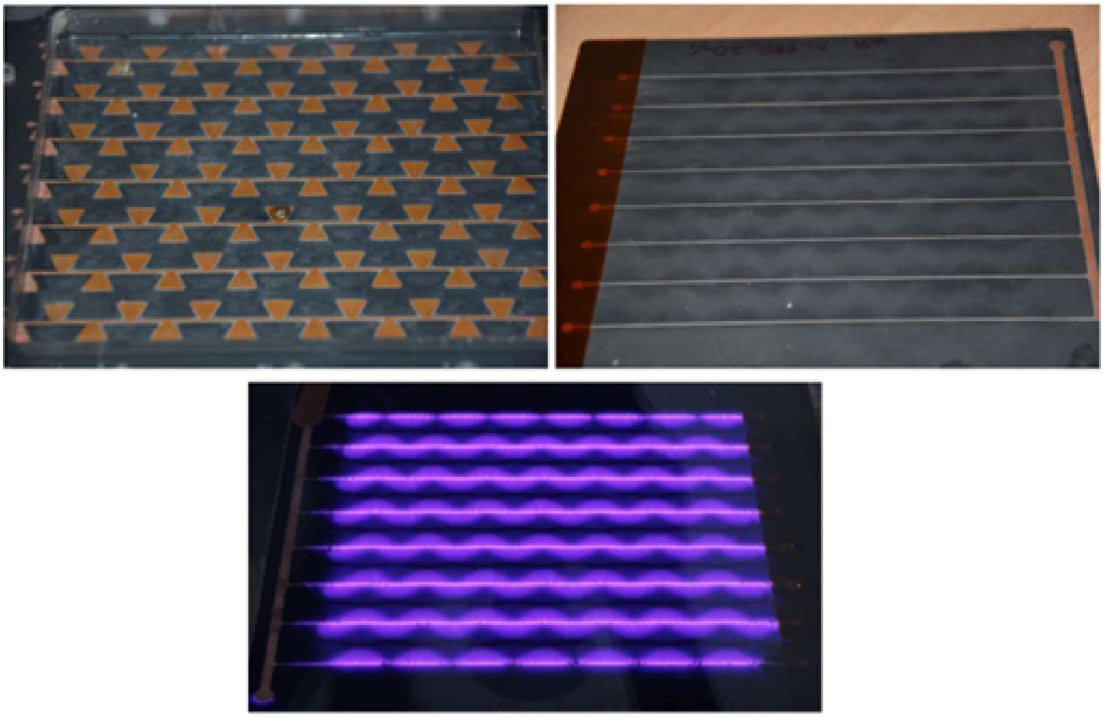

Figure 1.14: Photograph of the plasma actuator for wall-parallel standing wave forcing [18].

condition. Through Particle Image Velocimetry (PIV) measurements performed in quiescent conditions, the authors analyzed the flow generated by the actuator. The results confirmed that the induced velocity field exhibits a clear spatial alternation consistent with the sinusoidal electrode geometry, effectively reproducing the intended standing-wave-like modulation. Overall, as shown in Figure 1.15, this study demonstrates that spatially modulated plasma forcing can reproduce the effects of a wall-parallel standing wave and achieve measurable drag reduction, but only within a narrow range of operating conditions. Excessive forcing leads to a detrimental reorganization of the turbulent structures and ultimately increases drag.

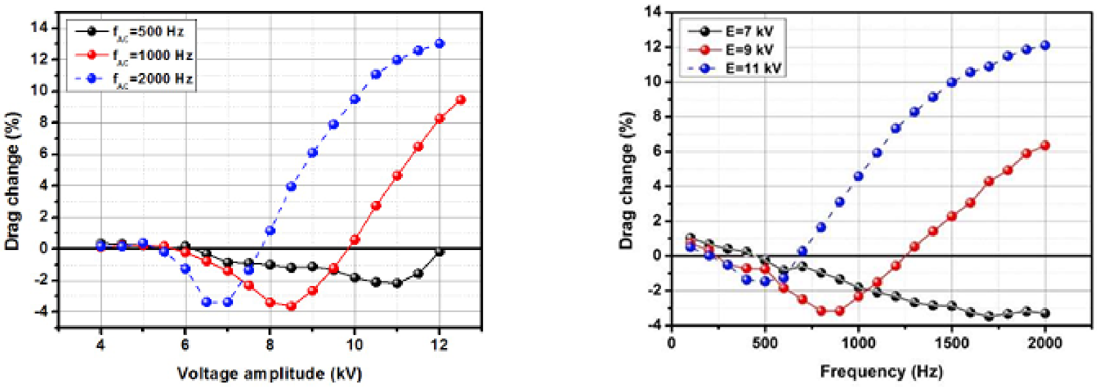

(a) (b)

Figure 1.15: Total drag change for different voltage amplitude (a) and ac frequency (b) [18].

1.3 Research Motivation

Although plasma actuators have been extensively studied, research has predominantly focused on conventional geometries with longitudinal electrodes, while only a limited number of studies have addressed unconventional configurations. The present work is motivated by the need to explore alternative actuator geometries capable of enhancing flow control performance while maintaining practical feasibility. In particular, the study draws inspiration from active flow control techniques such as the oscillating wall, which has demonstrated remarkable drag reduction capabilities, with values reaching up to 40%. This technique can generate traveling waves through modulation of the forcing, leading to significant drag reduction. However, the mechanical systems required to implement oscillating-wall strategies are complex and challenging to apply in practical scenarios.

Plasma actuators, on the other hand, provide a versatile and relatively simple solution, as they can generate flow forcing without moving parts. Moreover, the forcing can be easily modulated through voltage control. Previous studies, such as those by Jukes and Choi, have shown that properly controlled plasma actuators can also achieve drag reductions exceeding 40%. Nevertheless, most investigations have focused on the conventional three-electrode configuration. Following Bernard's approach [18], this research seeks to expand the current understanding by introducing a sinusoidal electrode geometry. Unlike the conventional configuration, which relies on two power supplies alternately switched to generate oscillating voltages and induce traveling waves, the sinusoidal geometry employs a single power supply and introduces spatial modulation through the electrode shape itself. This spatial modulation generates standing waves without temporal modulation of the input signal. This study aims to analyze the actuation phenomenology through S-PIV) measurements, providing a comprehensive characterization of the three-dimensional flow fields induced by the sinusoidal configuration.

Chapter 2

Review of Particle Image Velocimetry

This section analyzes the methodology used for data collection. Specifically, it provides a review of the literature concerning Particle Image Velocimetry, a technique that enables the determination of flow fields and provides insights into how the flow was manipulated by the actuators.

PIV is an anemometric and non-intrusive technique that provides both qualitative and quantitative information on the instantaneous velocity field of a fluid flow. This contrasts with more commonly utilized single-point measurements, such as Hot-Wire Anemometry (HWA) or Pitot tubes, which, while limited in spatial resolution, can provide excellent temporal information and a high-frequency response. Furthermore, this technique is particularly innovative as it provides detailed information on the flow field while minimizing disturbances caused by the presence of probes.

Three distinct types of PIV can be identified based on the region illuminated by the laser and the dimensionality of the resulting velocity field data:

- Planar PIV 2D2C: this configuration employs a single camera to measure the two velocity components projected onto the laser plane;
- Stereoscopic PIV 2D3C (S-PIV): the stereoscopic configuration employs two cameras to resolve the out-of-plane velocity component, thus providing a complete three-component velocity field over the laser sheet;
- Tomographic PIV 3D3C (T-PIV): this configuration employs a multi-camera setup (typically four or more) to reconstruct the three-dimensional velocity vector field within a finite volume, providing a full characterization of the flow and extending the analysis to a volumetric space rather than a single plane.

The experimental setup of a PIV system typically consists of three main subsystems, as illustrated in Figure 2.1:

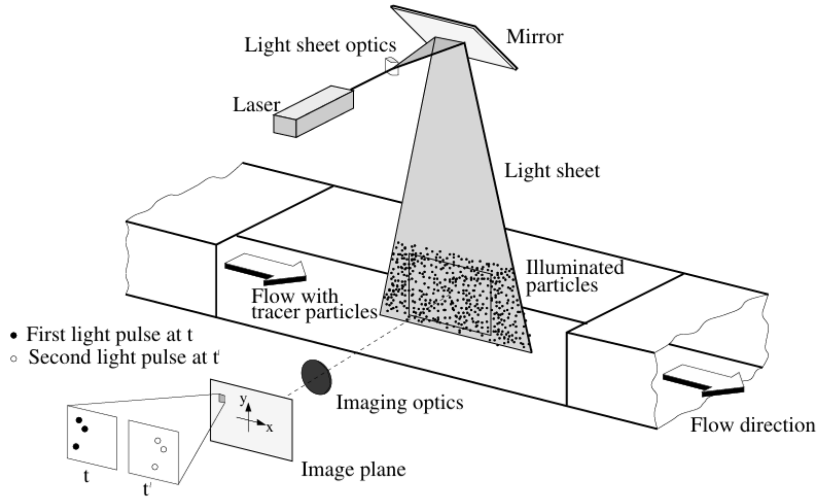

Figure 2.1: Experimental arrangement for particle image velocimetry in a wind tunnel [19].

- Light source and optics. The system typically employs a laser that provides a high-power monochromatic light beam. This beam is shaped into a thin sheet (or a volume in the case of T-PIV) to illuminate the tracing particles transported by the flow. The flow plane is illuminated at least twice within a very short time interval. This time delay is a critical parameter, adjusted according to the mean flow velocity. The lasers for PIV applications can be classified depending on the operating frequency: low speed lasers, characterized by repetition rates of up to 15 Hz and capable of delivering pulse energies reaching 800 mJ (typically 200 mJ per pulse), and high speed lasers for much higher acquisition frequencies, up to 10 kHz, with a lower energy per pulse of approximately 30 mJ;

- Camera and sensors. The camera is responsible for capturing the light scattered by the tracing particles, where the number of pixels $(N \times M)$ in the recorded images directly determines both the spatial resolution and the required storage memory. PIV cameras are typically distinguished based on their sensor technology. Charge-Coupled Device (CCD) sensors offer a more affordable solution with lower brightness levels (up to 12 bit) but carry a higher risk of sensor damage. In contrast, Complementary Metal-Oxide Semiconductor (CMOS) sensors, despite a higher average cost, provide significantly higher brightness (up to 16 bit) and greater reliability;

- Seeding. Tracing particles are used to seed the flow and are the essential element that makes the fluid motion visible. They must follow the flow without perturbing it; therefore, the fluid mechanical properties of the particles must be examined to avoid significant discrepancies between fluid and particle motion. Determining the size of the particles is crucial for accurate PIV measurements. By assuming spherical particles in a viscous fluid at a very low Reynolds number, the gravitationally induced velocity can be derived from Stokes' drag law as follows:

$$U_g = d_p^2 \frac{(\rho_p - \rho)}{18\mu} g \tag{2.1}$$

where d_p represents the tracing particle diameter, ρ_p the particle density, ρ the flow density, μ the flow viscosity and g the acceleration due to gravity. Similarly, the velocity lag U_s is defined as:

$$U_s = U_p - U = d_p^2 \frac{(\rho_p - \rho)}{18\mu} a \tag{2.2}$$

From which, the step response of U_p can be rewritten as an exponential law:

$$\frac{U_p(t)}{U} = 1 - \exp\left(-\frac{t}{\tau_s}\right) \tag{2.3}$$

which depends on the relaxation time τ_s, defined as:

$$\tau_s = d_p^2 \frac{\rho_p}{18\mu} \tag{2.4}$$

As evidenced by the previous equation, a larger particle size leads to an increased relaxation time; consequently, the resulting particle inertia prevents them from following the flow accurately. Conversely, excessively small particles do not scatter sufficient light, which would cause the processing algorithms to fail. To facilitate the selection of the optimal particle size, the dimensionless Stokes number (St) is introduced:

$$St = \frac{t_p}{\tau_s} \tag{2.5}$$

The choice of the tracing particles is made such that the dimensionless Stokes number is much smaller than unity. For our applications, Di-Ethyl-Hexyl-Sebacate (DEHS) particles generated by a Laskin nozzle were used. DEHS is characterized by chemical inertness and excellent dielectric strength, which minimize the risk of undesirable electrical arcing or short circuits.

The following discussion describes the operational procedure of S-PIV measurements. An experimental campaign can be divided into five main steps:

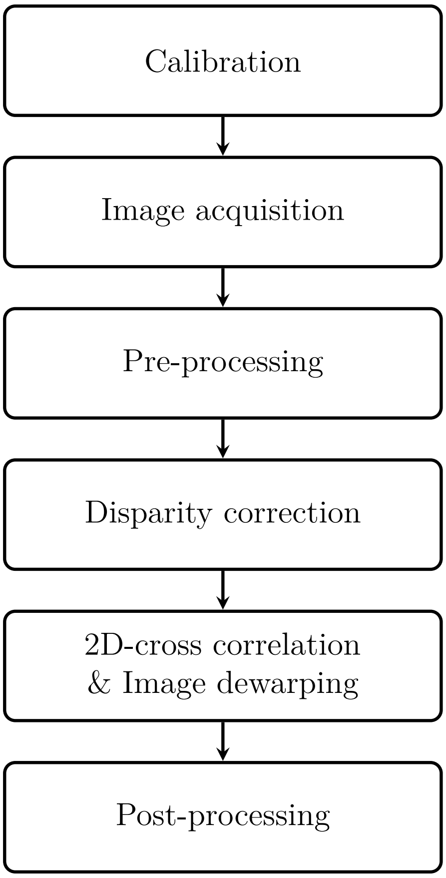

Figure 2.2: Flowchart of S-PIV measurements

2.1 Calibration

This step is essential to establish a correspondence between the information recorded on the image plane and the actual displacement of the particles on the target plane. In a S-PIV system, this process is particularly delicate as it requires the exact knowledge of several parameters, such as the lens focal length fl, the angles between the various planes θ and ϕ (see Figure 2.3), the actual position of the lens plane and the nominal magnification factor M_0. In S-PIV, the image plane is tilted with respect to the lens plane. This configuration is necessary when the camera is not perpendicular to the object plane and allows the entire image to remain in focus; otherwise, the focal distance would vary across different points of the plane. This is known as the Scheimpflug condition, and when it is satisfied, the target plane is focused completely. Knowledge of these parameters allows for the definition of the mapping functions:

$$X = f_1(x, y, \phi, \theta, M_0, fl) \tag{2.6}$$
$$Y = f_2(x, y, \phi, \theta, M_0, fl) \tag{2.7}$$

where (X, Y) are the coordinates on the image plane and (x, y) are the coordinates on the target plane. However, precisely determining all these geometric parameters is difficult, and this method does not account for non-linear effects.

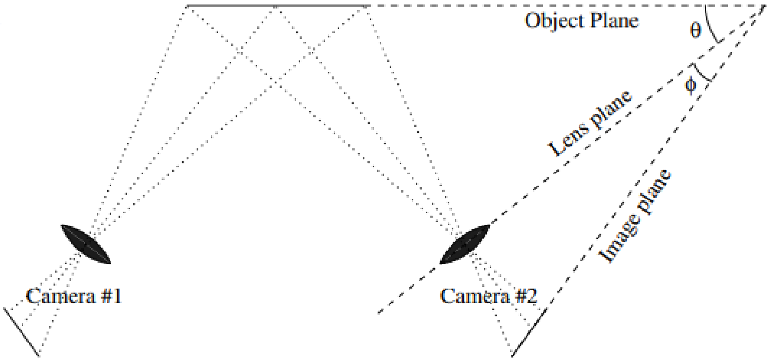

Figure 2.3: Basic stereoscopic imaging configurations satisfying the Scheimpflug condition.[19]

A more robust approach is the second-order image mapping approach, where the following functions are defined as:

$$X = a_0 + a_1x + a_2y + a_3x^2 + a_4xy + a_5y^2 \tag{2.8}$$
$$Y = b_0 + b_1x + b_2y + b_3x^2 + b_4xy + b_5y^2 \tag{2.9}$$

The twelve unknown parameters a_i can be determined using a least-squares fit if at least six image-object point pairs are provided, for instance, by employing a dual-plane target (see Figure 2.4) of known geometry. The advantage of this method is that it is not necessary to know the aforementioned imaging parameters. Furthermore, lens distortions and other image nonlinearities are inherently accounted for by the higher-order terms.

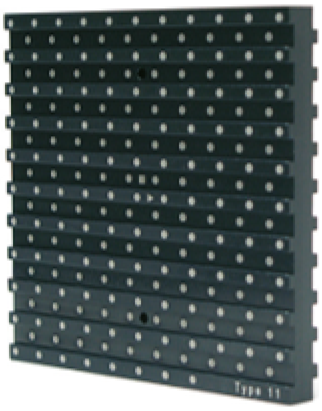

Figure 2.4: Dual-plane target

2.2 Image acquisition

The image acquisition process requires synchronization between the laser source and the camera shutters. To ensure this, a synchronizer is used. Two primary temporal parameters govern this phase: the acquisition frequency and the temporal separation (Δt). The Δt defines the time interval between the first image (Frame A) and the second image (Frame B), which are subsequently correlated to resolve the velocity field. Δt must be small enough to ensure that particles remain within the laser sheet thickness and the field of view. Typically, the temporal separation is chosen to have displacements of the tracing particles in the range of 8 to 12 pixels. Higher separations guarantee higher dynamic ranges, but other issues arise; it increases the number of particles that leave the illuminated area (3D effects) before the second laser pulse and increases the probability of false positives in the correlation process. Regarding the acquisition frequency, it must be high enough to capture small-scale fluctuations and fast temporal evolutions of the flow. However, it must be balanced to avoid excessive data volume, ensuring that both large-scale structures and small-scale dynamics are accurately resolved without compromising the quality of the statistical reconstruction. Furthermore, the tracing particle density must be carefully controlled. For the cross-correlation algorithm to function correctly, each window must contain about 8 to 10 particles per interrogation window. In fact, excessive seeding can lead to a poor signal-to-noise ratio, while insufficient seeding prevents the reconstruction of a continuous velocity field due to the lack of valid vectors in certain regions. Another parameter to consider during image acquisition is the camera f-stop, which is defined as the ratio between the focal length and the aperture diameter. Specifically, a low f-stop results in high particle brightness but a low depth of field. Conversely, a high f-stop increases the depth of field at the expense of light intensity.

2.3 Pre-processing

During the pre-processing phase, the raw images are enhanced through various algorithms to reduce several imperfections that cannot be eliminated during the image acquisition stage. Common issues include reflections from the walls or light emitted by the plasma actuator. These filtering operations are essential to increase the signal-to-noise ratio before the cross-correlation process.

Image enhancement can be achieved through several methods. A common approach is the subtraction of the average background, where the mean intensity value of each pixel across the entire dataset is calculated and subsequently subtracted from each individual frame. This method is computationally efficient and effective at removing static reflections; however, it may not yield sufficient image quality in the presence of time-varying background noise or intense intermittent reflections.

A more robust approach is the Proper Orthogonal Decomposition (POD). This method allows the velocity tensor to be decomposed into a set of orthogonal modes. Considering that each mode represents a coherent spatial structure of the flow and its energetic contribution is quantified by an eigenvalue. The flow velocity is decomposed into a mean contribution and a fluctuating term:

$$U(x, y, t) = \bar{U}(x, y) + u'(x, y, t) \tag{2.10}$$

where U and $u' \in C^{n \times m \times t}$. The first step of the POD method is to convert the velocity tensor u' into a matrix having $p = n \times m$ rows and t columns; in this way, each column represents a vectorized snapshot:

$$u' \in C^{n \times m \times t} \implies u' \in C^{p \times t} \tag{2.11}$$

Subsequently, the resulting matrix is decomposed into a product of three matrices representing, respectively, the eigenvectors, the eigenvalues and the temporal coefficients of the problem:

$$u' = \Psi \Sigma \Phi \tag{2.12}$$

The solution is not unique, as it depends on the choice of the basis functions. For the POD method, these bases are orthonormal vectors that satisfy the following condition:

$$\left|\left(\underline{u}_i, \underline{\phi}_j^\star\right)\right| = \max_{\left\|\underline{\phi}_j\right\|=1} \frac{1}{n} \sum_{i=1}^{n} \left|\left(\underline{u}_i, \underline{\phi}_j\right)\right| \tag{2.13}$$

The solution is therefore given by the normalized eigenvectors of the spatial covariance matrix, which is defined as the product between the transposed velocity matrix and itself:

$$u'^T u' = \Phi^T \Sigma \Sigma \Phi \quad \in C^{p \times p} \tag{2.14}$$

Since the covariance matrix can be computationally complex to manage, it is preferable to use the snapshot method, which exploits the temporal covariance matrix defined as:

$$u'u'^T = \Psi\Sigma\Sigma\Psi^T \quad \in C^{t\times t} \tag{2.15}$$

Since eigenvectors are ordered by decreasing energy content, the velocity field can be reconstructed by removing the first k modes, which are primarily correlated to optical reflections, and instead using the subsequent modes to recover the particle signal.

$$\underline{\underline{U}}_k = \underline{\underline{\Psi}} \begin{pmatrix} I_k & 0 \\ 0 & 0 \end{pmatrix} \underline{\underline{\Psi}}^T \underline{\underline{U}} \tag{2.16}$$

2.4 Disparity correction

In a standard S-PIV setup, the reconstruction accuracy depends on the precise alignment between the calibration target and the laser light sheet. Due to minor offsets or rotations of the target, significant discrepancies between the two camera views may be detected. Therefore, the disparity correction step adjusts the calibration, taking into account this misalignment. This procedure utilizes the acquired particle images to detect the apparent displacement of particles between the two views through cross-correlation of simultaneous frames.

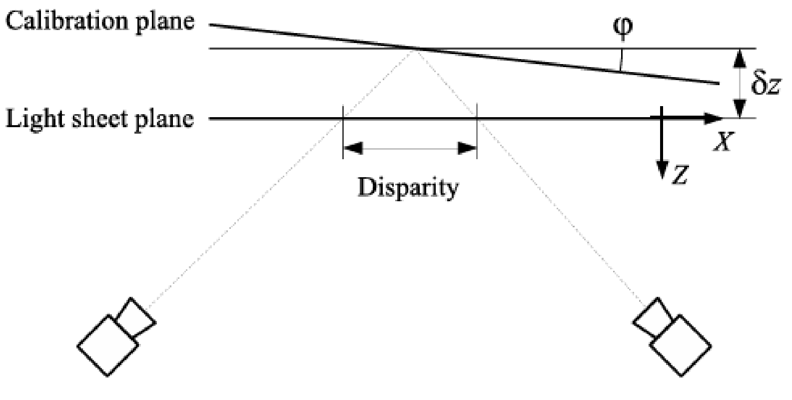

Figure 2.5: Misalignment between calibration target and light sheet plane.

2.5 2D cross-correlation & Image dewarping

The key point of a PIV measurement is the cross-correlation stage. The preprocessed images are divided into small interrogation windows (or cells). The aim is to determine the velocity vectors for each cell; to achieve this, each window in Frame

A is compared with the corresponding window in Frame B using a cross-correlation algorithm. The cross-correlation function is defined as follows:

$$R_{j,j+1}(r_1, r_2) = \sum_{h=1}^{\Delta h} \sum_{k=1}^{\Delta k} f_j(h,k) f_{j+1}(h + r_1, k + r_2) \tag{2.17}$$

where f_j is the intensity distribution of the cells and r_i denotes the displacement associated with the peak of the correlation map. This algorithm identifies the most probable displacement and, given the separation time (Δt), the velocity vector can be calculated. This step is often performed through multiple iterations, moving from large interrogation windows to progressively smaller ones. Thus, information from previous iterations can be exploited to optimize the correlation process. In fact, the displacement calculated in the initial steps is used to shift or deform the windows in subsequent iterations. To improve the spatial discretization of the field, an overlap between interrogation windows can be applied, extracting more information from the same set of tracing particles. Another important parameter to take into account is the Interrogation Window (IW) size. The selection of the IW represents a fundamental trade-off between spatial resolution and statistical robustness:

- Large windows ensure a high number of tracing particles per cell, increasing the signal-to-noise ratio and the robustness of the cross-correlation. However, they provide poor spatial discretization;

- Small windows allow for a much finer discretization of the velocity field, which is essential near the wall where gradients are high. Nevertheless, they increase the risk of having an insufficient number of particles to achieve a valid correlation peak.

To further improve accuracy, additional processes can be applied directly to the images prior to the cross-correlation. If a particle is imaged by multiple pixels, its sub-pixel position can be determined by fitting a Gaussian curve to its intensity distribution. This estimation allows the algorithm to identify the particle's center with sub-pixel resolution, significantly enhancing the precision of the displacement calculation.

In S-PIV, cross-correlation must be applied to each set of images captured by the two cameras. However, the velocity components determined in this stage do not represent the actual flow field, as they are 2D projections onto the sensors. To obtain the true velocity components, a further step of geometric reconstruction is required. Consequently, through a geometric analysis of the vectors obtained from the cross-correlation, it is possible to reconstruct the three-dimensional velocity components within the laser sheet as follows:

$$u = \frac{u_1 \tan\alpha_2 + u_2 \tan\alpha_1}{\tan\alpha_1 + \tan\alpha_2} \tag{2.18}$$

$$v = \frac{v_1 \tan\beta_2 + v_2 \tan\beta_1}{\tan\beta_1 + \tan\beta_2} \tag{2.19}$$

$$w = \frac{u_1 - u_2}{\tan\alpha_1 + \tan\alpha_2} = \frac{v_1 - v_2}{\tan\beta_1 + \tan\beta_2} \tag{2.20}$$

where u_i and v_i represent the velocity components determined through cross-correlation and α_i and β_i are obtained through geometric calibration.

For the S-PIV analysis, the *PaIRS* (Particle Image Reconstruction Software) was employed, which was developed by the University of Naples Federico II.

2.6 Post processing

In order to non-dimensionalize the results obtained and make them independent of the specific experimental conditions, the calculation of the viscous quantities is carried out. This operation allows for the derivation of fundamental parameters such as the wall shear stress (τ_w) and the skin friction coefficient (c_f). Different approaches can be employed: for example, the Clauser method. This method is based on the assumption that, in the logarithmic region of a turbulent boundary layer, the velocity profile follows a universal law. By rewriting the variables, you can determine c_f without needing to resolve the extremely thin viscous sublayer. The governing equations are rewritten as follows:

$$\frac{u}{u_\tau} = \frac{1}{k} \ln\left(\frac{y u_\tau}{\nu}\right) + B \tag{2.21}$$

$$\frac{u}{u_\tau}\frac{U_\infty}{U_\infty} = \frac{1}{k} \ln\left(\frac{y\nu}{u_\tau \nu} U_\infty\right) + B \tag{2.22}$$

$$\frac{u_\tau}{U_\infty} = \sqrt{\frac{C_f}{2}} \tag{2.23}$$

$$\frac{u}{U_\infty} = \sqrt{\frac{C_f}{2}} \left[\frac{1}{k} \ln\left(\frac{y U_\infty}{\nu}\right) + \frac{1}{k} \ln\left(\sqrt{\frac{C_f}{2}}\right) + B\right] \tag{2.24}$$

where u is the velocity profile measured and $\kappa = 0.38$ and $B = 4.17$ are the constants for a smooth-wall turbulent boundary layer. The final step involves determining C_f from this non-linear equation. Since the expression is implicit with respect to the skin-friction coefficient, it cannot be solved analytically. Therefore, a numerical best-fit procedure is employed to identify the C_f value. However, the reliability of the Clauser method depends heavily on the assumption of fixed values for κ and

B. While these constants are well-established for smooth-wall boundary layers, their universality is often questioned in the presence of flow control devices such as riblets or plasma actuators. These actuators can significantly alter the log-law intercept or the turbulence structure, making these assumptions problematic. To overcome this limitation, a more robust approach was preferred, such as the method proposed by Rodriguez-Lopez et al. [20], which enables the extraction of viscous scales without fixing the value of κ and B.

The Rodríguez-López method accounts for a potential wall-position offset (Δy). By including this parameter in the optimization procedure, it is possible to compensate for the uncertainty in the relative positioning between the measurement system and the actuator surface. It is assumed that the velocity profile is linear within the viscous sublayer and logarithmic in the log layer. To ensure a smooth and continuous connection between these two regions, the buffer layer is described using the Musker profile, which is obtained by integrating the following equation:

$$\frac{du^+}{dy^+} = \frac{\dfrac{(y^+)^2}{\kappa} + \dfrac{1}{s}}{(y^+)^3 + \dfrac{(y^+)^2}{\kappa} + \dfrac{1}{s}} \tag{2.25}$$

where s is a constant that relates the eddy viscosity in the inner and overlap regions. In order to represent the empirically observed overshoot of the mean profile with respect to the logarithmic law at high Reynolds numbers, a corrective term is introduced.

$$u^+_{bump} = \frac{\exp\left[-\log^2(y^+/M_1)\right]}{M_2} \tag{2.26}$$

Therefore, including the outer layer, the canonical profile can be expressed as follows:

$$u^+_{canonical} = \begin{cases} u^+_{musker} + u^+_{bump} + \dfrac{2\Pi}{\kappa}\mathcal{W}(y/\delta) & 0 \le y \le \delta \\ u^+_e & \delta \le y \le \infty \end{cases} \tag{2.27}$$

At this point, the canonical profile depends on five key parameters: $\{u_\tau, \Delta y, \kappa, \Pi, \delta\}$. To determine these variables, an error function is defined to evaluate the difference between the canonical profile and the experimental data points. Thus, the problem has become an optimization problem that involves the minimization of the residual error. This is achieved by varying the five unknowns within predefined ranges. Every optimization method requires a starting point, which is calculated using the aforementioned Clauser method.

Chapter 3

Experimental Apparatus

This chapter provides a description of the experimental setup employed for the mechanical characterization and the power supply system. Furthermore, the following sections will detail the data acquisition system used, the specific geometry of the PA and its manufacturing process.

3.1 PAs Manufacturing and Design

The investigation focuses on an innovative geometry characterized by sinusoidal electrodes. The design was developed in a previous thesis project [21] and it is reported in Fig. 3.1.

The exposed face features electrodes with a sinusoidal geometry, while the encapsulated side consists of a single large square electrode. Although the encapsulated electrode could have been designed to mirror the exposed one and shifted to ensure plasma inception, a simpler geometry was preferred to streamline the manufacturing process and avoid electrode misalignment issues. This design choice also promotes a more uniform plasma discharge along the entire length of the electrode. The PA was attached to a glass plate and then to a 3D-printed support, which enhances the overall rigidity of the actuator and allows it to be secured within the wind tunnel.The procedure for determining the dimensional parameters of the plasma actuator, presented in the previous thesis, is reported below. The approach requires a preliminary evaluation of the friction velocity $u_\tau = \sqrt{\tau_{wall}/\rho}$ within the wind tunnel under standard operating conditions. In particular, considering a flat plate boundary layer at a distance of $x = 3.5\,m$ from the leading edge, with standard air viscosity and a mean freestream velocity $U_\infty \approx 15\,m/s$, which represents a mid-range value of the measurement campaign. The local skin friction coefficient

(a) Sinusoidal-electrode layout **(b)** 3D-printed support

Figure 3.1: DBD-PA design and 3D-printed support.

C_f is estimated using the semi-empirical correlation:

$$C_f = \frac{0.0576}{Re_x^{1/5}} \tag{3.1}$$

where Re_x is the Reynolds number calculated at $x = 3.5\,m$, the friction velocity is derived as:

$$u_\tau = \sqrt{\frac{1}{2} C_f U_\infty^2} \approx 0.56\,m/s \tag{3.2}$$

u_τ is employed as a scaling parameter to translate the dimensionless values typically found in the literature into the physical, dimensional characteristics of the actuator. The geometric characteristics of the sinusoidal actuator are summarized in Table 3.1.

Table 3.1: Geometric parameters of the sinusoidal actuator.

Spacing		**Amplitude**		**Wavelength**		**Width**
s^+	s [mm]	A^+	A [mm]	λ_x^+	λ_x [mm]	-
575	15.7	287.5	7.85	1035	28.3	3 mm

In Table 3.2, the properties of the dielectric substrate are reported. As previously mentioned, to increase the structural rigidity of the actuator, the device was mounted on a glass support plate; this solution was implemented to prevent any bending of the substrate during testing, which could arise from the thermal stress induced by the plasma discharge.

Table 3.2: Parameters of the dielectric substrate.

Material	**Dimensions**	**Thickness**
PMMA	26 × 26 cm	2 mm

Based on the electrical characterization performed by the previous student [21], the data in Fig. 3.2 and Table 3.3 has emerged.

Measurements will be performed using slightly lower peak-to-peak voltages (V_{pp}) as a conservative approach to prevent excessive actuator stress (see Table 4.1).

Table 3.3: Operating conditions for maximum induced velocity

f_{act} [kHz]	V_{input} [V]	V_{pp} [kV]	I [A]	$w_{induced}$ [m/s]
10.10	29.00	17.28	8.06	4.92
12.00	35.00	13.92	4.50	4.36

Once the geometry and materials are selected, the fabrication of the plasma actuator follows a structured procedure. First, a dielectric board is cut to the required dimensions for wind tunnel integration (26 × 26 cm). The electrode geometry is designed using *SolidWorks*; the design is then exported as a DXF file and subsequently converted into a *GCode* file, an industry standard format.

Before the laser treatment, a black stencil layer is applied to both sides of the dielectric substrate. The GCode file is processed via *OpenBuildsCONTROL* software to control a laser pantograph, which removes the stencil only where the electrodes are to be located. A conductive nickel-based paint is then applied to these areas. This stencil-based technique ensures high-definition edges and prevents paint leakage outside the desired boundaries. After the paint has dried, the surface is sanded with abrasive paper to remove any imperfections. Finally, the remaining stencil is peeled off, leaving the completed and functional actuator.

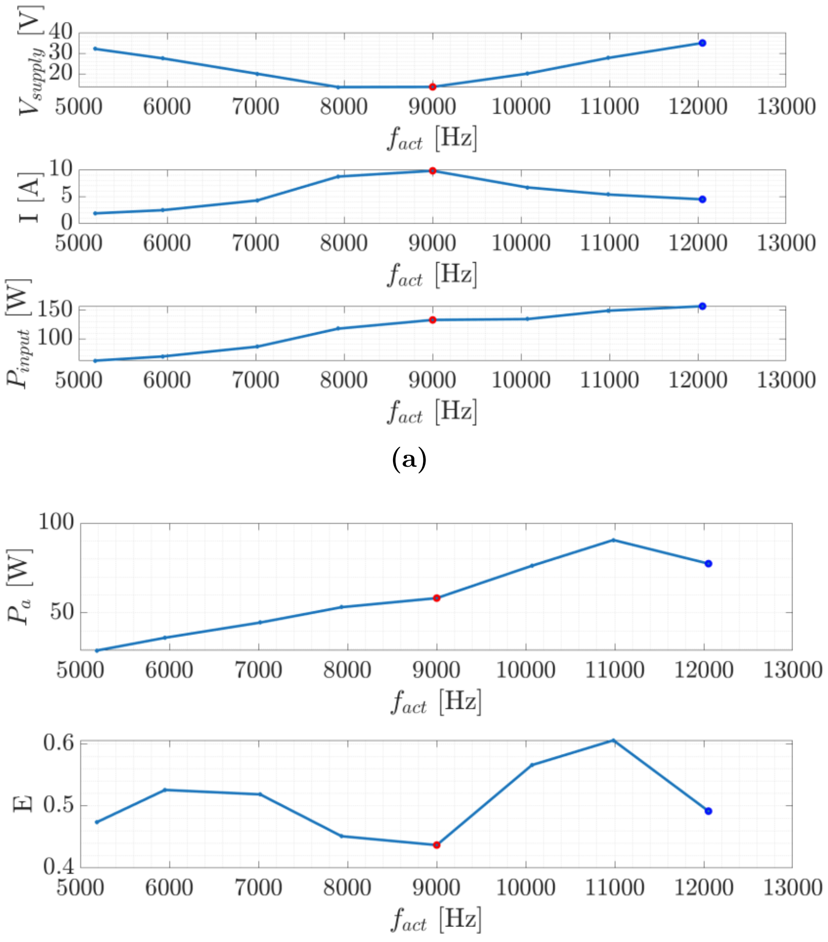

(a)

(b)

Figure 3.2: Electrical characterization as a function of the actuation frequency. Top panels: supply voltage V_{supply}, input current, and input power P_{input}. Bottom panels: effective power P_a and electrical efficiency E. Red circles: $V_{pp} = 13.12$ kV; blue circles: $V_{pp} = 13.2$ kV; remaining points: $V_{pp} = 14$ kV.

3.2 Power Supply System

The power supply and diagnostic system consist of the following main components:

- DC Power Supply: it provides electrical energy as constant direct current, acting as the primary power source for the entire circuit. In this study, a *Voltcraft VSP 2410* unit was used;

- Function Generator: it generates a low-voltage square-wave control signal, allowing for the precise setting of the operating frequency. In this study, a *RS*

Pro AFG-210005 was used;

- Extra-High-Tension (EHT) power supply: this system is designed to generate high-voltage signals from low-voltage inputs. Its primary functions include converting direct current (DC) to alternating current (AC) via a H-bridge circuit and amplifying the voltage from a few volts to the kilovolt range (in our configuration, the output is about 2000 times the input voltage). In this study, a *GBS Elektronik GmbH Minipuls 4* was used. The *Minipulse* unit constrains the applicable voltage to the actuator, as it is designed to operate with a maximum input voltage of 35 V and currents below 10 A;
- Oscilloscope: this instrument is not necessary to supply the PA but it can display the voltage applied in real-time via high-voltage and current probes. It is used as a diagnostic tool for monitoring and analyzing power consumption.

The interconnections and the signal flow between the hardware components are illustrated in the flowchart in Figure 3.3. The diagram highlights the integration between the power supply line and the control signals managed by the function generator and the NI-DAQ system.

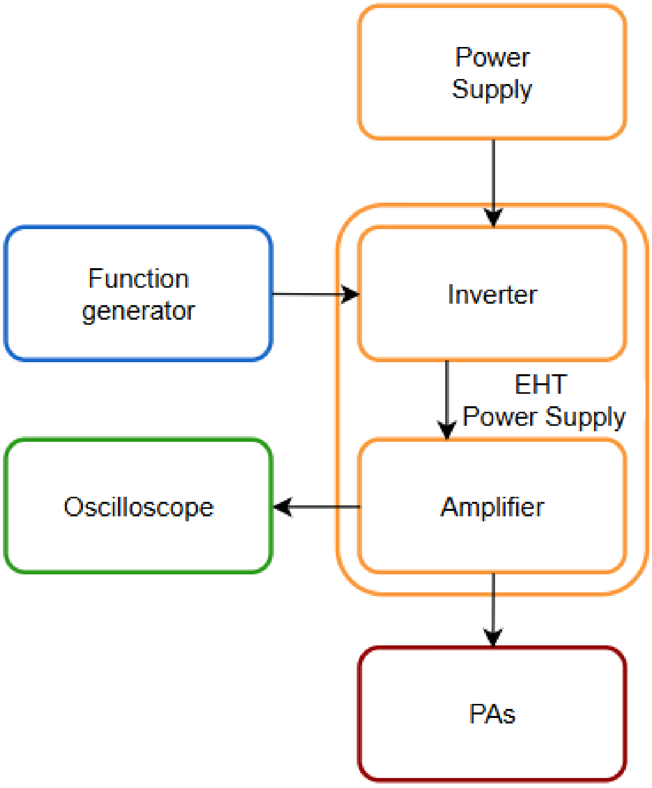

Figure 3.3: Schematic representation of the hardware interconnection.

The aforementioned equipment is shown in Fig. 3.4.

(a) Power supply **(b)** Function generator

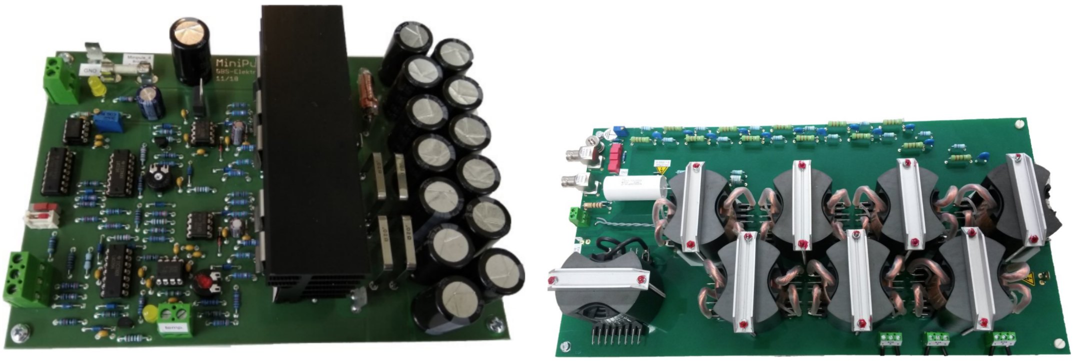

(c) Bridge **(d)** Amplifier

(e) Oscilloscope

Figure 3.4: Power supply and electrical characterization system

3.3 Wind Tunnel

Figure 3.5: The Fuxia wind tunnel of Laboratory of Aeronautics M. Panetti of Politecnico of Torino.

The measurements were conducted at the M. Panetti Aerodynamics Laboratory. The Fuxia wind tunnel, shown in Figure 3.5, is an open-circuit blowing wind tunnel equipped with a flat plate for the development of a canonical boundary layer.

The wind tunnel features two fans upstream of the stagnation chamber. To prevent propeller wake signatures from reaching the test section, a wide-angle diffuser leads to the stagnation chamber. Inside the settling chamber, honeycombs and screens are used to straighten the flow and reduce turbulence intensity, thereby eliminating velocity fluctuations and propeller-induced motions. Subsequently, the flow is channeled through a convergent duct into the test section, which has a square cross-section of 70 cm × 70 cm and a length of 5.3 m. A high contraction ratio between the settling chamber and the test section is essential; the higher the ratio, the lower the turbulence intensity of the flow.

Inside the test section, a flat plate features a super-elliptical leading edge geometry. This design prevents boundary layer separation and, under natural evolution conditions, is particularly useful for transition studies. Furthermore, the plate divides the tunnel into two regions, allowing all necessary instrumentation to be positioned in the lower zone without altering or compromising the measurements taken in the upper region. Typically, studying the natural evolution of the TBL requires 20 to 25 meter long wind tunnels; since our test section is not sufficiently long, transition is forced using a trip strip placed near the leading edge.

At the end of the plate, a flap is used to compensate for the effects of the growing boundary layer on the walls. This growth leads to a reduction in the effective cross-sectional area, which consequently induces a favorable pressure gradient ($dp/dx < 0$).

Finally, a divergent duct (diffuser) is used for pressure recovery, which improves the overall energy efficiency of the system.

The flow velocity within the test section is regulated by a closed-loop feedback system managed by a PID (Proportional-Integral-Derivative) controller, as illustrated in Fig. 3.6.

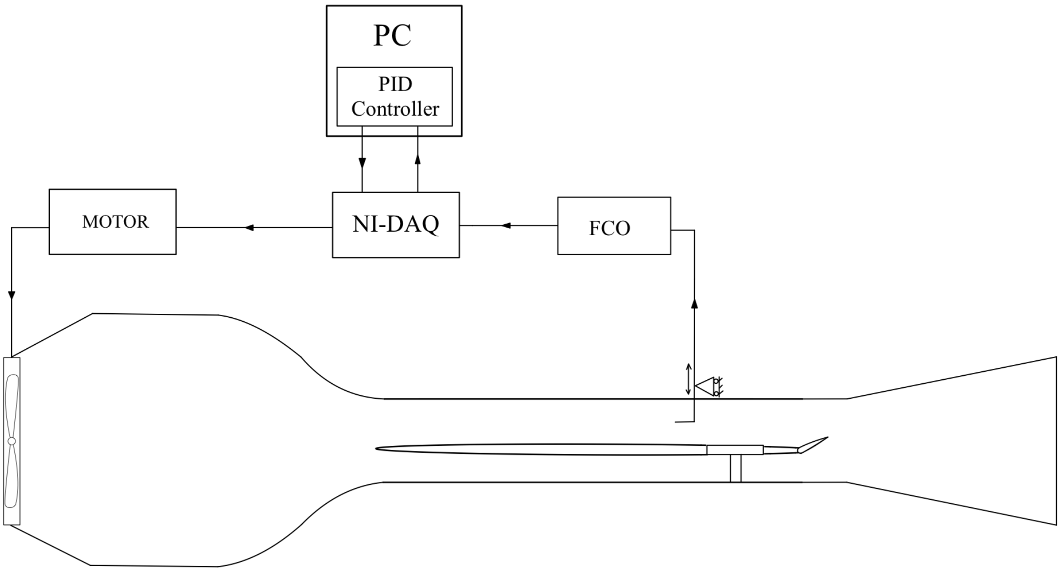

Figure 3.6: PID controller.

A Pitot tube measures dynamic pressure and transmits the signal to an FCO pressure transducer, which converts the pressure signal into an electrical one. This signal is sent to a National Instruments Data Acquisition (NI-DAQ) system that converts the analog signal into a digital one, translating the voltage into a numerical value readable by the computer. The software then compares this data with the desired velocity setpoint, allowing the PID algorithm to calculate the error and determine the corrective output $u(t)$ (note that for this discussion, $u(t)$ represents a generic control signal and not the x-component of the velocity). This command is sent back through the NI-DAQ as an output signal to the motor, which adjusts the rotational speed of the fans to stabilize the velocity.

Mathematically, the PID controller calculates the control signal $u(t)$ by acting on the error $e(t)$, defined as the difference between the setpoint $r(t)$ and the measured value $y(t)$:

$$e(t) = r(t) - y(t)$$

The general PID equation is expressed as the sum of three distinct components:

$$u(t) = K_p e(t) + K_i \int_0^t e(\tau) d\tau + K_d \frac{de(t)}{dt}$$

The coefficients K_p, K_i, and K_d act as corrective parameters that influence the speed at which the system reaches the setpoint value, ensuring that convergence toward the desired velocity is achieved in a stable manner and without divergent oscillations.

3.4 PIV Setup

As specified in the previous chapters, the implementation of a Stereoscopic Particle Image Velocimetry setup requires two cameras, a laser source, and suitable seeding particles. The setup used is shown schematically in Fig. 3.7. The entire assembly is mounted on a traversing system, allowing it to translate in the flow direction. This movement is manually regulated by a hand-wheel. This configuration enables the acquisition of S-PIV measurements at various streamwise positions.

The cameras adopted for high-frequency image acquisition are *Andor Zyla ZL41 sCMOS* cameras, featuring a 5.5 Mpx resolution and a sensor size of 2560×2160 pixels^2. Each camera is equipped with a 100 mm fixed focal length lens with a 2× teleconverter. Moreover, to satisfy the Scheimpflug condition, the cameras are equipped with a Scheimpflug adapter. This device allows for the independent rotation of the sensor plane relative to the lens plane, thereby enabling the entire image to remain in focus even when the object is tilted.

Illumination is provided by a *Litron dual-cavity laser*, operating at a frequency of 15 Hz and delivering approximately 200 mJ per pulse. The dual-cavity configuration allows for the generation of two independent laser pulses with a highly controllable time delay. This feature is essential for high-frequency sampling. Once emitted, the laser beam passes through a set of optics that transform the beam into a thin light sheet, oriented perpendicular to the flow direction.

The seeding system involves a *Laskin nozzle.* When supplied with high-pressure air ($3\,bar$) and submerged in DEHS oil, the device produces an aerosol with a mean particle size of $1\,\mu$m. The resulting seeding is injected directly into the stagnation chamber through perforated tubes. Initially, it was intended to be upstream of the fans; however, this would have caused excessive loss of seeding due to the fan blades.

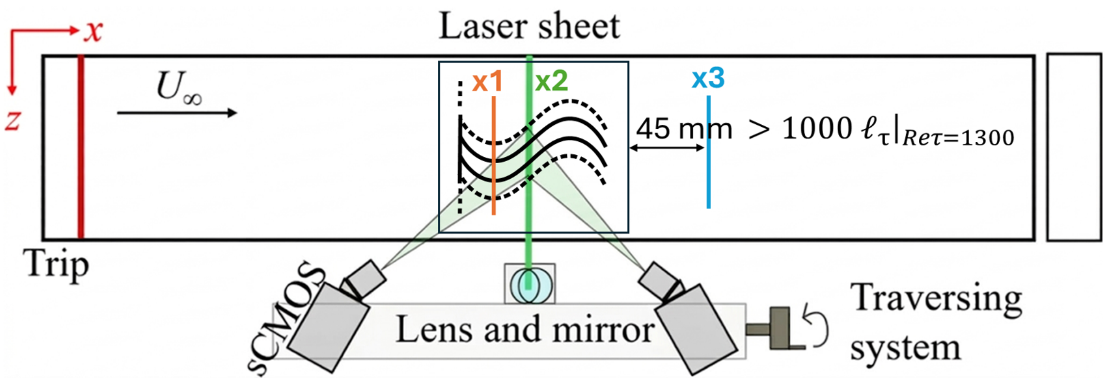

(a) Top View.

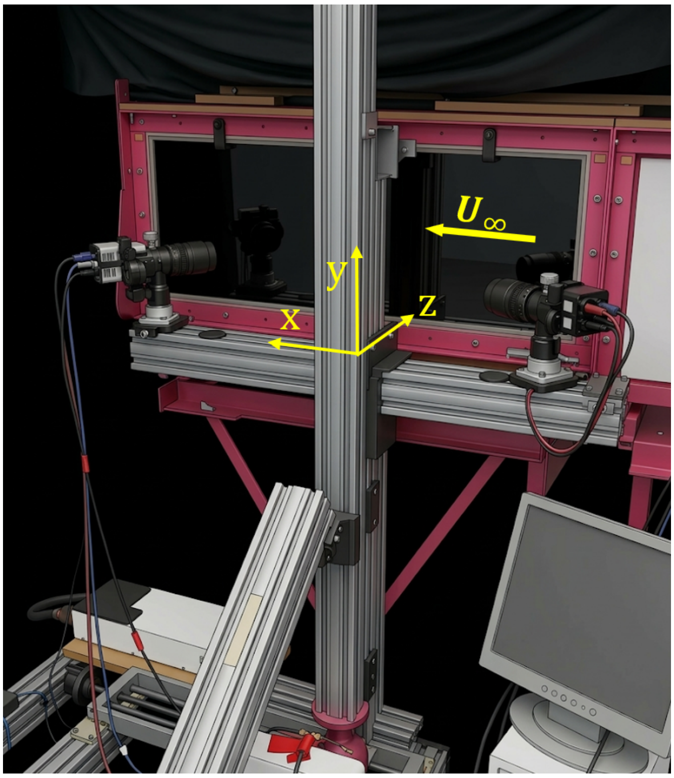

(b) Side View.

Figure 3.7: Schematic representation of the PIV experimental setup.

All the components required for the PIV are shown in the following figures:

(a) Litron laser **(b)** *Andor Zyla ZL41 sCMOS* cameras

(c) Laskin nozzle

Figure 3.8: Principal components of the PIV setup.

Chapter 4

Results

This chapter will present the results obtained from the S-PIV campaign. Before discussing the results, the experimental matrices are reported to summarize all the measured cases. The following table refers to three distinct measurement positions: $x1$, $x2$ and $x3$ (downstream). Specifically, x1 and x2 correspond to the maximum/minimum and intermediate points along the sinusoidal wave of the exposed electrode. These measurement locations are graphically represented in figure 4.1.

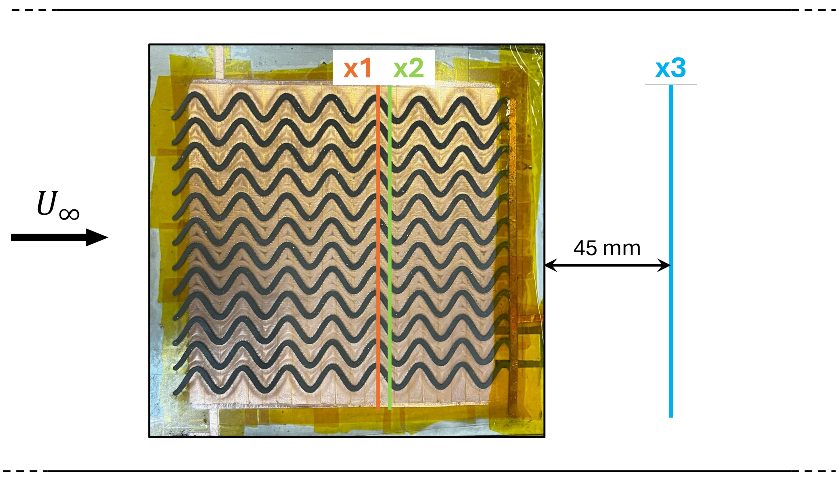

Figure 4.1: S-PIV measurements stations

The downstream measurement position was located approximately 1000 viscous units ($\Delta x^+ \approx 1000$) from the actuator's trailing edge. A relevant question often addressed in literature is the persistence of the actuation effect downstream of the array, for example in terms of drag reduction. To investigate this evolution, a specific downstream measurement location was selected. This position was determined a posteriori: once the viscous scales (ℓ_ν) for the non-actuated cases were established, it was possible to define the physical distance for the target placement. To ensure experimental consistency and due to the time-intensive nature of the calibration process, this fixed location was maintained for all test cases, avoiding the uncertainties associated with frequent sensor repositioning and re-calibration; the case characterized by a free-stream velocity of $U_\infty = 9$ m/s was selected as the reference

Table 4.1: Experimental matrix for sinusoidal PA PIV measurements.

Positions	U_∞ [m/s]	Time delay Δt [μ s]	Acquisition time [s]	V_{pp} [kV]	f_{act} [kHz]
x1	9	30	60	0	10.2
			90	14	
				15.8	
	14	15	60	0	
			90	14	
				15.8	
	16	13	60	0	
			90	14	
				15.8	
x2	9	30	60	0	
			90	14	
				15.8	
	14	15	60	0	
			90	14	
				15.8	
	16	13	60	0	
			90	14	
				15.8	
x3	9	30	60	0	
			90	14	
				15.8	
	14	15	60	0	
			90	14	
				15.8	
	16	13	60	0	
			90	14	
				15.8	

4.1 Data Validation

To validate the entire measurement chain and hence the reliability of all the experimental data, it is necessary to compare measurements obtained from benchmark test cases with known reference results. The mean velocity profiles are presented below, compared with the results obtained from DNS carried out by Schlatter and Örlü for a TBL characterized by a friction Reynolds number of $Re_\tau = 1270$. Some discrepancies in the values may be observed; however, these can be attributed to the inherent uncertainties of the experimental measurements and to the fact that the presence of the electrodes inevitably alters the surface roughness of the plate. What is crucial to observe, however, is the trend of the profiles in the log layer, which should match the DNS results as closely as possible.

Another metric that can be used to assess the equilibrium state of the boundary layer is the diagnostic plots, reported in Figure 4.2 which is a graphical method used to rapidly assess the quality of experimental data in turbulent boundary layers, obviating the need to calculate the viscous scales. It allows for the verification of a canonical profile by comparing the velocity profiles within the logarithmic region. In this region, the curves are expected to overlap regardless of the Reynolds number. Conversely, the region closer to the wall is subject to Reynolds number effects; therefore, it is expected that the curves deviate from the reference.

The Table 4.2 presents the linear interpolation coefficients calculated within the logarithmic region for the different test cases. Additionally, the percentage error is reported relative to the reference DNS data, characterized by a slope $m = -0.245$ and an intercept $q = 0.28$.

Table 4.2: Linear regression coefficients (m and q) and percentage errors in the logarithmic region relative to the reference DNS ($m_{DNS} = -0.245$, $q_{DNS} = 0.28$) for various positions and freestream velocities.

Positions	**U_∞ [m/s]**	**m**	**q**	**Err %**
$x1$	9	-0.24	0.27	1%
	14	-0.23	0.27	4%
	16	-0.21	0.28	3%
$x2$	9	-0.24	0.27	1%
	14	-0.25	0.28	5%
	16	-0.21	0.26	2%
$x3$	9	-0.22	0.26	2%
	14	-0.25	0.28	2%
	16	-0.22	0.26	2%

The error is calculated as follow:

$$Err_{\%,\text{ avg}} = \frac{1}{N}\sum_{i=1}^{N}\left|\frac{u_{rms}/U_\infty - (u_{rms}/U_\infty)_{DNS}}{(u_{rms}/U_\infty)_{DNS}}\right| \times 100$$

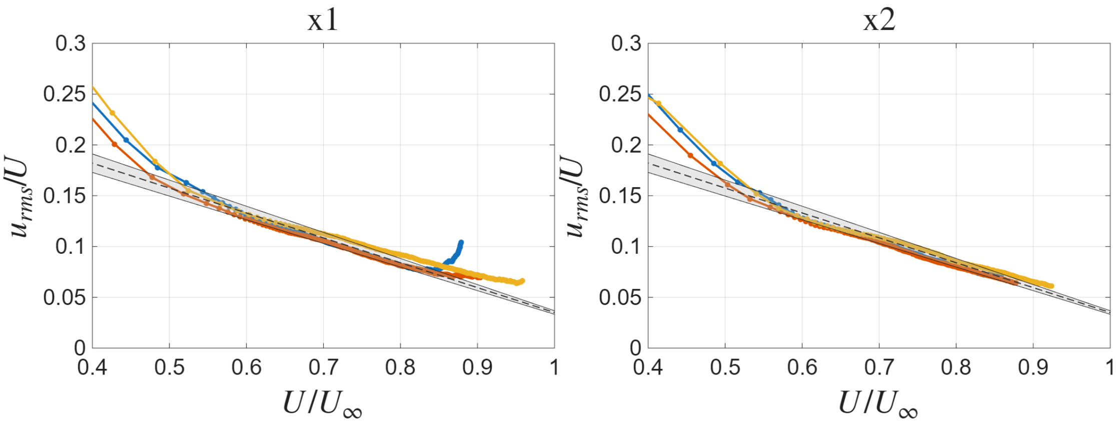

(a) Test case: x1 - unactuated flow

(b) Test case: x2 - unactuated flow

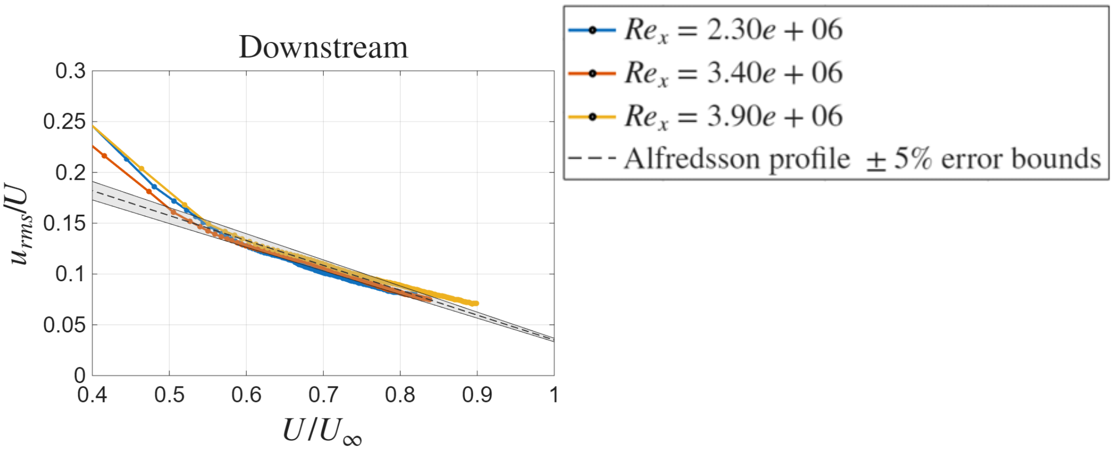

(c) Test case: downstream - unactuated flow

Figure 4.2: Diagnostic plots of the boundary layer for various freestream velocities and measurement positions.

The mean velocity and Reynolds stress profiles are reported below, see Figure 4.3. These data are processed using the Rodríguez-López approach (see Paragraph 2.6) to determine the viscous scales and are subsequently normalized by them.

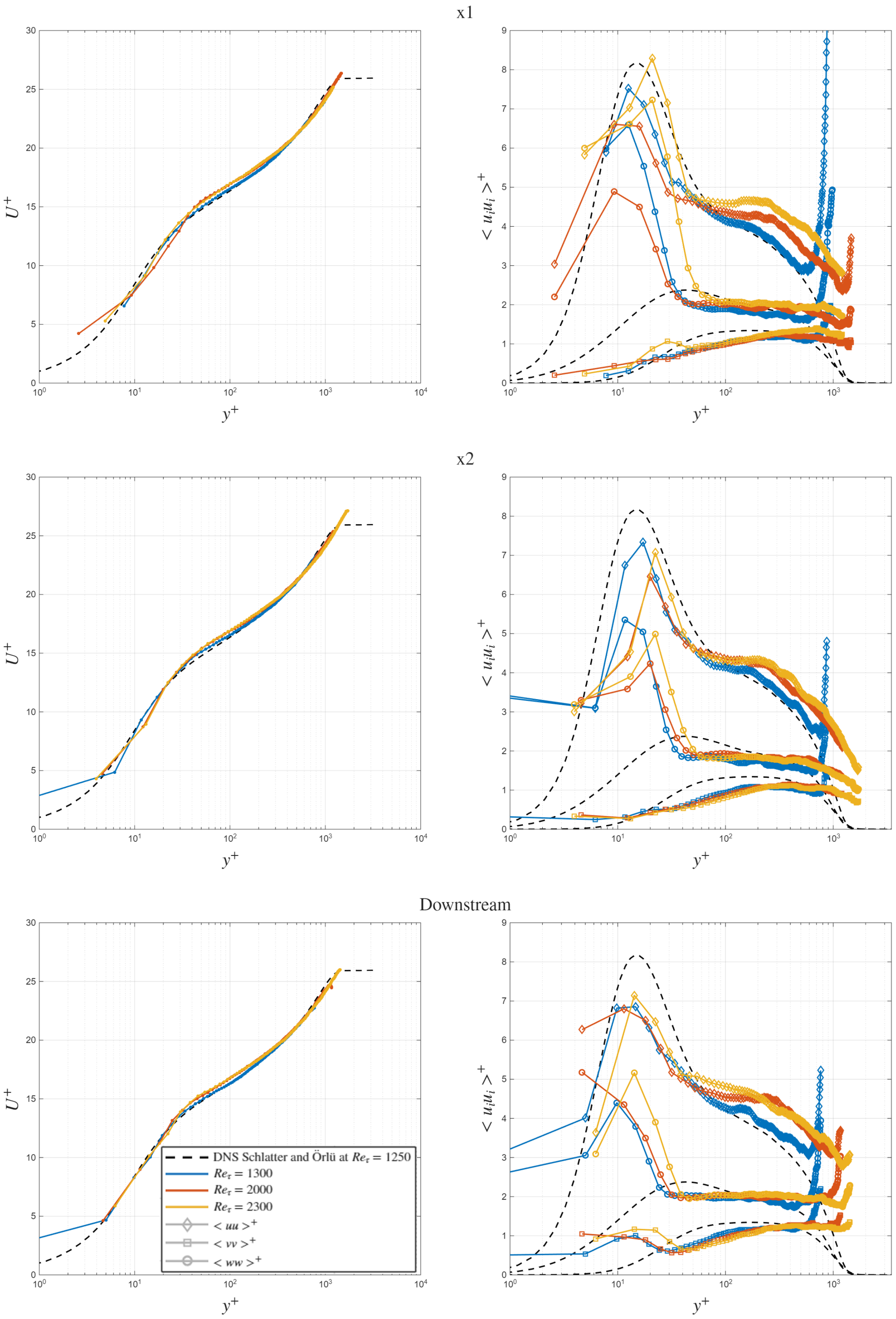

Figure 4.3: Mean velocity U^+ (left) and Reynolds stress components $\langle u_i u_i \rangle^+$ (right) as a function of y^+, compared with DNS data at $Re_\tau = 1270$ (black dashed lines). Color coding denotes friction Reynolds numbers (Re_τ) cases, while markers distinguish the stress components: $\langle uu \rangle^+$ (diamonds), $\langle vv \rangle^+$ (squares), and $\langle ww \rangle^+$ (circles).

Regarding the outer layer, the slight deviations observed in the profiles can be linked to local seeding density fluctuations. Similarly, in the inner layer, the minor discrepancies between experimental data and the reference DNS are likely due to laser reflections on the actuator surface. Despite these localized near-wall and far-field effects, the diagnostic plot and the overall trend of the Reynolds stress profiles show consistent agreement with the literature. This confirms that the experimental apparatus provides a reliable representation of the flow physics under investigation. The viscous scale values obtained from the optimization process are reported in the following table.

Table 4.3: Boundary layer parameters and optimized viscous scales (u_τ, l_τ) for the three investigated free-stream velocities across different streamwise positions ($x1$, $x2$, and $x3$).

Positions	U [m/s]	u_τ [m/s]	l_τ [m]	δ [m]	Re_δ	Re_τ
$x1$	9	0.38	4.05e-05	0.0510	2.24e5	1300
	14	0.52	2.93e-05	0.0550	3.37e5	2000
	16	0.65	2.45e-05	0.0525	3.90e5	2300
$x2$	9	0.37	4.09e-05	0.0510	2.17e5	1300
	14	0.52	2.94e-05	0.0550	3.24e5	2000
	16	0.62	2.46e-05	0.0525	4.18e5	2300
$x3$	9	0.37	4.17e-05	0.0510	2.05e5	1300
	14	0.53	2.98e-05	0.0550	3.14e5	2000
	16	0.64	2.50e-05	0.0525	3.94e5	2300

4.2 Velocity fields

The following figures illustrate the flow fields for each velocity component across the analyzed test cases at the specified measurement positions. The fields are first time-averaged and subsequently subjected to periodic averaging in the spanwise direction, exploiting the geometric periodicity of the electrode arrangement. In this way, the statistical robustness of the obtained data is increased. The data are non-dimensionalized using u_τ and ℓ_τ derived from the corresponding unactuated (no-plasma) case. This approach was adopted because determining the skin friction velocity for the actuated cases is particularly challenging; the presence of plasma introduces significant noise and prevents accurate near-wall measurements, thereby hindering the reliable application of the Rodriguez-Lopez algorithm. The velocity fields are calculated by subtracting the corresponding unactuated case from the actuated datasets. This subtraction highlights the flow regions specifically altered by the plasma actuator. Furthermore, a comparison between the effects obtained by operating the plasma actuator at two different voltage levels will be presented in Section 4.3.

Regarding the streamwise velocity component, see Figure 4.4, a distinct deceleration is observed in the intermediate region, followed by a significant acceleration in proximity to the exposed electrodes. The effects are notably more intense in the high-voltage case, indicating a stronger momentum injection into the boundary layer as the electrical potential increases.

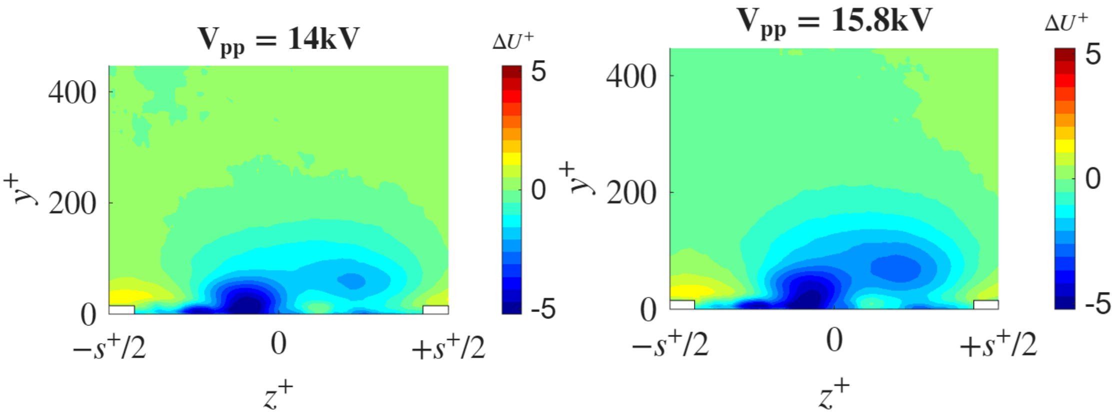

(a) Test case: x1 $Re_\tau = 1300$ $V_{pp} = 14\ kV$. **(b)** Test case: x1 $Re_\tau = 1300$ $V_{pp} = 15.8\ kV$.

Figure 4.4: Induced streamwise velocity fields (ΔU^+) for the two analyzed voltage levels in position $x1$.

As shown in Figure 4.5, completely analogous behavior is observed at position $x2$.

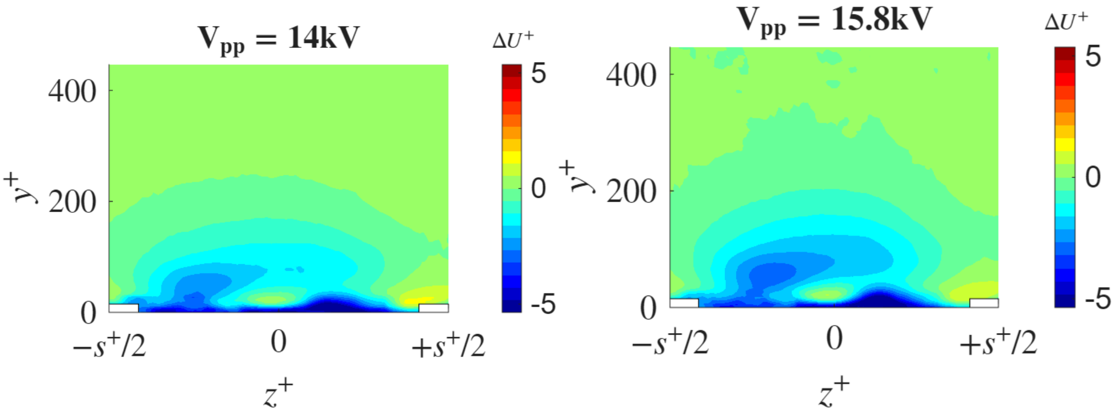

(a) Test case: x2 $Re_\tau = 1300$ $V_{pp} = 14$ kV. **(b)** Test case: x2 $Re_\tau = 1300$ $V_{pp} = 15.8$ kV.

Figure 4.5: Induced streamwise velocity fields (ΔU^+) for the two analyzed voltage levels in position $x2$.

From the analysis of the wall-normal velocity component in position $x1$, see Figures 4.6a and 4.6b, two distinct downwash regions are clearly visible in correspondence with the exposed electrodes, where the fluid is drawn toward the surface. In parallel, two upwash regions are observed in the central zone; these two ascending jets tend to converge and merge at an altitude of approximately $y^+ \approx 100$, enclosing a small residual downwash zone in the center. This central lobe is probably due to a recirculation structure caused by the weak initial interaction between the jets generated by the electrodes.

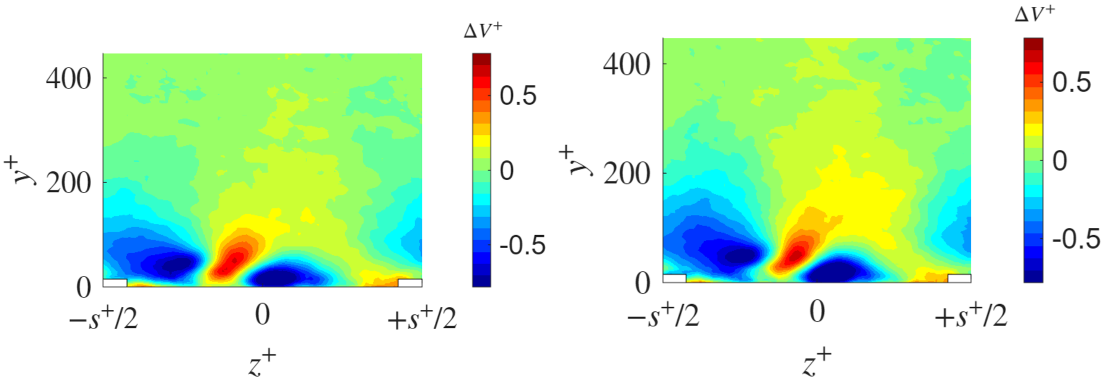

(a) Test case: x1 $Re_\tau = 1300$ $V_{pp} = 14$ kV. **(b)** Test case: x1 $Re_\tau = 1300$ $V_{pp} = 15.8$ kV.

Figure 4.6: Induced wall-normal velocity fields (ΔV^+) for $V_{pp} = 14$ kV in position $x2$.

Instead, in position $x2$, Figures 4.7a and 4.7b, a significantly different interaction is evident. At this station, the electrodes are closer together, leading to a much stronger coupling between the generated ionic winds and higher induced velocities. Specifically, an intense upwash region in the middle and two downwash regions located directly above the exposed electrodes can be observed.

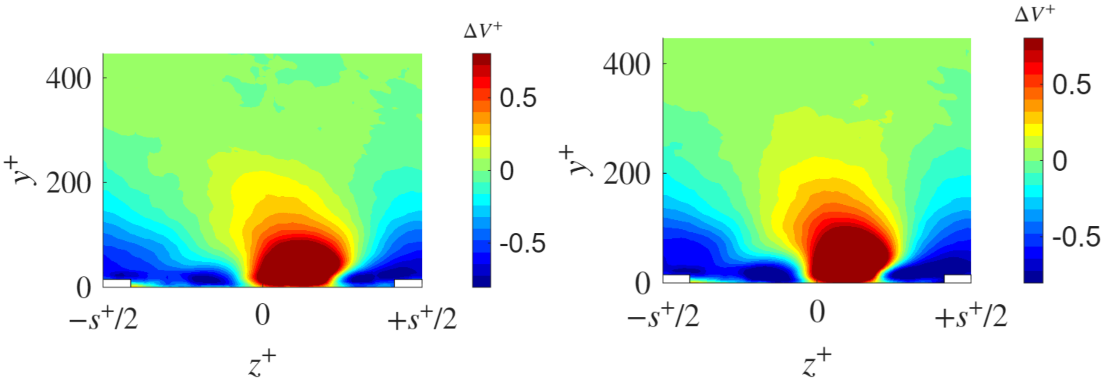

(a) Test case: x2 $Re_\tau = 1300$ $V_{pp} = 14\ kV$. **(b)** Test case: x2 $Re_\tau = 1300$ $V_{pp} = 15.8\ kV$.

Figure 4.7: Induced wall-normal velocity fields (ΔV^+) for $V_{pp} = 15.8$ kV in position $x2$.

Finally, concerning the spanwise component, a rightward induced jet generated by the left electrode can be observed, stronger than the opposite one. This behavior is due to the sinusoidal geometry: the left electrode is located at a minimum point, where a constructive superposition of the induced jets from the surrounding electrode segments occurs, whereas at the right electrode, which is located at a maximum, a weaker induced jet is observed in terms of velocity. The physical mechanism described above is schematically represented in the following figure.

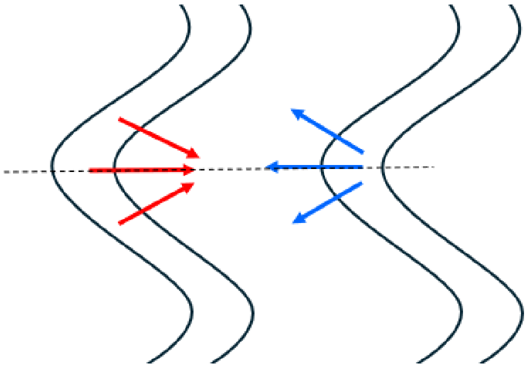

Figure 4.8: Schematic representation of the induced flow field interaction in the x1 position.

At position $x1$, two large lobes of opposite sign are clearly visible in correspondence with the exposed electrodes. Conversely, the phenomenology at position $x2$ appears more complex: in addition to the two primary lobes located above the electrodes, two further regions of opposite sign emerge in the inter-electrode area. These induced velocities are attributable to the jets generated upstream, which are subsequently convected by the main flow toward the downstream section.

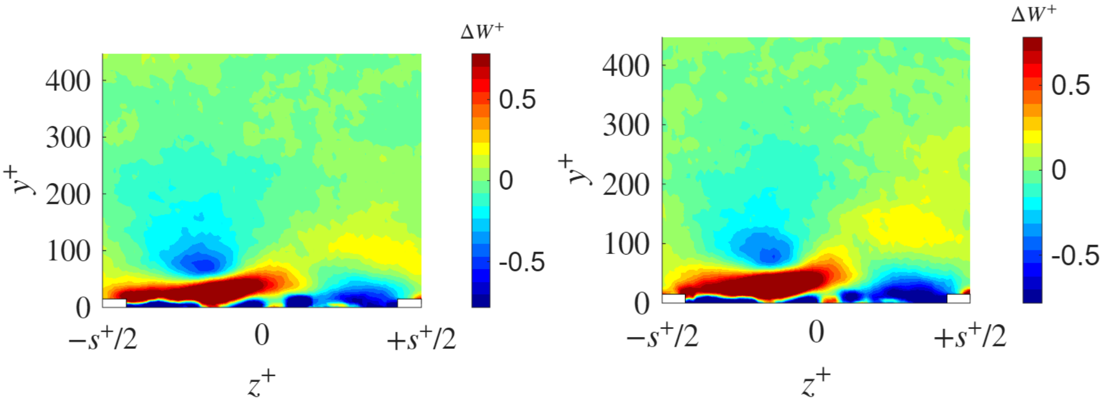

(a) Test case: x1 $Re_\tau = 1300$ $V_{pp} = 14\ kV$. **(b)** Test case: x1 $Re_\tau = 1300$ $V_{pp} = 15.8\ kV$.

Figure 4.9: Induced spanwise velocity fields (ΔW^+) for the two analyzed voltage levels in position $x1$.

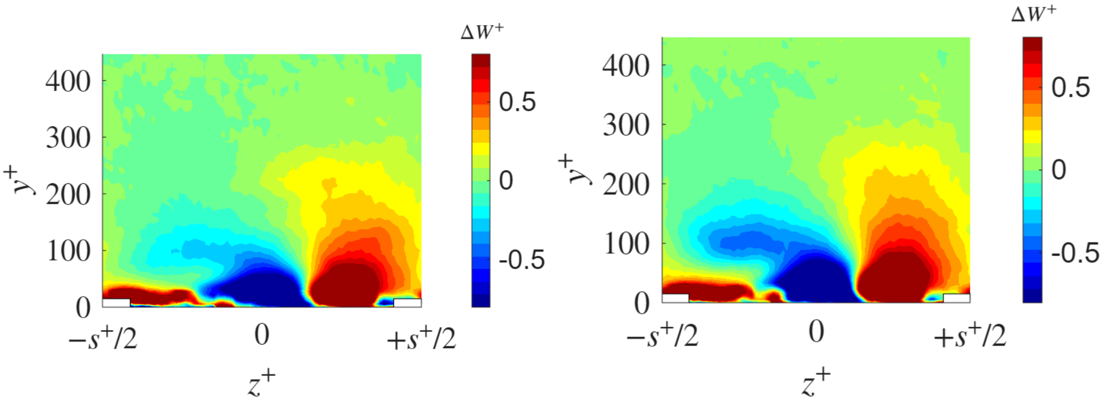

(a) Test case: x2 $Re_\tau = 1300$ $V_{pp} = 14\ kV$. **(b)** Test case: x2 $Re_\tau = 1300$ $V_{pp} = 15.8\ kV$.

Figure 4.10: Induced spanwise velocity fields (ΔW^+) for the two analyzed voltage levels in position $x2$.

The images above reveal a slight effect due to the different V_{pp} applied to the actuator, manifesting as larger and more intense lobes. However, since the potential difference is relatively small, these effects remain marginal. This phenomenon is more clearly observed in the streamwise component. A more detailed visualization of the potential's impact will be provided in Section 4.3. Moreover, the images reveal that the influence of the plasma actuator remains predominantly confined within the first 400 viscous wall units ($y^+ < 400$). Beyond this threshold, the induced effects decay rapidly, becoming negligible as the distance from the wall increases.

An analogous behavior across all velocity components is observed at higher Reynolds numbers, although significant differences emerge in the wall-normal and spanwise components. In both cases, the induced structures appear notably smaller in scale. Specifically, regarding the wall-normal velocity, a substantial reduction in the intensity of the plumes is observed as the flow velocity increases. This is attributed to the fact that the higher momentum of the free-stream flow tends to counteract the vertical lift of the jet, effectively confining the structures closer to the wall and limiting their vertical penetration. Regarding the streamwise component, the perturbation appears to extend toward higher y^+ values and increase in intensity; however, it must be considered that at higher velocities, the viscous length scale decreases.

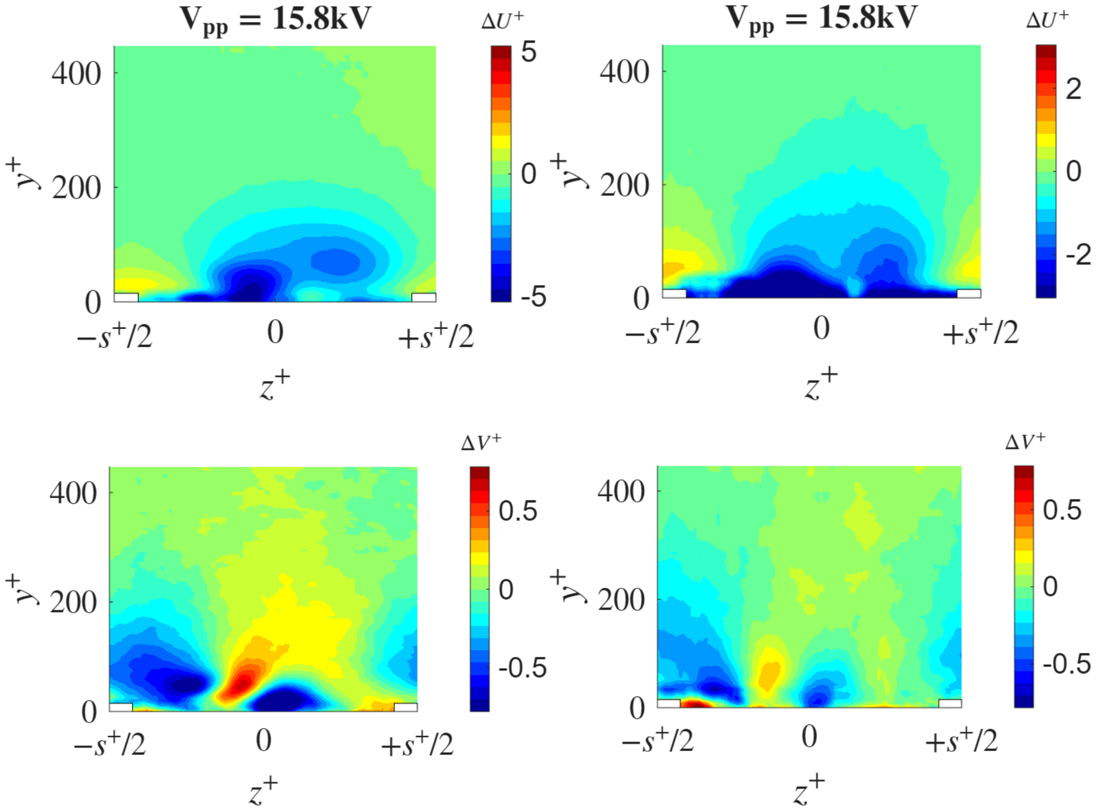

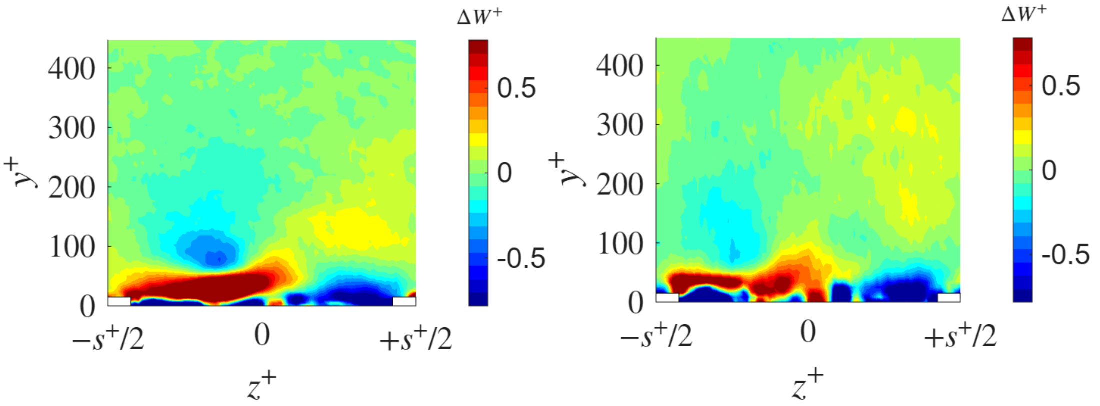

Figure 4.11: Influence of the friction Reynolds number Re_τ on the induced flow field. Cross-stream maps of velocity perturbations in viscous units. $V_{pp} = 15.8\ kV$.Left columns: $Re_\tau = 1300$; Right columns: $Re_\tau = 2300$.

The downstream velocity fields are shown in Figures 4.12 and 4.13. Although the physical measurement location remains constant, the corresponding dimensionless distances from the trailing edge (Δx^+) vary due to the change in the viscous length scale. These values, normalized by the baseline friction length, are summarized in Table 4.4.

U_∞ [m/s]	Δx^+
9	1110
14	1580
16	1915

Table 4.4: Downstream distances from the trailing edge normalized by the friction length of the unactuated case.

Downstream the characteristic structures associated with plasma actuators remain observable, albeit with reduced intensity. Specifically, concerning the streamwise velocity component, a flow deceleration is present in the region between the exposed electrodes. This deceleration becomes more pronounced at higher voltages and free-stream velocities; this is likely attributable to the fact that the flow is more convection-dominated at higher Reynolds numbers. Furthermore, the wall-normal velocity component reveals an upward jet in the intermediate region, flanked by two downwash regions located at the electrodes themselves. Regarding the spanwise component, identifying structures analogous to those observed directly over the actuator becomes increasingly difficult; nevertheless, such features remain discernible at lower Reynolds numbers. This is primarily because, at lower Re_τ, the measurement plane is located at a shorter dimensionless distance (Δx^+) from the trailing edge, where the induced vortices have undergone less spatial decay and turbulent diffusion. For other velocities, the spanwise flow field remains clearly perturbed; it can therefore be hypothesized that the large-scale structures are undergoing a breakup process into smaller, less intense scales. For the sake of brevity, only the two extreme cases, corresponding to the minimum and maximum flow velocities, are presented here. The complete set of analyzed cases is provided in Appendix A.

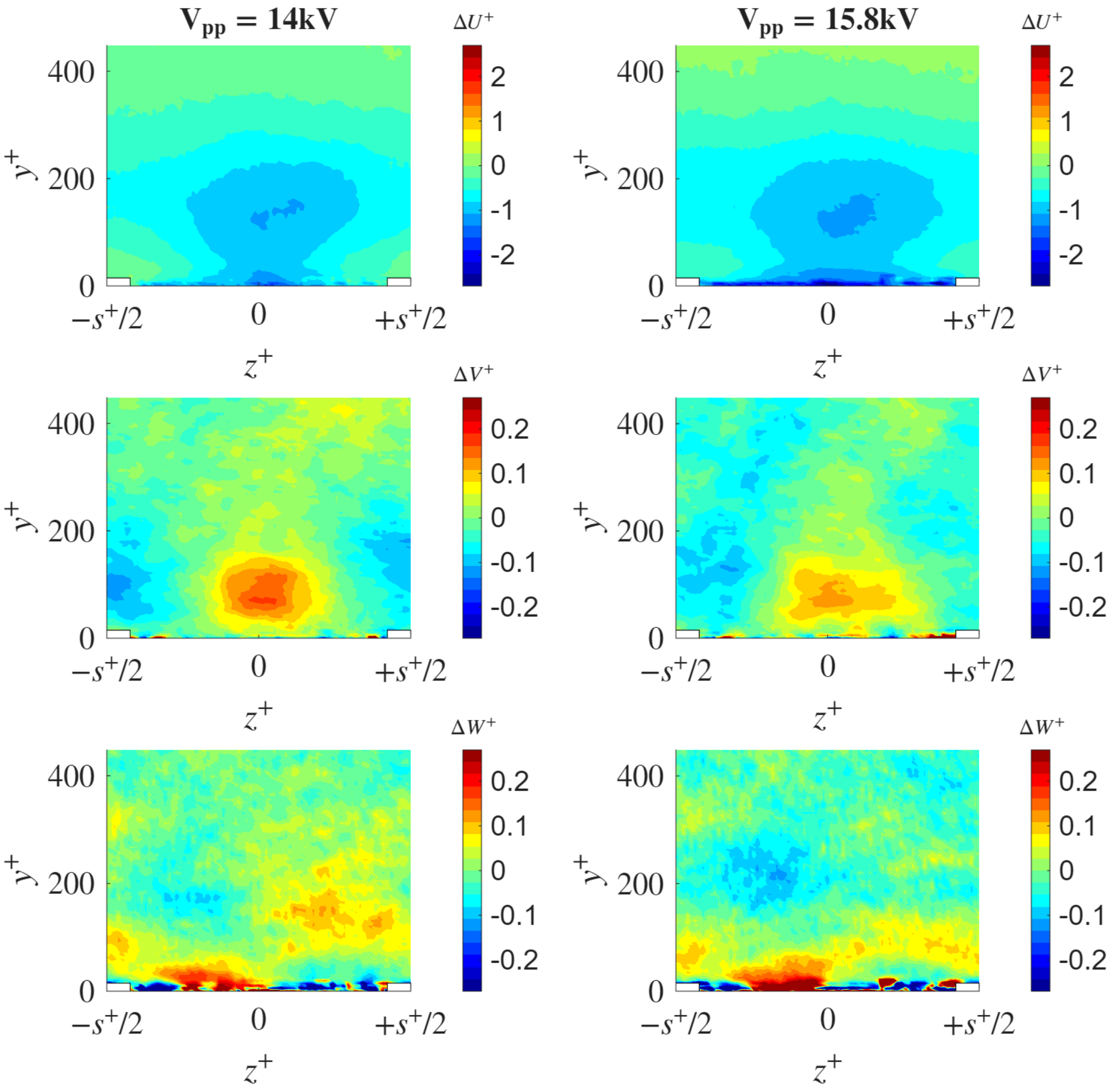

Figure 4.12: Test case: Downstream $Re_\tau = 1300$.

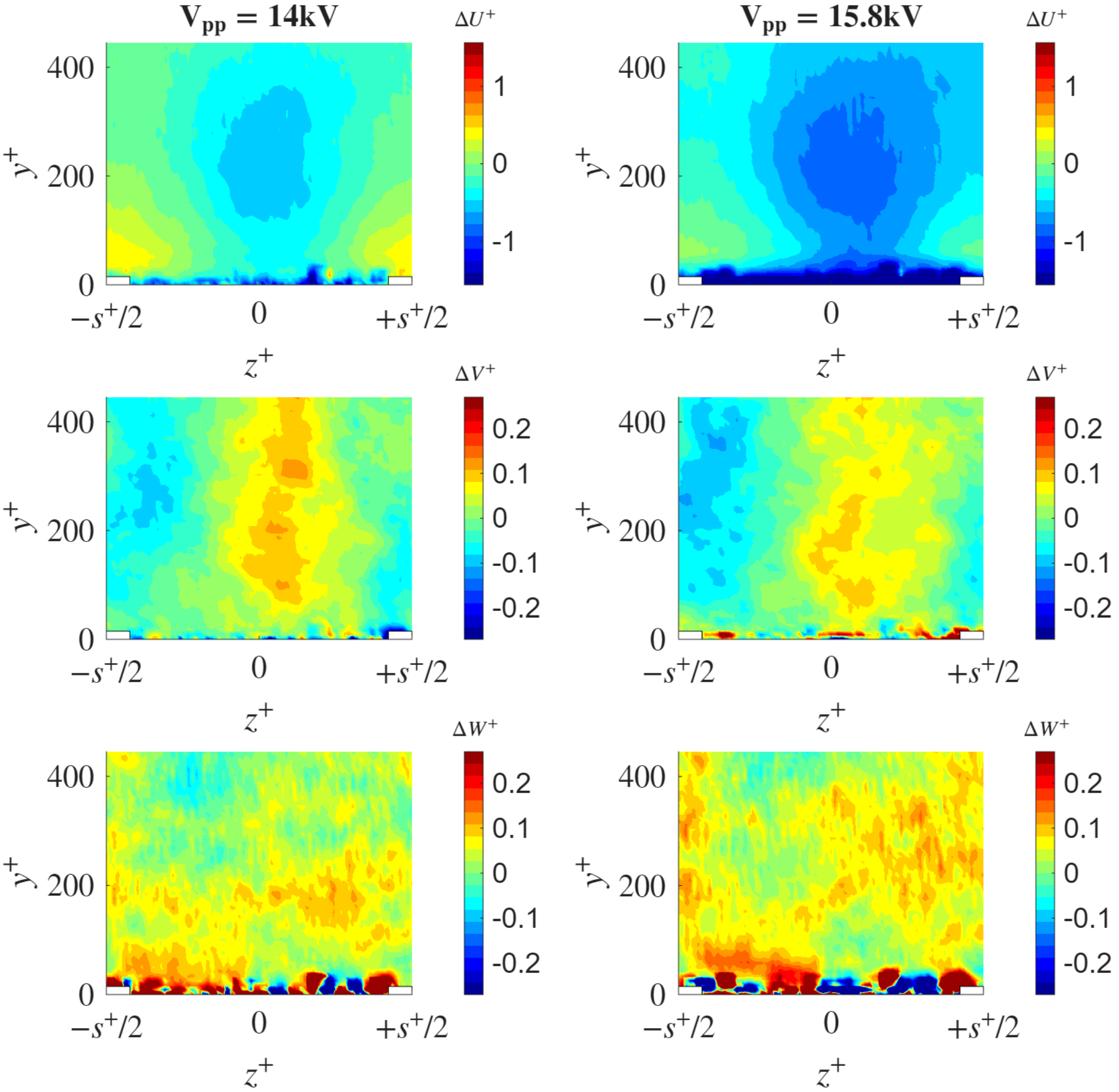

Figure 4.13: Test case: Downstream $Re_\tau = 2300$.

4.3 Voltage Effect

An interesting aspect to investigate is the spanwise velocity distribution as a function of the spacing between two electrodes, see Figure 4.15. Specifically, by plotting the transverse velocity component profiles along the wall-normal direction at various intermediate locations between the electrodes, the following graphs can be derived. Similarly, only specific representative cases are reported in this section; the complete set of analyzed data is provided in Appendix B.

In general, the profiles exhibit a clear resemblance to those obtained in a Stokes layer. The primary difference lies in the boundary conditions: in the case of oscillating walls, the velocity at $y^+ = 0$ matches the wall velocity exactly (and is thus non-zero). In our configuration, this condition does not apply; instead, we observe that the induced velocity peak occurs at approximately $y^+ = 30$. Moving away from the left electrode, a continuous decrease in induced velocity is observed, eventually reaching negative values in the vicinity of the right electrode. Furthermore, the positive induced velocities are higher in magnitude than the negative ones due to the jet superposition effect. Moreover, a higher peak voltage leads to an increase in the induced transverse velocity; however, this difference remains slight, as the gap between the two analyzed voltage levels is not large enough to trigger a significant shift in the plasma-generated body force magnitude. Another interesting observation is the higher induced velocity at increased Reynolds numbers. This can be attributed to the fact that the actuator itself was designed and optimized to operate under high-speed conditions, making it more effective at higher Reynolds numbers than at lower ones. 1. The following reference frame is adopted.

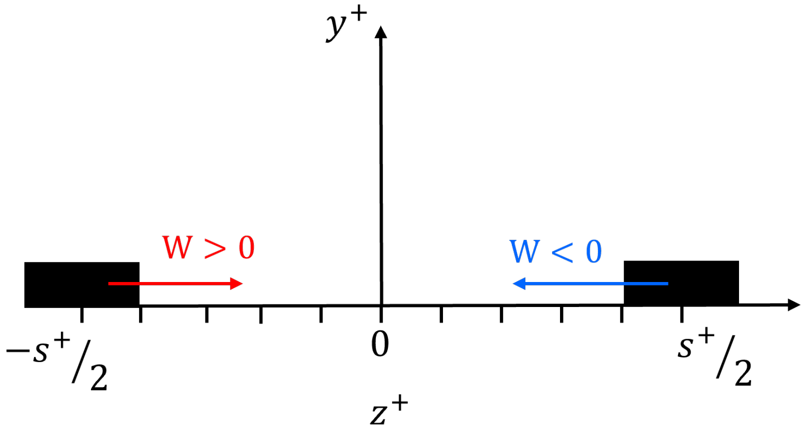

Figure 4.14: Coordinate system and measurement locations.

We shall now proceed to analyze the individual effects of the governing parameters on the flow field.

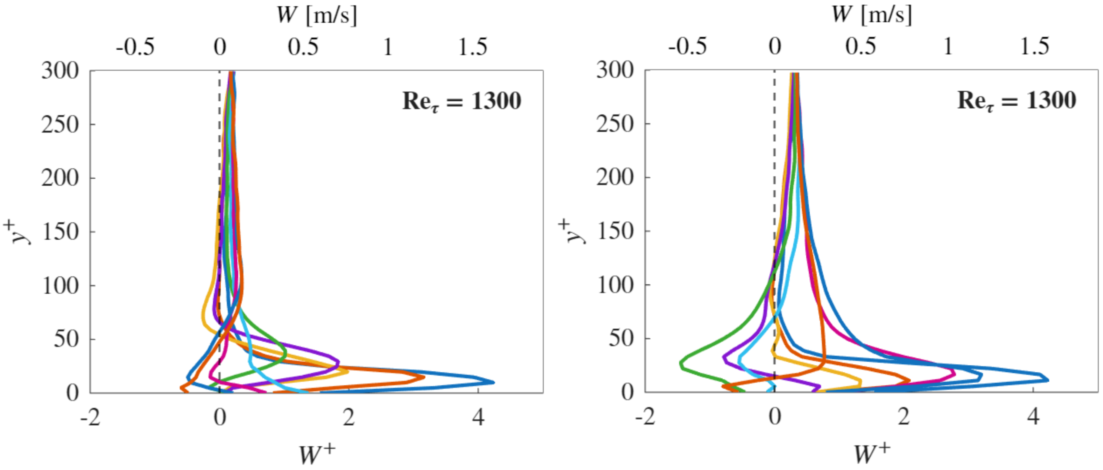

(a) Test case: $x1$, $Re_\tau = 1300$, $V_{pp} = 14\ kV$ **(b)** Test case: $x2$, $Re_\tau = 1300$, $V_{pp} = 14\ kV$

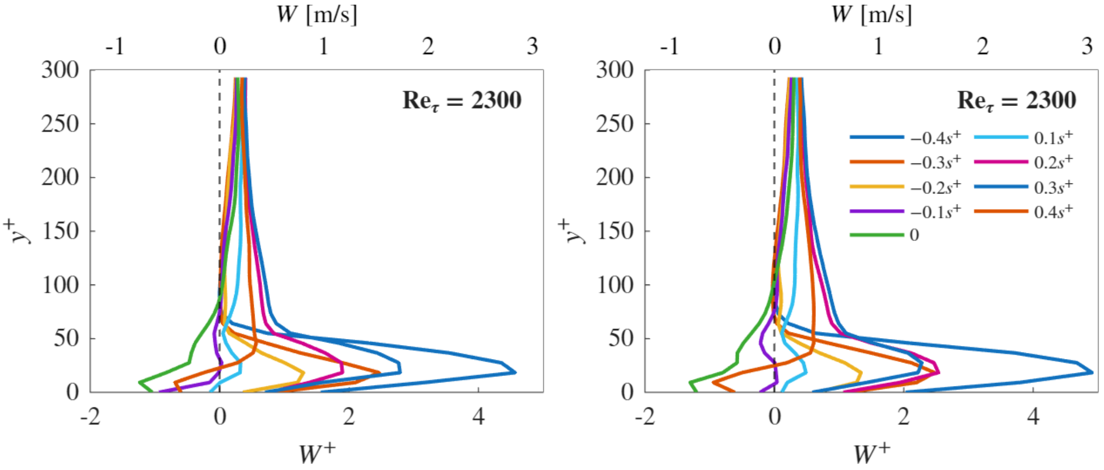

(c) Test case: $x2$, $Re_\tau = 2300$, $V_{pp} = 14\ kV$ **(d)** Test case: $x2$, $Re_\tau = 2300$, $V_{pp} = 15.8\ kV$

Figure 4.15: The spanwise velocity profiles at different in under different operating conditions: (a) baseline case at position x_1; (b) effect of downstream evolution (position x_2); (c) effect of increasing free-stream velocity U_∞ at fixed position; (d) effect of increasing actuation potential V_{pp} at high velocity.

Taking panel 4.15a as a reference ($Re_\tau = 1300$, $V_{pp} = 14$ kV at position $x1$), it can be observed that at position $x2$, the same case exhibits a modulation of the turbulent boundary layer in the spanwise velocity component that extends to higher y^+ values. In fact, while the spanwise component at $x1$ tends to vanish at approximately 150 wall units, at position $x2$ (4.15b), as well as for higher flow velocities, the velocity remains non-zero until significantly higher y^+ levels are reached.

Regarding the effect of the friction Reynolds number, see Figure 4.15c. Higher Re_τ values appear to induce slightly higher velocities. This can be attributed to the fact that the increased flow momentum confines the plasma actuator's effect closer to the wall; consequently, the energy input is concentrated within a thinner near-wall region, leading to higher localized induced velocities.

Finally, concerning the actuation voltage, a slight increase in velocity is also noted at higher V_{pp} (4.15d). However, the potential difference is not large enough to produce a substantial enhancement of the induced flow field.

Analyzing the effect of voltage on the other velocity components, the results are presented in Figure 4.16. These profiles are shown with the non-actuated (no-plasma) baseline subtracted to highlight the net effect of the actuation. Specifically, the impact of voltage was investigated at two fixed wall-normal heights: $y^+ \approx 30$, which roughly corresponds to the peak of the induced spanwise velocity, and at $y^+ \approx 130$, where the effect is still detectable, although significantly reduced. In general, the effect of the plasma actuator decreases as the distance from the wall increases. Conversely, in the near-wall region, the average effect is slightly stronger when the actuator is driven at higher voltages, as expected.

Regarding position $x1$ and the wall-normal component, two peaks separated by a central depression can be observed. This behavior is consistent with the previously described recirculation bubble. Moreover, even at different driving voltages, the peak associated with the left electrode produces a higher wall-normal velocity compared to that induced by the right electrode; this effect is attributable to the sinusoidal geometry of the electrode and to the constructive superposition of the induced jets in the case of the left electrode.

For position $x2$, the induced velocities of the wall-normal component are larger than those observed in case $x1$. This is due to a stronger interaction between the two plasma-induced jets. Several studies have shown that the effectiveness of plasma actuators depends on the spacing between the electrodes, and that smaller spacing can result in greater drag reduction since drag is correlated with the upwash regions generated by the actuator. Another feature observed at position $x2$ is that the plume is not located exactly at the midpoint between the two electrodes, but is shifted toward the right. This is because the electrodes are not perpendicular to the laser plane; consequently, the plasma-induced jet does not lie within the measurement plane.

As previously highlighted in the velocity fields, regarding the streamwise component, we observe flow deceleration in the region between the exposed electrodes, whereas acceleration occurs in correspondence with them. This deceleration is slightly more pronounced at lower Reynolds numbers.

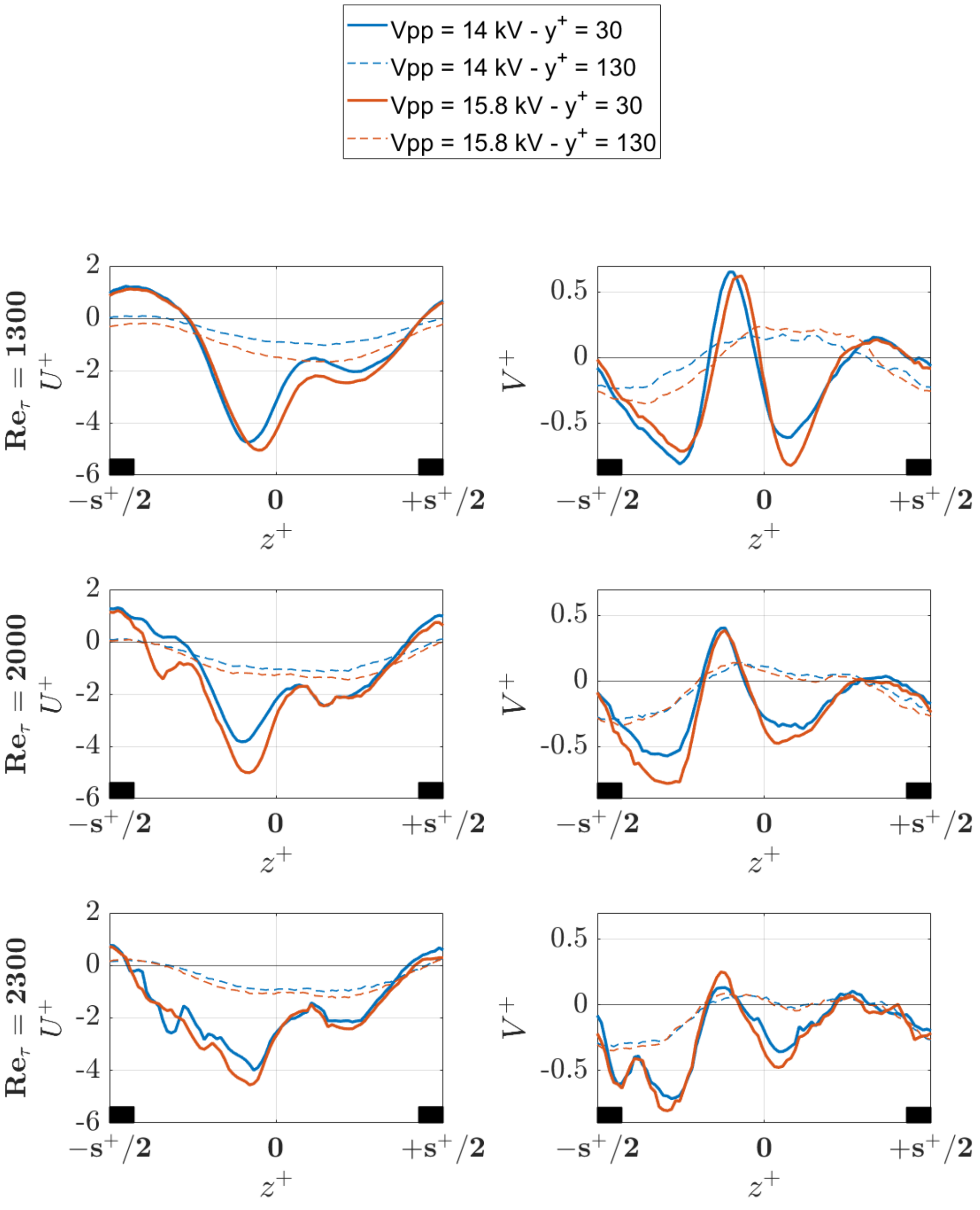

(a) Position: $x1$.

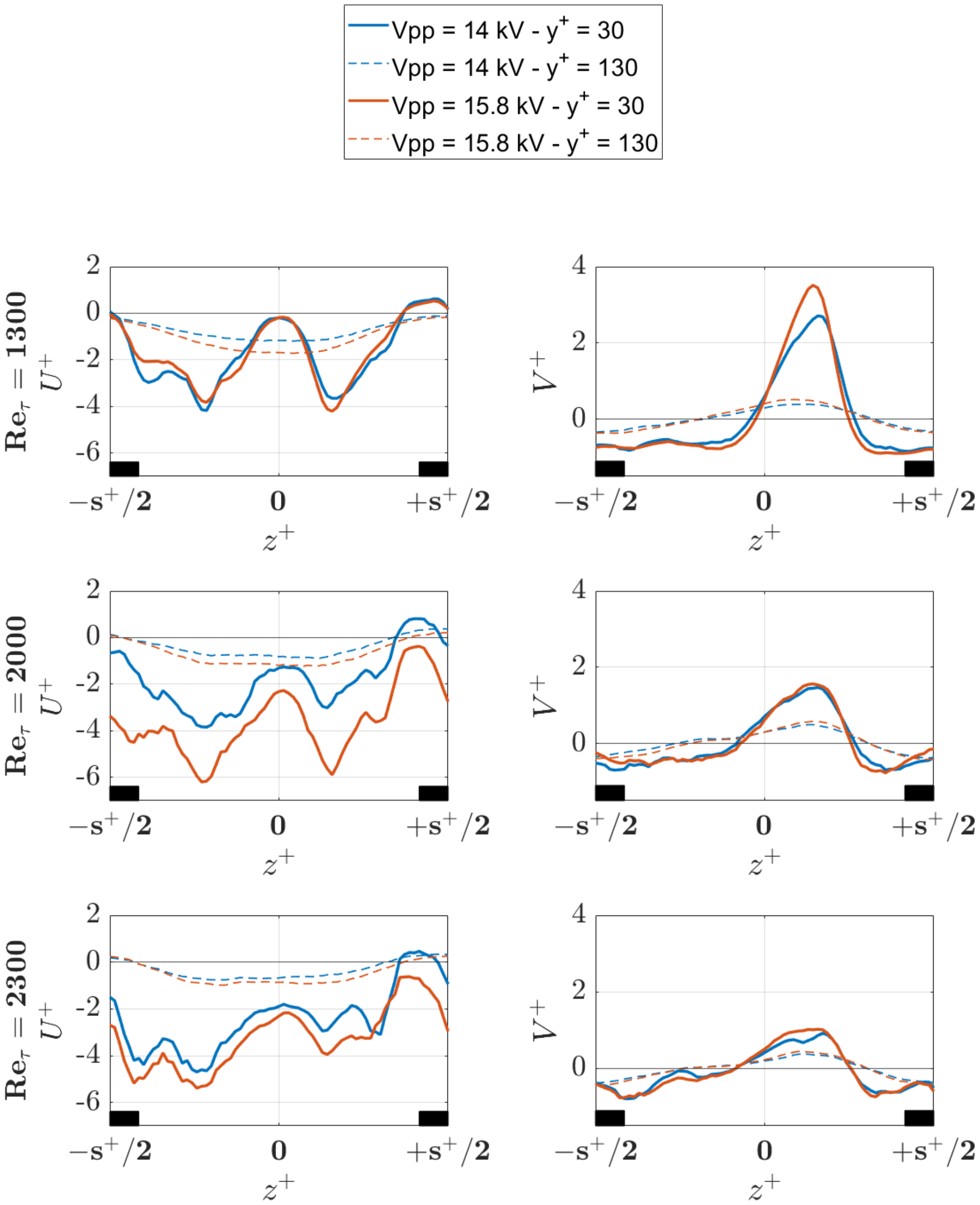

(b) Position: $x2$.

Figure 4.16: Effects of voltage variation on the streamwise and wall-normal velocity profiles at different Reynolds numbers in position $x1$ and $x2$ at $y^+ = 30$ and $y^+ = 130$.

4.4 Reynolds Stresses

In this section, the Reynolds stresses are analyzed, focusing on their evolution across different streamwise positions and their sensitivity to variations in peak-to-peak voltage and friction Reynolds number (Re_τ). Specifically, the profiles of the $\overline{uu}^+$ and $\overline{uv}^+$ components are presented, as these components are central to assessing potential drag reduction in the streamwise direction. These profiles are obtained by averaging the experimental data in both time and the spanwise direction. To ensure a consistent comparison across different test cases, the profiles are normalized using the viscous scales (u_τ, δ_ν) of the corresponding unactuated (baseline) case.

The following figure (4.17) illustrates the $\langle uu \rangle^+$ component of the Reynolds stress tensor at different peak-to-peak voltages (V_{pp}), providing a direct comparison with both the unactuated baseline and the reference DNS data. In general terms, it can be observed that the presence of plasma actuation leads to a noticeable reduction in Reynolds stresses in the near-wall region. This trend holds true for the majority of the investigated conditions, with the notable exception of the $x1$ position at $Re_\tau = 1300$. This specific discrepancy might be attributed to several factors; however, it is likely suggestive of measurement uncertainty, given that a reduction in stress is again observed at higher flow velocities. A common feature across all tested configurations is the emergence of a secondary peak located within the log-layer, approximately at 100 wall units, where the unactuated case typically displays a plateau. This secondary maximum appears to migrate further away from the wall as the flow moves toward the downstream position. This behavior suggests that, even in regions where the direct influence of the actuator is no longer present, the turbulence tends to be displaced toward the outer flow, further from the solid boundary. Regarding the influence of the actuation voltage, a slightly more intense effect can be identified, with the observed modifications to the Reynolds stress profiles becoming more pronounced at higher peak-to-peak voltages. The remaining analyzed cases are reported in Appendix C.

Regarding the Reynolds shear stress ($-\langle u'v' \rangle^+$), a reduction in near-wall stresses is observed compared to the unactuated baseline. Similar to the previous observations, a secondary peak emerges at approximately 100 wall units for $x1$ and $x2$ positions. This peak appears to migrate toward higher y^+ values in the downstream direction, while simultaneously increasing in intensity. These features are consistent across all test cases, with slightly more pronounced effects identified at higher actuation voltages.

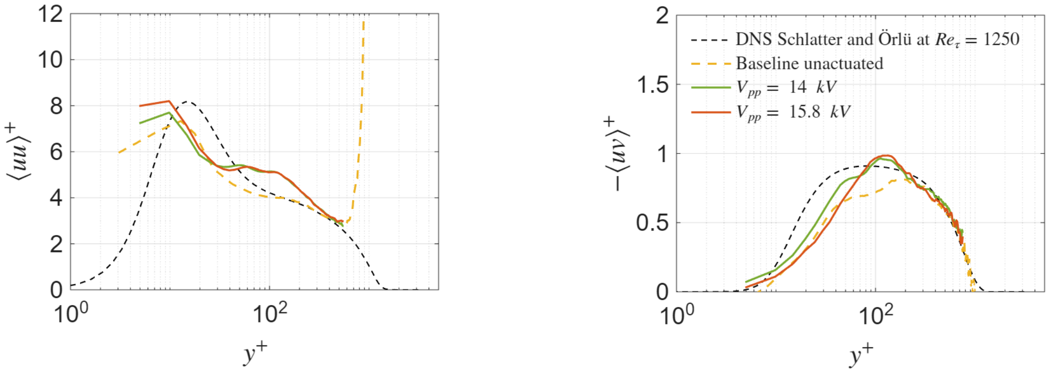

(a) Test case: $x1$, $Re_\tau = 1300$, $\langle uu \rangle^+$ **(b)** Test case: $x1$, $Re_\tau = 1300$, $\langle uv \rangle^+$

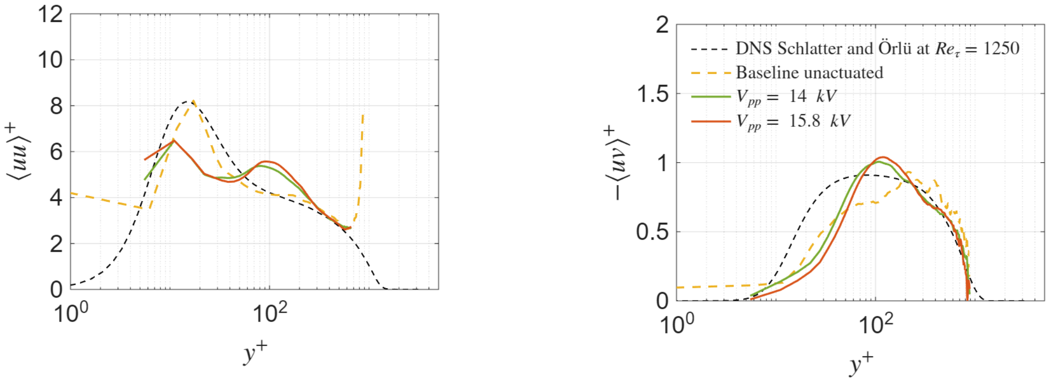

(c) Test case: $x2$, $Re_\tau = 1300$, $\langle uu \rangle^+$ **(d)** Test case: $x2$, $Re_\tau = 1300$, $\langle uv \rangle^+$

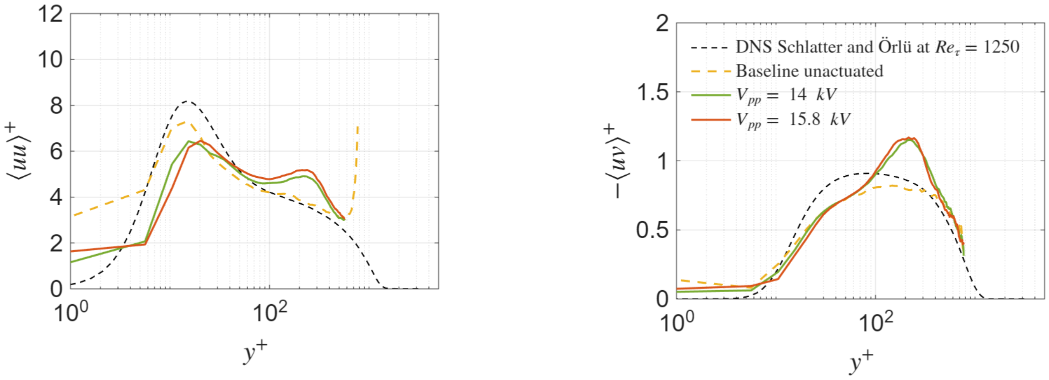

(e) Test case: $x3$, $Re_\tau = 1300$, $\langle uu \rangle^+$ **(f)** Test case: $x3$, $Re_\tau = 1300$, $\langle uv \rangle^+$

Figure 4.17: Evolution of the streamwise Reynolds stress profiles ($\langle uu \rangle^+$ on the left) and Reynolds shear stress ($\langle uv \rangle^+$ on the right) at a fixed $Re_\tau = 1300$ for different downstream positions: (a) $x1$, (b) $x2$, and (c) $x3$. The plots compare the DNS results (dashed line) and the unactuated baseline (yellow dashed line) with the actuated cases at $V_{pp} = 14$ kV (green) and $V_{pp} = 15.8$ kV (orange).

We shall now examine the potential influence of the Reynolds number by analyzing the behavior of the Reynolds stresses at different flow velocities, see Figure 4.18. To maintain clarity and avoid overcrowding the plots, only the minimum and maximum velocities investigated are presented, both at a constant actuation potential of 15.8 kV. In the following figures, the black dashed line represents the reference DNS data, while the colored dashed lines correspond to the unactuated baseline cases at their respective Reynolds numbers: red for $Re_\tau = 1300$ and blue for $Re_\tau = 1600$. The solid lines represent the actuated conditions. While the observed trends remain consistent across all tested voltages, the 15.8 kV case is selected for this comparison to better highlight the phenomena, as the effects are more pronounced at higher potentials (see Appendix C).

Regarding the streamwise Reynolds stress component ($\langle uu \rangle^+$), no significant modifications are observed in the near-wall region as Re_τ varies; consequently, the Reynolds number effect near the wall can be considered negligible. However, notable variations emerge in the logarithmic region, particularly concerning the induced secondary peak. As the velocity increases, this secondary peak tends to migrate toward higher y^+ values. Furthermore, it is no longer sharply localized; instead, the fluctuation intensity tends to be distributed over a wider range of y^+ values.

A similar trend is observed for the Reynolds shear stress component ($\langle uv \rangle^+$), where the peak shifts toward higher y^+ levels with increasing velocity. Additionally, consistent with the streamwise Reynolds stress, the observed effects on the Reynolds shear stress profiles appear to be less intense at higher Reynolds numbers.

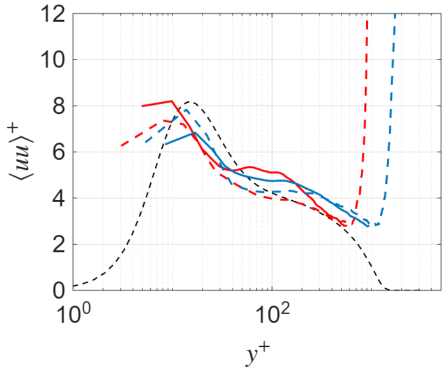

(a) Test case: $x1$, $V_{pp} = 15.8$ kV, $\langle uu \rangle^+$

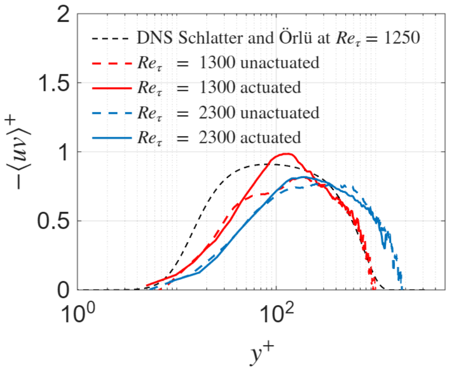

(b) Test case: $x1$, $V_{pp} = 15.8$ kV, $\langle uv \rangle^+$

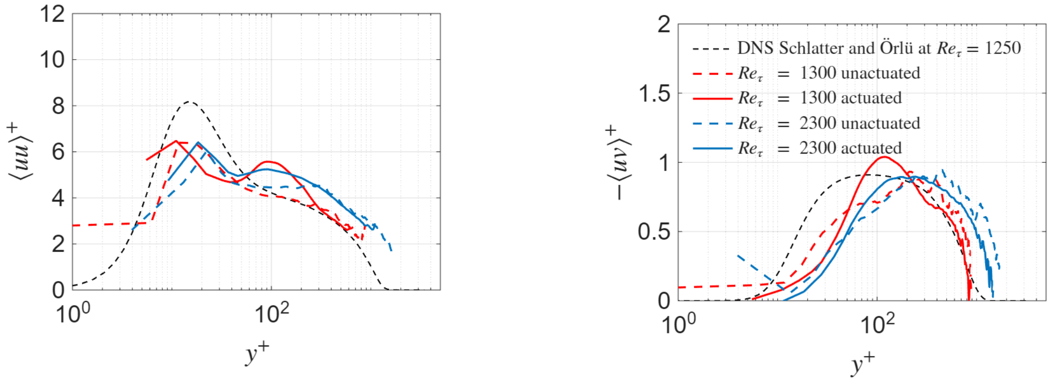

(c) Test case: $x2$, $V_{pp} = 15.8$ kV, $\langle uu \rangle^+$ **(d)** Test case: $x2$, $V_{pp} = 15.8$ kV, $\langle uv \rangle^+$

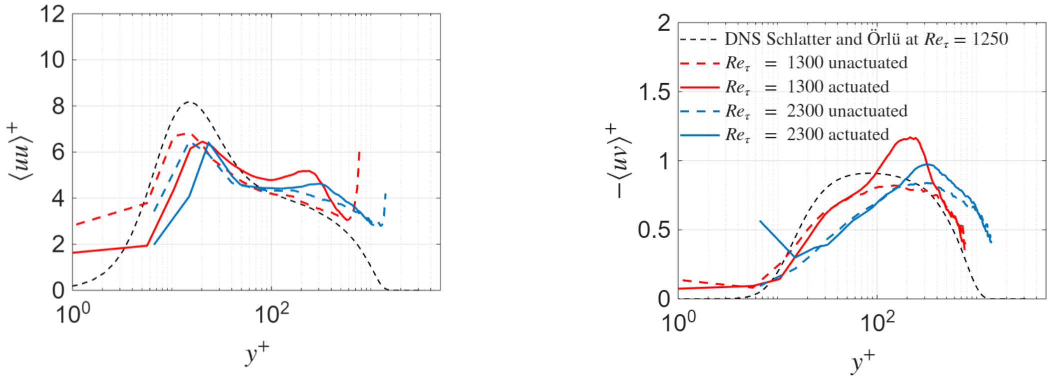

(e) Test case: $x3$,$V_{pp} = 15.8$ kV, $\langle uu \rangle^+$ **(f)** Test case: $x3$, $V_{pp} = 15.8$ kV, $\langle uv \rangle^+$

Figure 4.18: Evolution of the streamwise Reynolds stress profiles ($\langle uu \rangle^+$ on the left) and Reynolds shear stress ($\langle uv \rangle^+$ on the right) at a fixed $V_{pp} = 15.8\ kV$ for different downstream positions: (a) $x1$, (b) $x2$, and (c) $x3$. The plots compare the DNS results (dashed line) and the unactuated baseline (yellow dashed line) with the actuated cases at $Re_\tau = 1300$ (red) and $Re_\tau = 2300$ (blue).

Chapter 5

Conclusions

The experimental activity conducted has allowed for an extensive analysis of the interaction between sinusoidal geometry plasma actuators and the turbulent boundary layer, providing more information on the effects of turbulent boundary layer manipulation through plasma actuators with unconventional geometries.

Stereoscopic PIV measurements in the cross-flow plane reveal that the interaction of the induced spanwise wall jets generates well-defined, coherent three-dimensional structures; the actuation effect is not limited to the spanwise component alone, but involves all components, significantly modifying the local structure of the boundary layer. In particular, the collision of the transverse wall jets produces plumes directed in the wall-normal direction, resulting in an alternating spatial distribution of upwash and downwash regions. The central zones between the electrodes are characterized by upward motion, while above the electrodes, flow entrainment towards the wall is observed. The ejection of, on average, slower flow away from the wall leads to a reduction in velocity along the streamwise direction; conversely, near the electrodes, an acceleration of the flow along the same direction is observed.

It is established that the distance between electrodes plays an important role in the genesis of the so-called plumes: indeed, precisely due to the variation in spacing between the electrodes moving streamwise, significant differences in the flow fields emerged between positions $x1$ and $x2$. Since the spacing is greater in $x1$, it does not allow for an optimal interaction of the jets, and this translates into less intense plumes and flow modulation confined to lower y^+. The downstream flow fields highlighted how the modulation remains coherent in space even where the actuator is not present, still showing significant but less intense variations, especially for the streamwise and wall-normal components.

During the experimental campaign, the effects of various parameters were analyzed, such as the influence of the friction Reynolds number and the peak-to-peak voltage imposed on the actuator. A fundamental aspect that emerged is the role of the supply voltage: an increase in voltage leads to an increase, albeit minimal given the small input variation investigated, in the induced velocities. This effect is maintained even at higher Reynolds numbers, demonstrating its effectiveness even in more energetic flow conditions.

From the profiles of the transverse velocity component along the wall-normal direction, taken at different intermediate positions between the two electrodes, it emerges that more intense transverse jets are induced at higher velocities. This behavior can be interpreted by considering that the increase in Re_τ leads to a decrease in the boundary layer thickness and, therefore, to a compression of the structures toward the wall. The energy introduced by the actuator remains physically confined closer to the wall, thus leading to more intense transverse jets.

The analysis of Reynolds stresses highlighted changes in the distribution of turbulent fluctuations, suggesting a direct interaction between the structures generated by the actuator and the mechanisms of turbulence production. Particular attention was given to the $\langle uu \rangle^+$ and $\langle uv \rangle^+$ components, as they are more relevant for determining a possible drag reduction along the streamwise direction. In general, above the actuator, Reynolds stresses increase at approximately 200 wall units from the wall, where a distinct peak emerges compared to the non-actuated case. This peak tends to shift away from the wall and intensify in the downstream position. Near the wall, a reduction in Reynolds stresses compared to the non-actuated case is generally observed; however, the measurement shows some uncertainties at these scales due to signal noise from laser reflections and the presence of the plasma. As Re_τ increases, the profiles remain relatively unaltered near the wall, while a shift of the external peak toward higher y^+ and a flattening of the peak itself are observed.

The analyzes conducted in this work provide a solid benchmark for the systematic comparison between sinusoidal geometry actuators and more traditional configurations. Although the results have identified several indicators of potential drag manipulation, the current experimental setup does not allow for a direct quantification of skin-friction resistance.

Looking toward future developments, two main directions are proposed: the implementation of techniques for the direct measurement of skin friction (τ_w), which are essential for obtaining a quantitative estimate of drag reduction, and the manufacturing of PCB-printed actuators. The latter would eliminate the undesirable effects of dielectric flexing caused by thermal stresses, ensuring a more stable electrode geometry and enhancing the repeatability and reliability of the tests. Furthermore, the use of PCB technology could allow for testing across a broader range of voltages by reducing the risk of arcing, thereby increasing the overall durability and operational authority of the device.

Appendix A

Velocity Fields

Figure A.1: Test case: $x1$ $Re_\tau = 1300$.

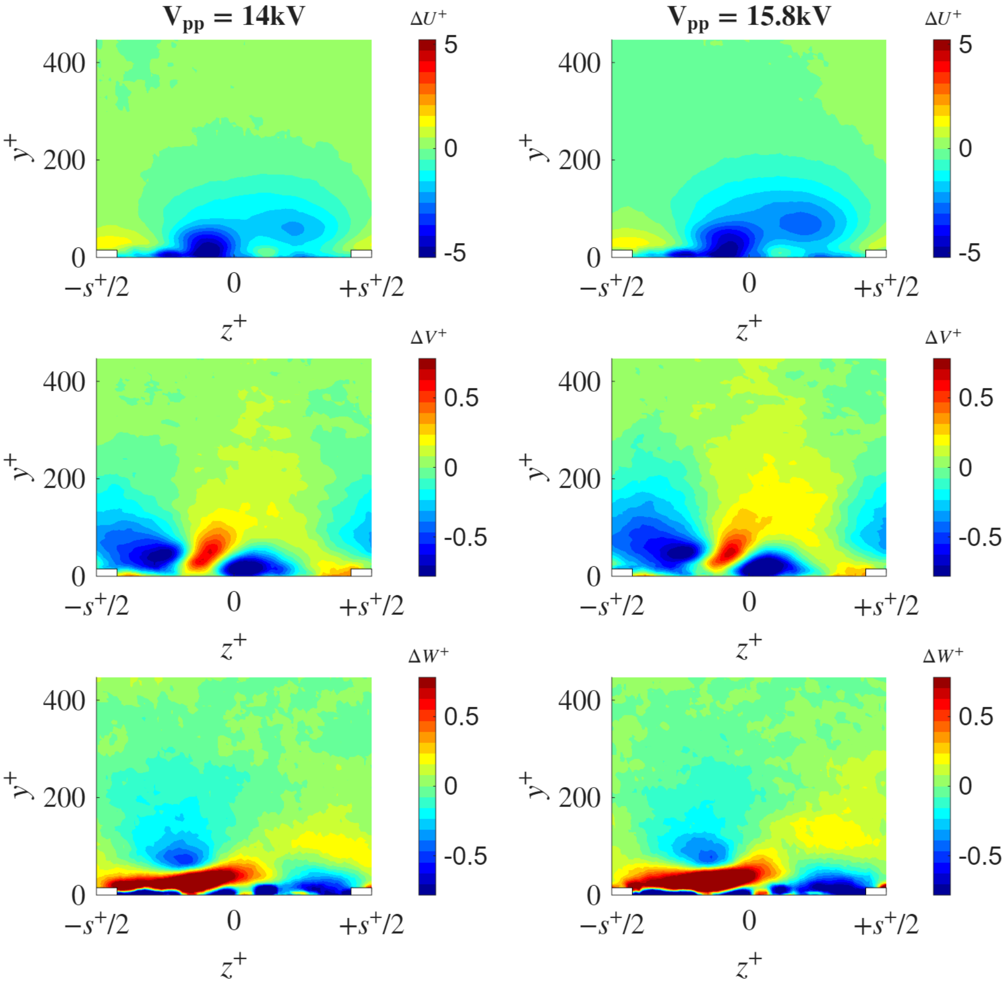

Figure A.2: Test case: $x1$ $Re_\tau = 2000$.

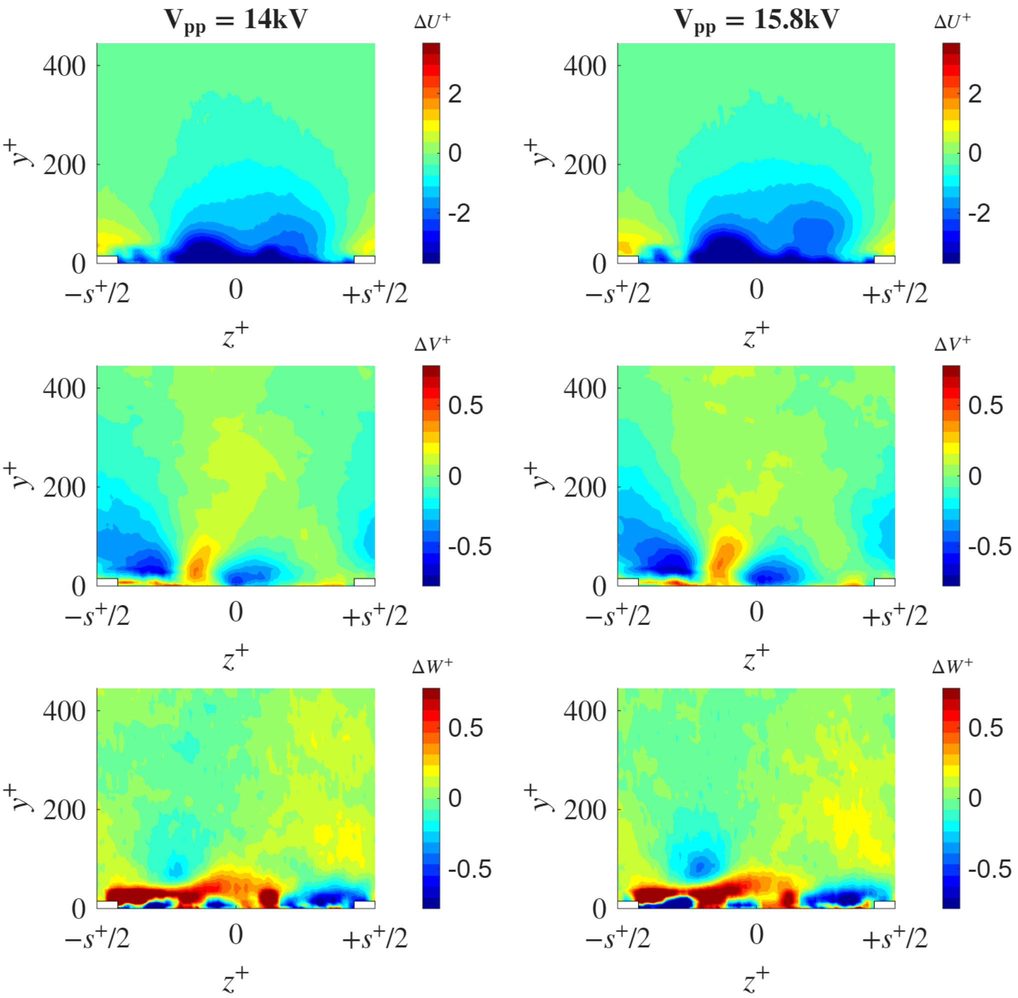

Figure A.3: Test case: $x1$ $Re_\tau = 2300$.

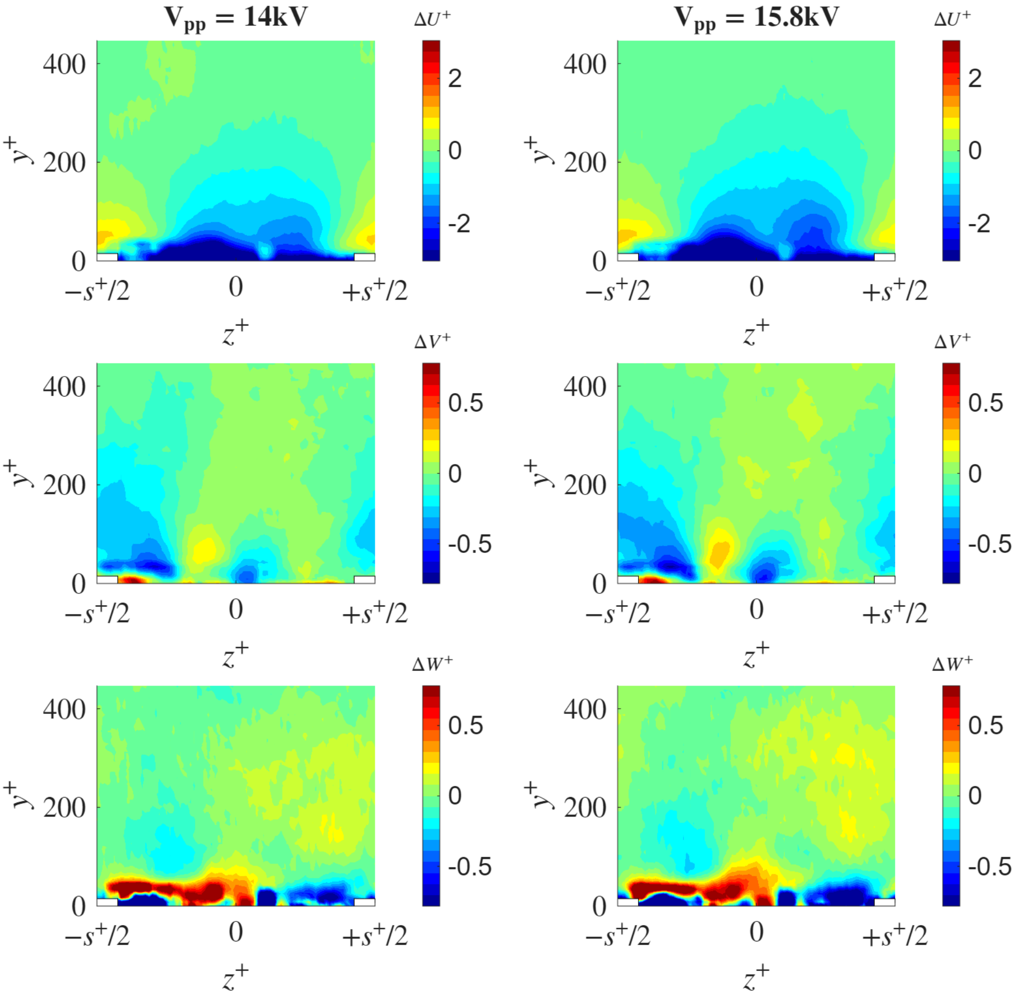

Figure A.4: Test case: $x2$ $Re_\tau = 1300$.

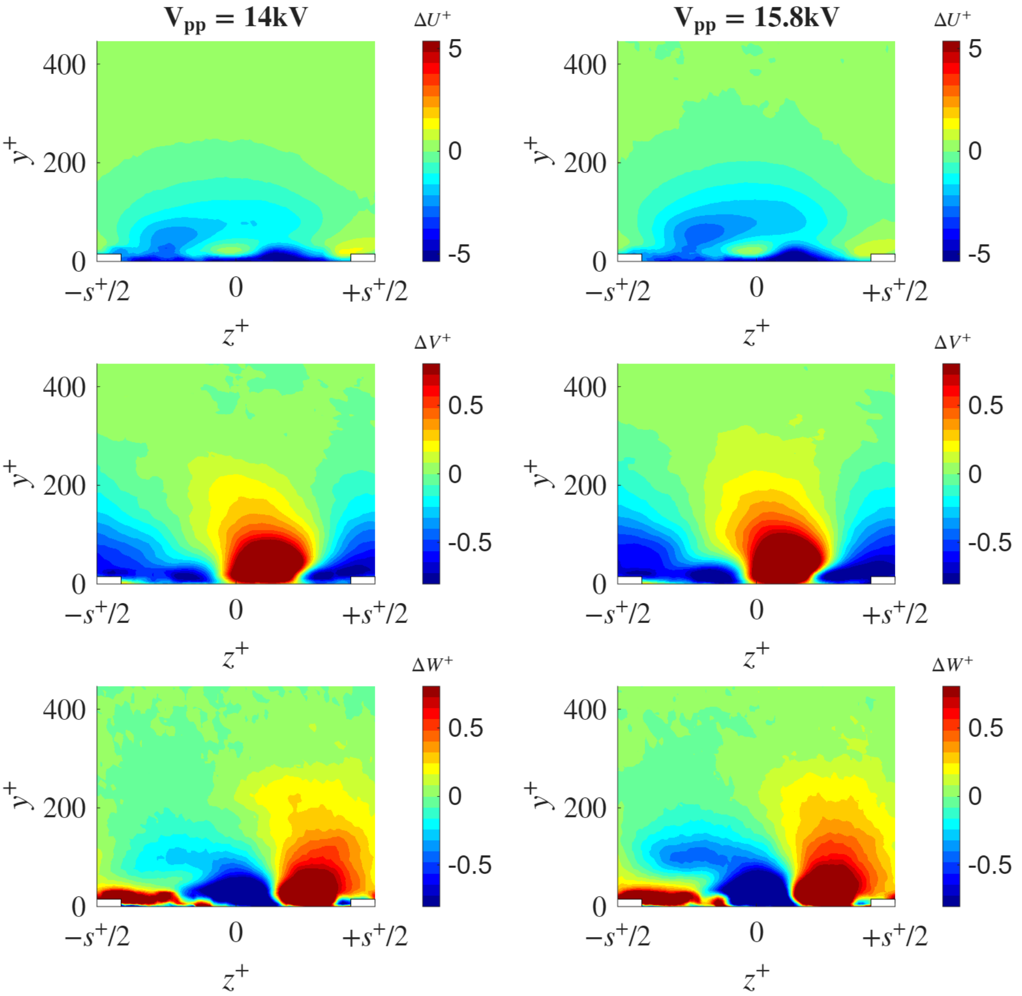

Figure A.5: Test case: $x2$ $Re_\tau = 2000$.

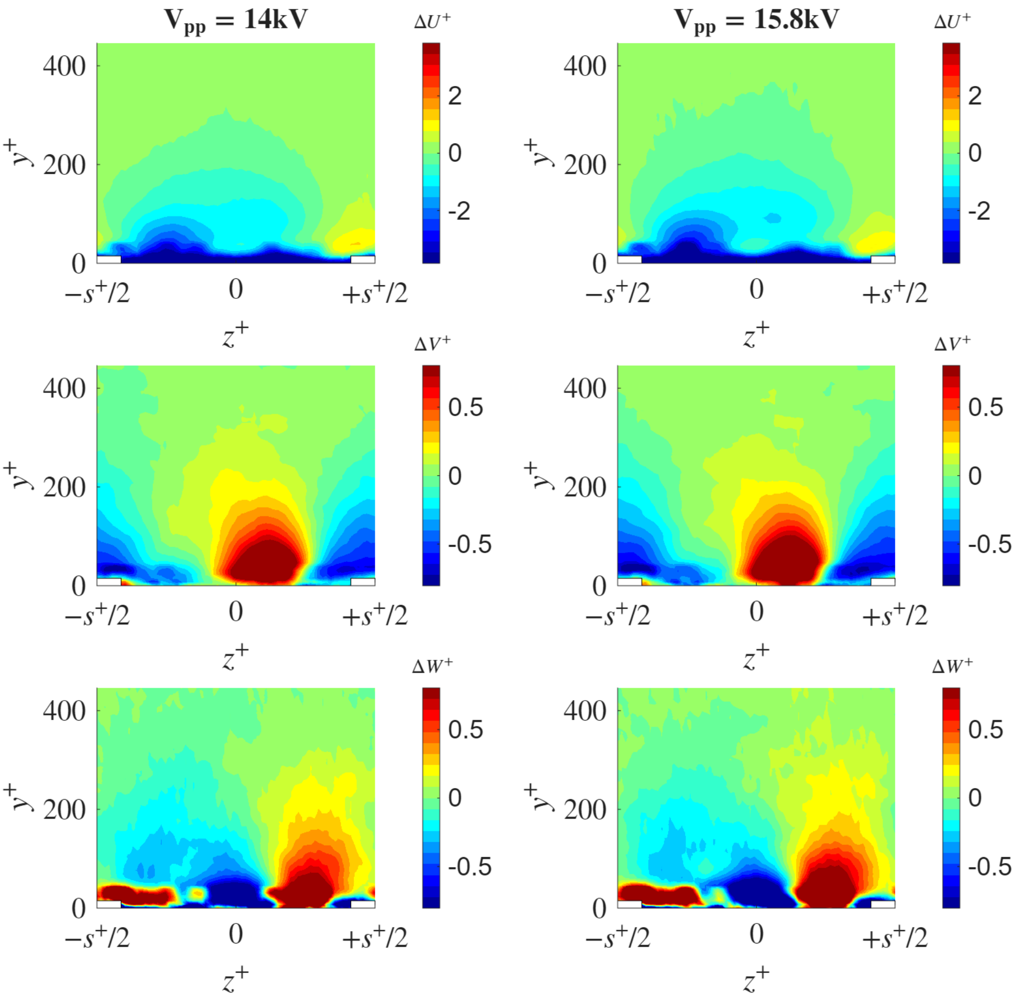

Figure A.6: Test case: $x2$ $Re_\tau = 2300$.

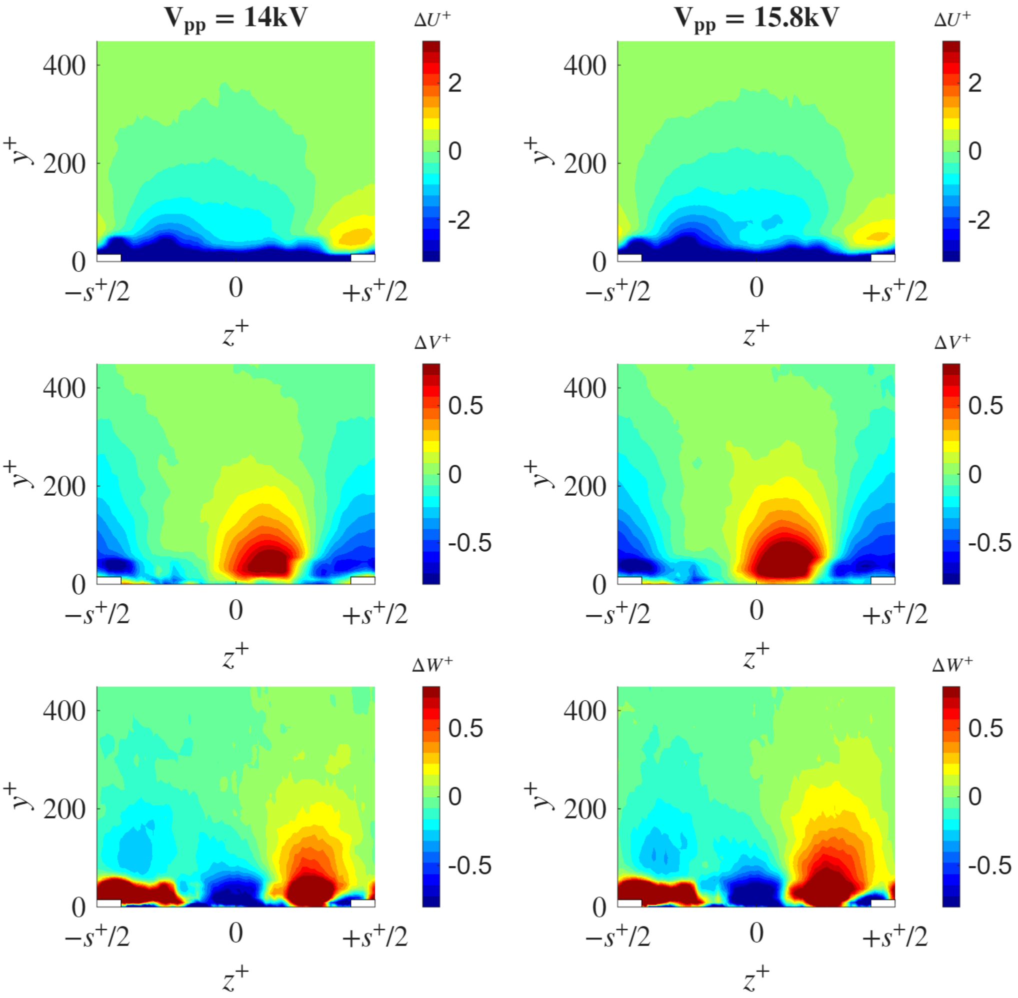

Figure A.7: Test case: $x3$ $Re_\tau = 1300$.

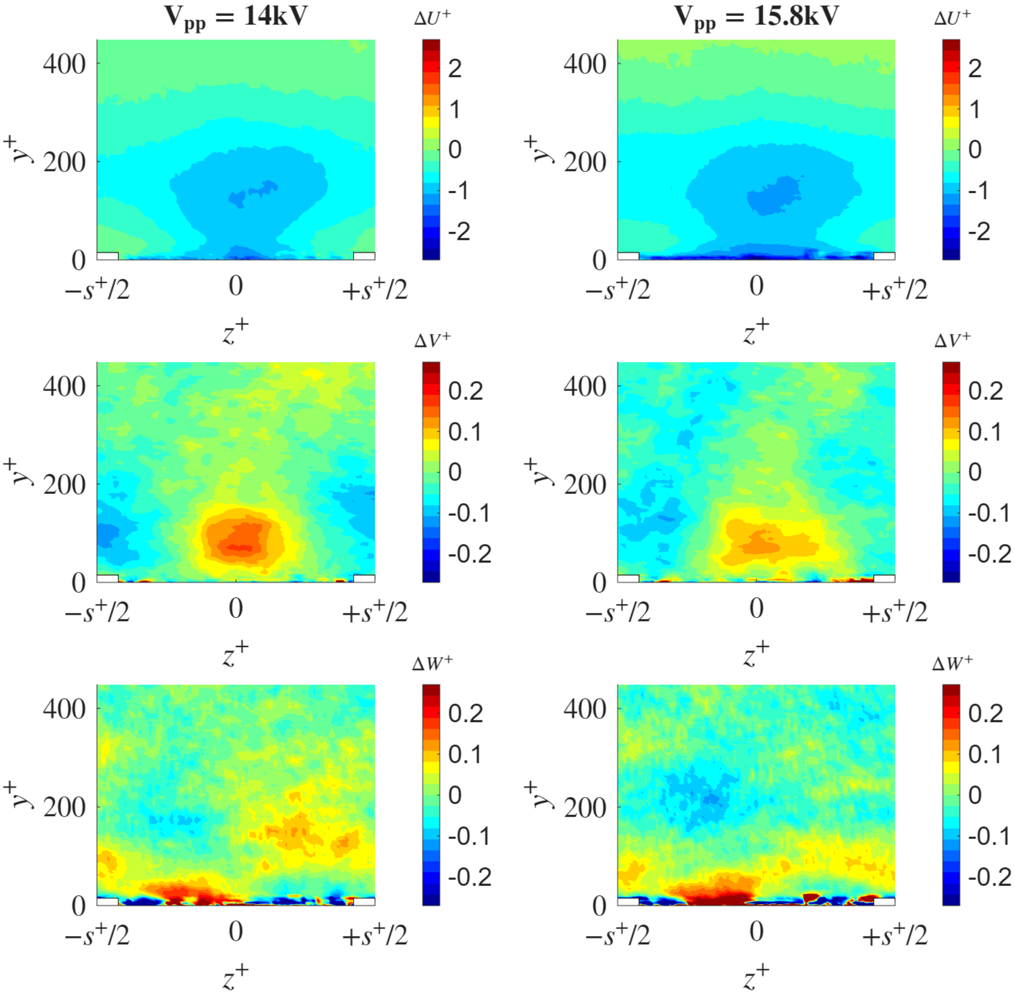

Figure A.8: Test case: $x3$ $Re_\tau = 2000$.

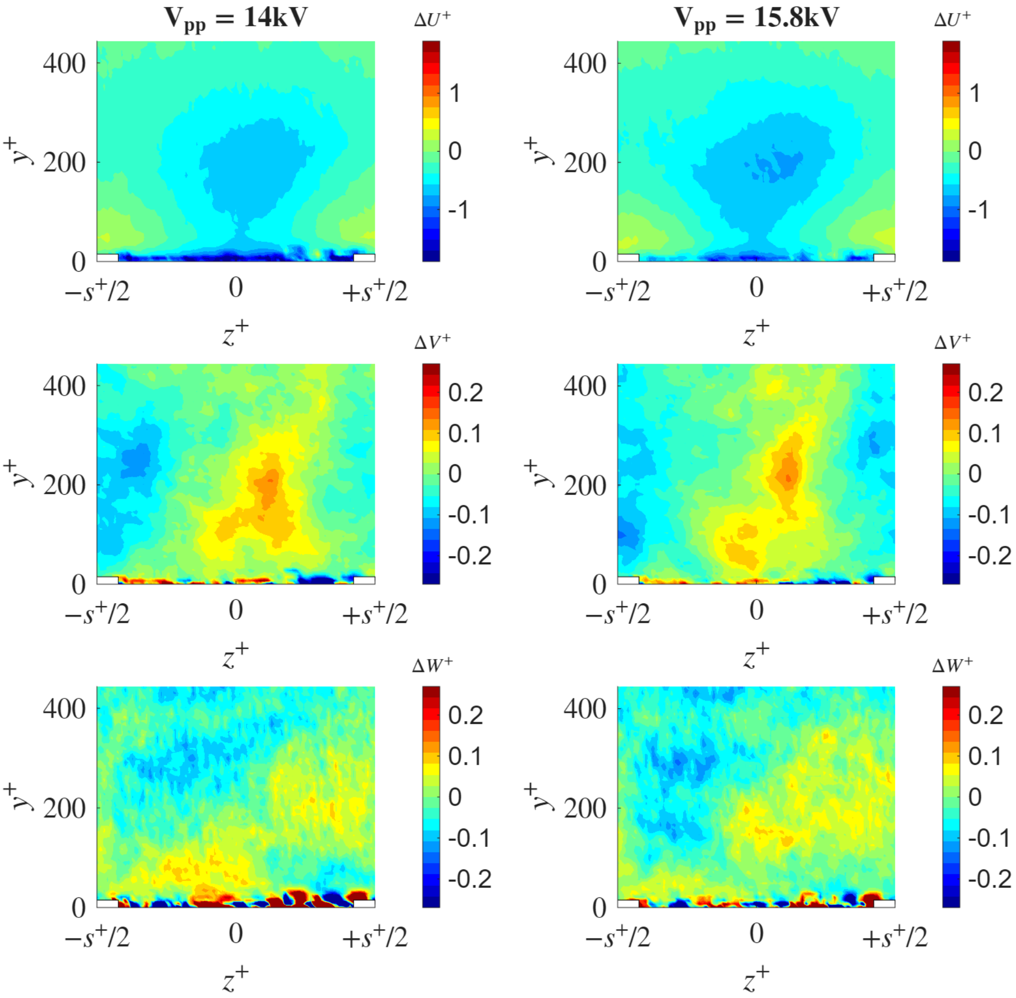

Figure A.9: Test case: $x3$ $Re_\tau = 2300$.

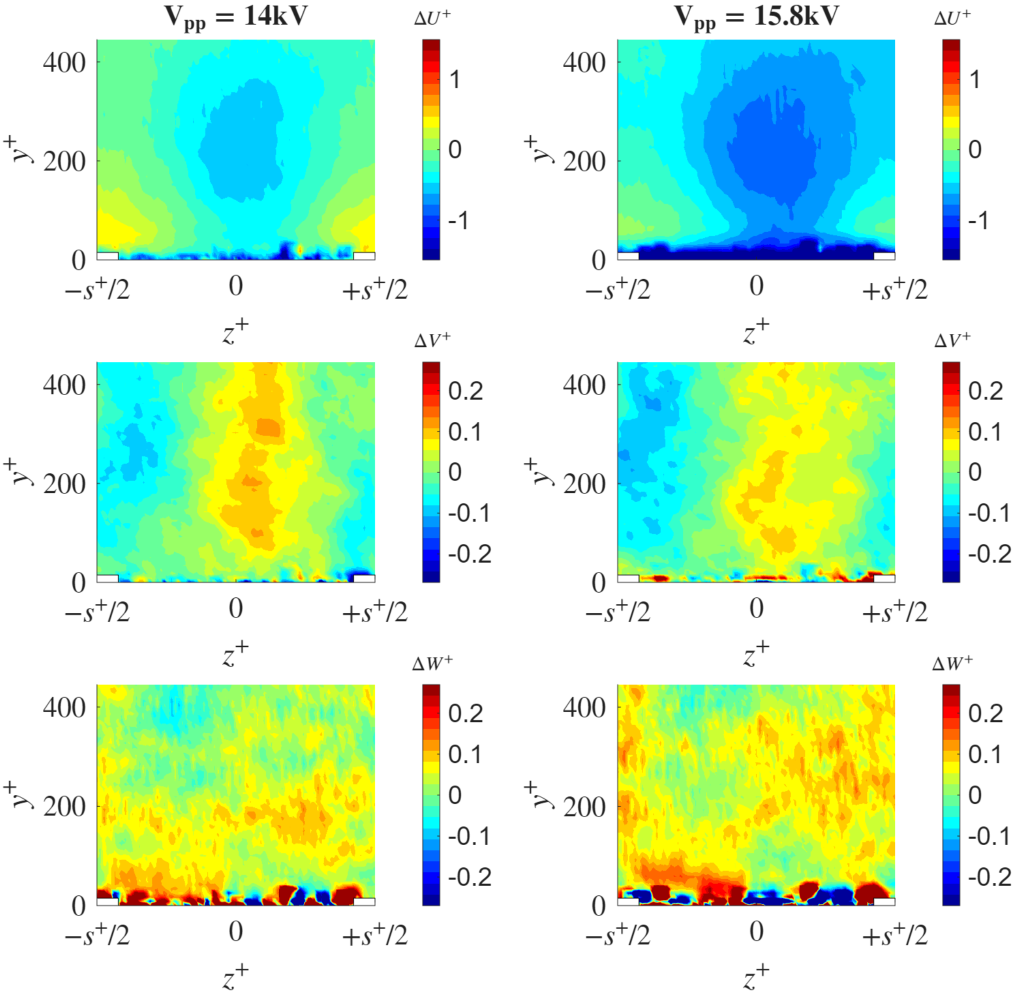

Appendix B

Voltage effect

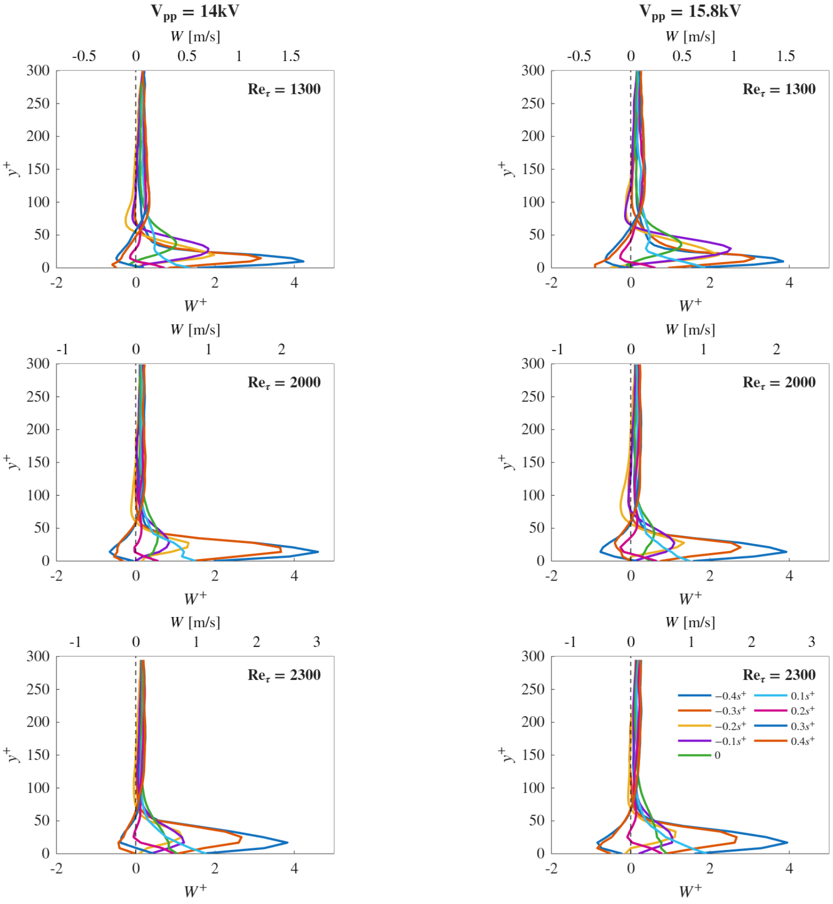

(a) Test case: $x1$ $V_{pp} = 14\ kV$.

(b) Test case: $x1$ $V_{pp} = 15.8\ kV$.

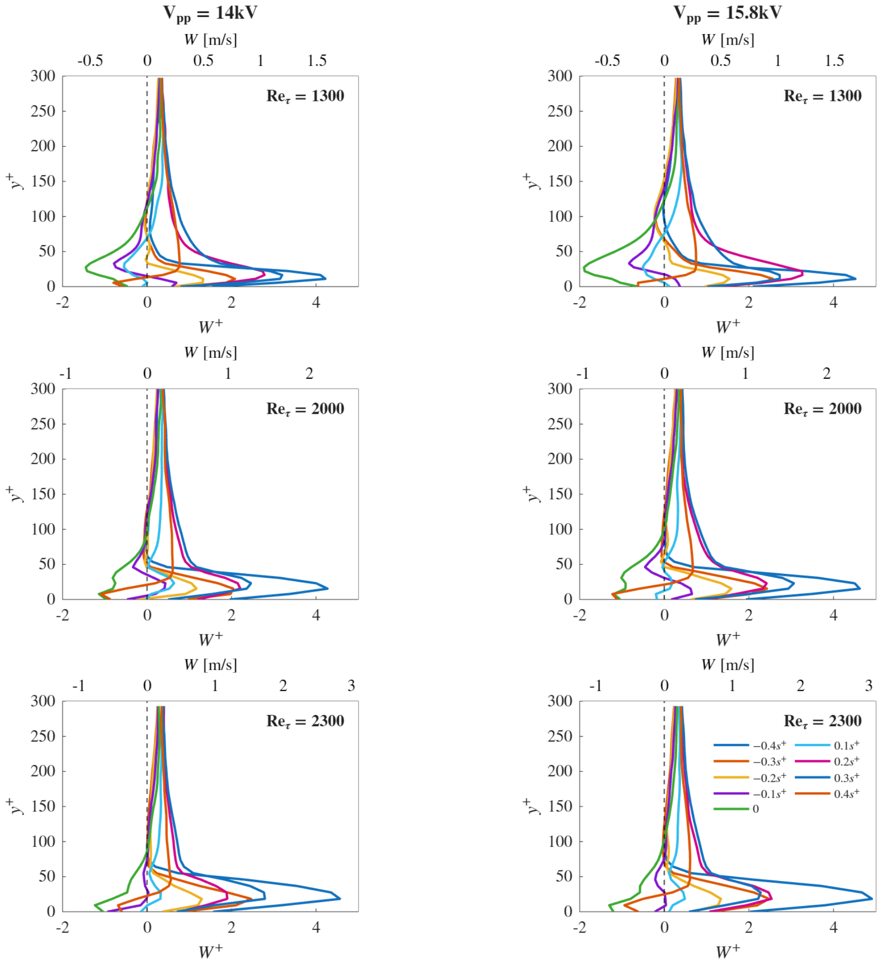

(c) Test case: $x2$ $V_{pp} = 14$ kV.

(d) Test case: $x2$ $V_{pp} = 15.8$ kV.

Figure B.1: Effects of voltage variation on the spanwise velocity profiles at $x1$ and $x2$, measured at discrete spanwise locations with a constant step of 10% of the electrode spacing (s^+).

Appendix C

Reynolds Stresses

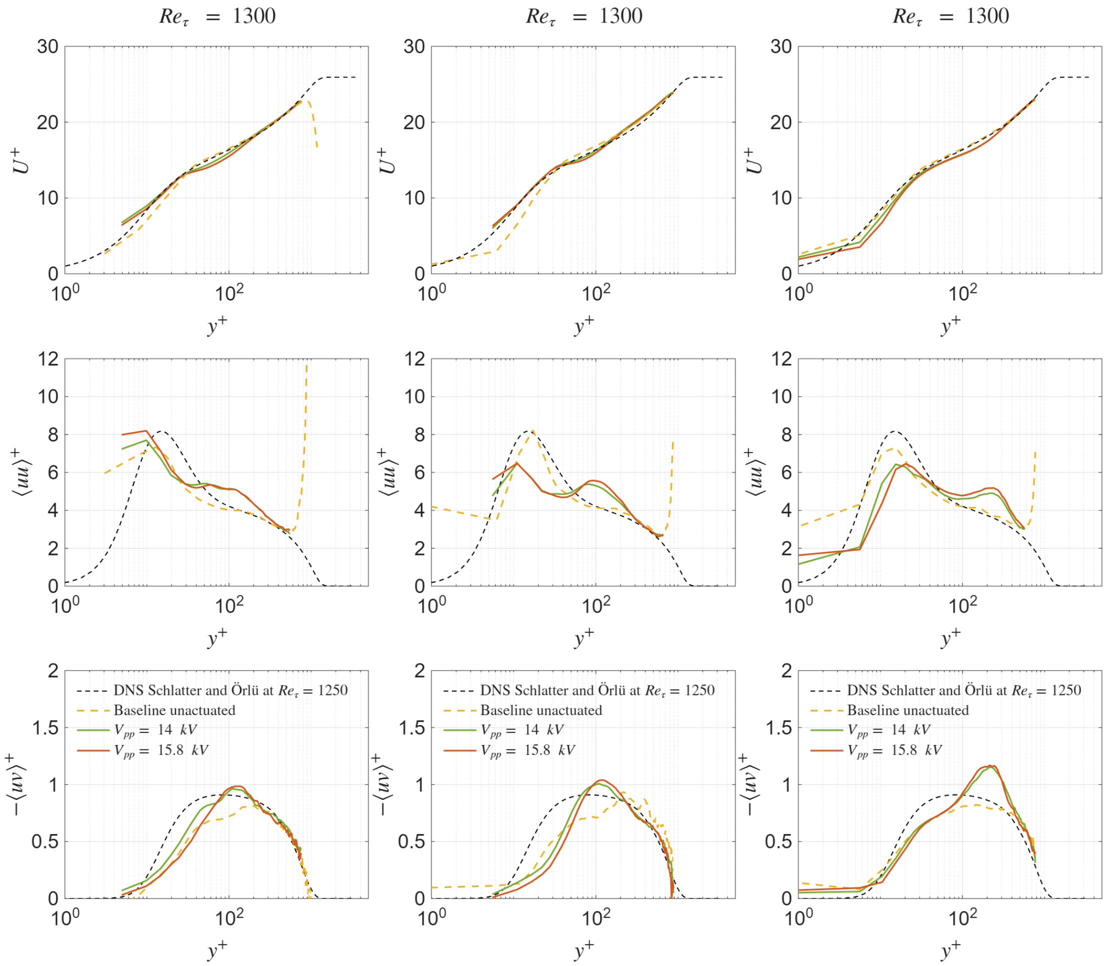

(a) Position: $x1$. **(b)** Position: $x2$. **(c)** Position: *Downstream*.

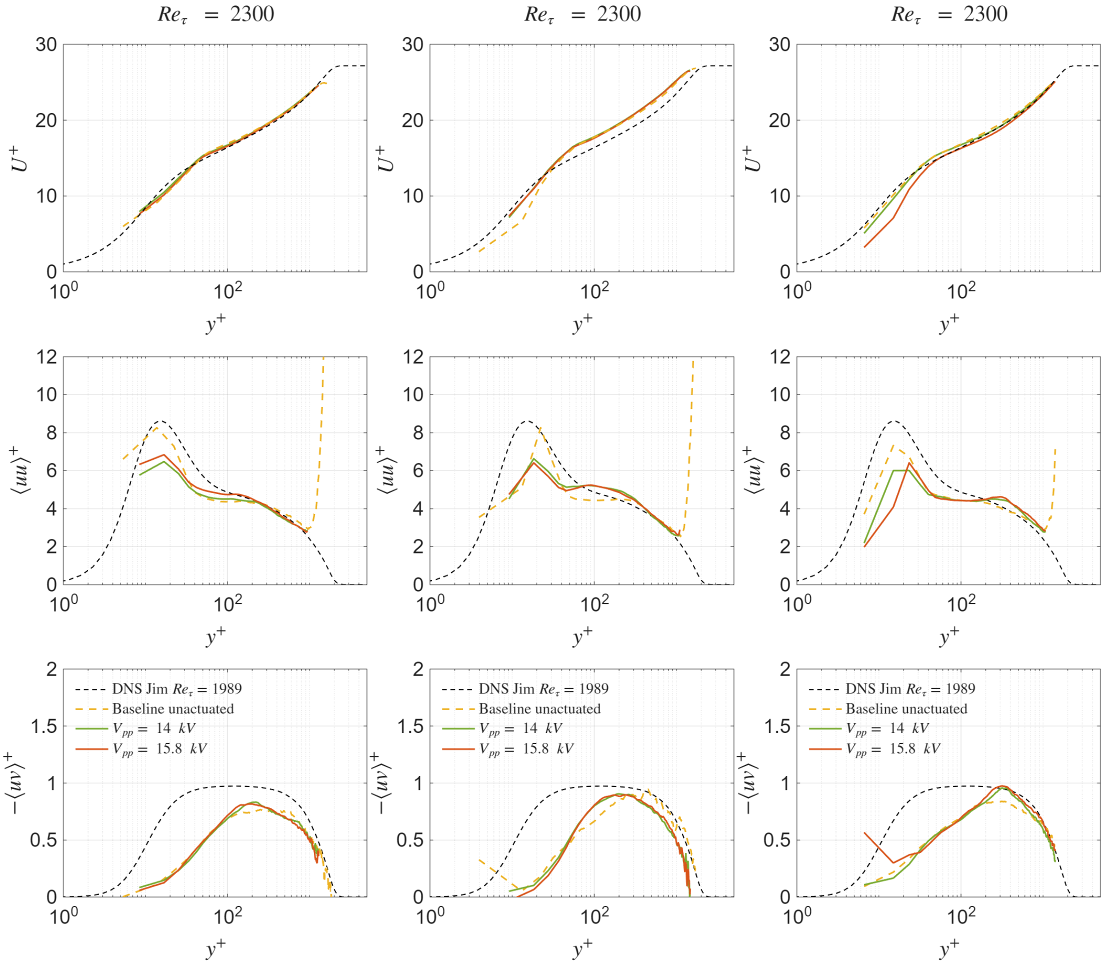

(d) Position: $x1$.

(e) Position: $x2$.

(f) Position: *Downstream*.

Figure C.1: Dimensionless mean velocity profiles and $\overline{uu}^+$ and $-\overline{uv}^+$ Reynolds stresses components at different streamwise positions for a fixed friction Reynolds number (a,b,c) $Re_\tau = 1300$ and (d,e,f) $Re_\tau = 2300$. The black dashed linerepresents the reference DNS data, and the yellow one denotes the no-plasma case at the corresponding Reynolds number. All profiles are normalized using the viscous scales of the unactuated case.

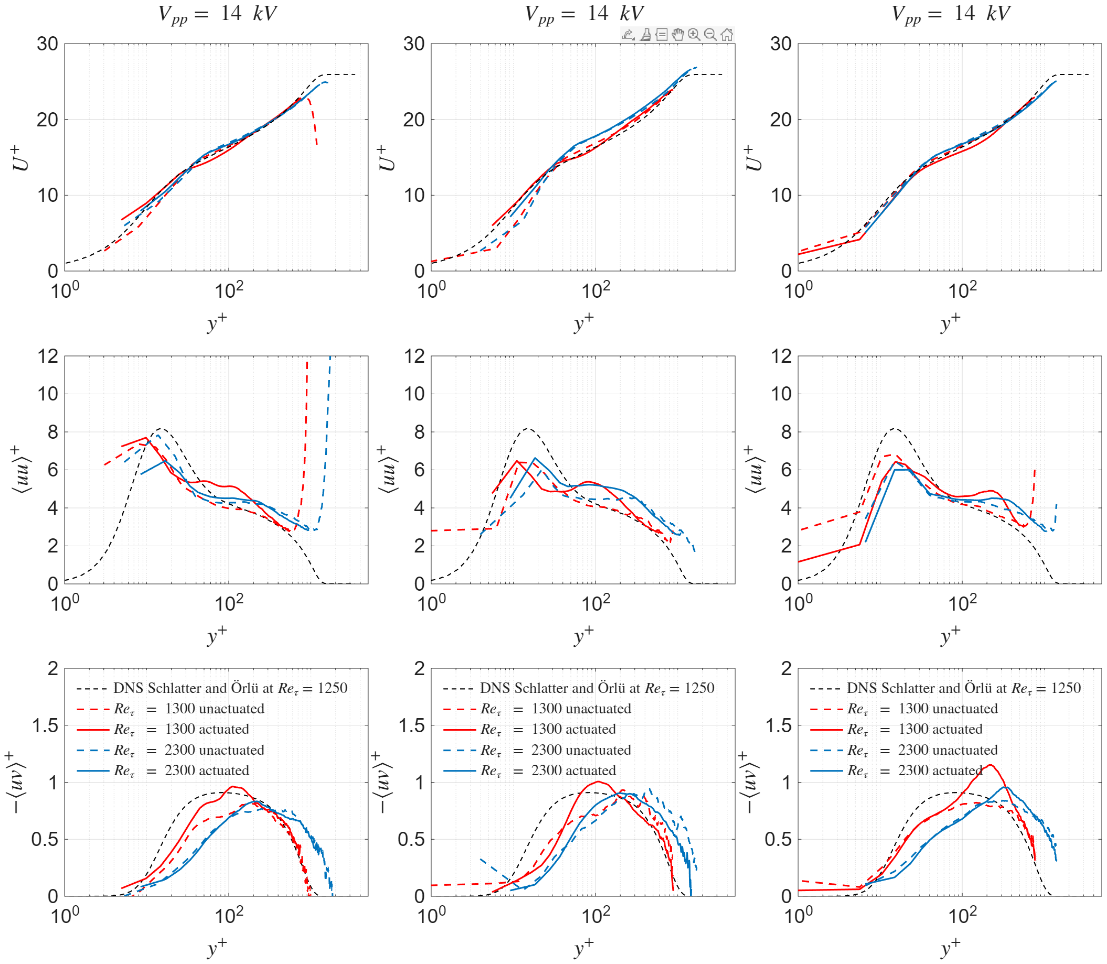

(g) Position: $x1$. **(h)** Position: $x2$. **(i)** Position: $Downstream$.

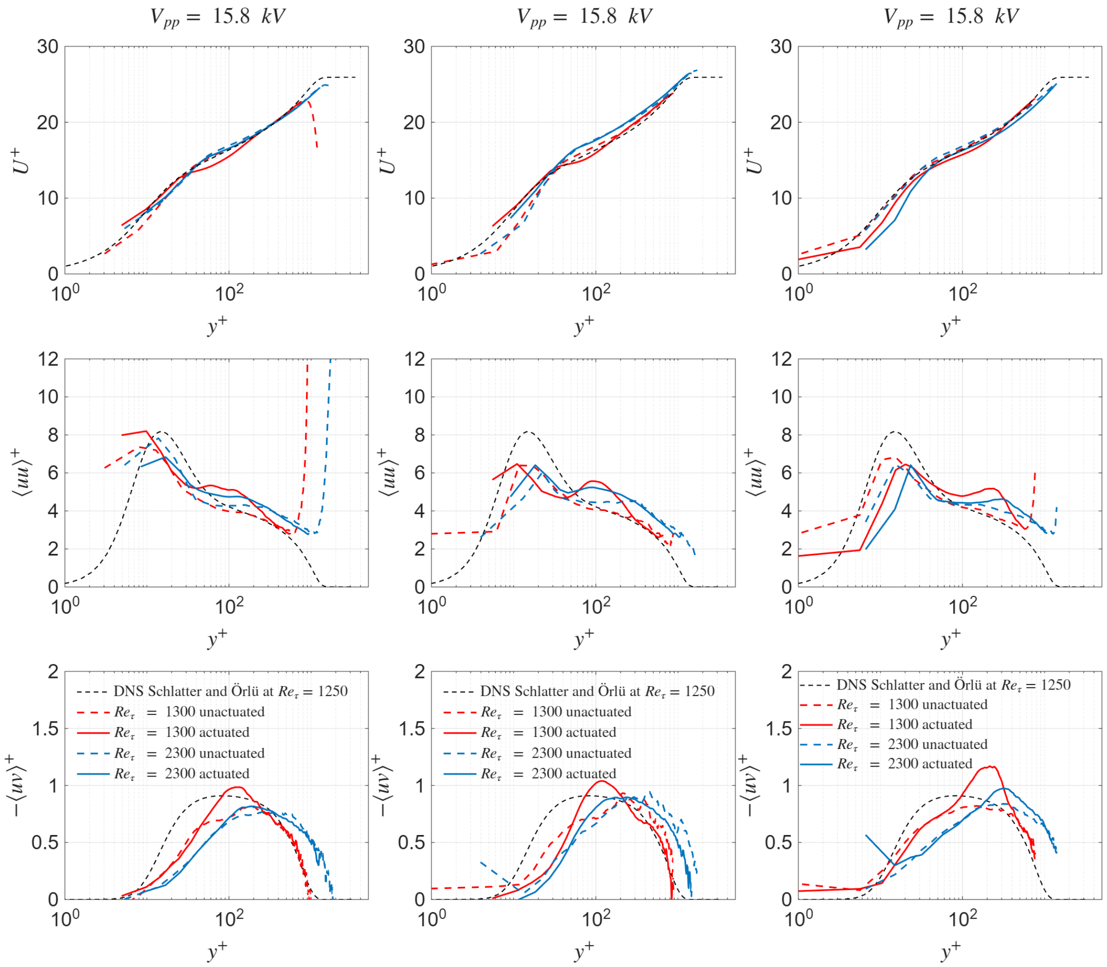

(j) Position: $x1$. **(k)** Position: $x2$. **(l)** Position: $Downstream$.

Figure C.2: Dimensionless mean velocity and Reynolds stresses profiles at different streamwise positions, comparing different friction Reynolds numbers (Re_τ) at fixed peak-to-peak voltages. (a,b,c) Profiles at V_{p-p} = 14 kV; (d,e,f) profiles at V_{p-p} = 15.8 kV. In each plot, results for Re_τ = 1300 and Re_τ = 2300 are compared. The black dashed line (–) represents the reference DNS data, while the colored dashed lines denote the corresponding unactuated (no-plasma) cases for each Reynolds number. All profiles are normalized using the viscous scales of the respective unactuated case.

Bibliography

[1] Advisory Council for Aviation Research and Innovation in Europe (ACARE). *Flightpath 2050: Europe's Vision for Aviation.* Brussels: European Commission, 2011 (cit. on p. 1).

[2] S. A. Jones. *VII. Boundary Layer Flows.* Study Guide, Louisiana Tech University. n.d. (Cit. on p. 3).

[3] Hermann Schlichting and Klaus Gersten. *Boundary-Layer Theory.* 9th. With contributions from Egon Krause and Herbert Oertel Jr. Translated by Katherine Mayes. Berlin, Heidelberg: Springer-Verlag, 2017. ISBN: 978-3-662-52917-1. DOI: `10.1007/978-3-662-52919-5` (cit. on p. 4).

[4] James M. Wallace. «Quadrant Analysis in Turbulence Research: History and Evolution». In: *Annual Review of Fluid Mechanics* 48.1 (2016), pp. 131–158. DOI: `10.1146/annurev-fluid-122414-034550` (cit. on p. 5).

[5] Donald Coles. «The law of the wake in the turbulent boundary layer». In: *Journal of Fluid Mechanics* 1.2 (1956), pp. 191–226 (cit. on p. 6).

[6] J. I. Choi, C. X. Xu, and H. J. Sung. «Drag reduction by spanwise wall oscillation in wall-bounded turbulent flows». In: *AIAA Journal* 40.5 (2002) (cit. on p. 8).

[7] M. Quadrio and P. Ricco. «The laminar generalized Stokes layer and turbulent drag reduction». In: *Journal of Fluid Mechanics* 667 (2011), pp. 135–157 (cit. on p. 8).

[8] Jinjun Wang and Lihao Feng. *Flow Control Techniques and Applications.* Vol. 46. Cambridge Aerospace Series. Cambridge, UK: Cambridge University Press, 2018 (cit. on pp. 9, 10, 13).

[9] Mihailo R. Jovanović and Bassam Bamieh. «Componentwise energy amplification in channel flows». In: *Journal of Fluid Mechanics* 534 (2005), pp. 145–183 (cit. on p. 11).

[10] A. Baron and M. Quadrio. «Turbulent Drag Reduction by Spanwise Wall Oscillations». In: *Applied Scientific Research* 55 (1996), pp. 311–326 (cit. on p. 11).

[11] Yunlun Du and George Em Karniadakis. «Suppressing wall turbulence by means of a transverse traveling wave». In: *Science* 288.5469 (2000), pp. 1230–1234 (cit. on p. 11).

[12] Maurizio Quadrio, Pierre Ricco, and Claudio Viotti. «Streamwise-traveling waves of spanwise wall velocity for turbulent drag reduction». In: *Journal of Fluid Mechanics* 627 (2009), pp. 161–178 (cit. on pp. 11, 12).

[13] F. Auteri, A. Baron, M. Belan, G. Campanardi, and M. Quadrio. «Experimental assessment of drag reduction by traveling waves in a turbulent pipe flow». In: *Physics of Fluids* 22.11 (2010), p. 115103 (cit. on p. 12).

[14] Max W. Knoop, Rahul Deshpande, Ferry F. J. Schrijer, and Bas W. van Oudheusden. «Response of a turbulent boundary layer to steady, square-wave-type transverse wall-forcing». In: *Physical Review Fluids* 10.6 (2025), p. 064607 (cit. on p. 12).

[15] Timothy N. Jukes, Kwing-So Choi, Graham A. Johnson, and Simon J. Scott. «Turbulent Boundary-Layer Control for Drag Reduction Using Surface Plasma». In: *Proceedings of the 3rd AIAA Flow Control Conference*. American Institute of Aeronautics and Astronautics, 2004 (cit. on p. 14).

[16] Kwing-So Choi, Timothy Jukes, and Richard Whalley. «Turbulent boundary layer control with plasma actuators». In: *Philosophical Transactions of the Royal Society A: Mathematical, Physical and Engineering Sciences* 369.1940 (2011), pp. 1443–1458 (cit. on pp. 14–16).

[17] H. Zong, Z. Su, H. Liang, and Y. Wu. «Experimental investigation and reduced-order modeling of plasma jets in a turbulent boundary layer for skin-friction drag reduction». In: *Physics of Fluids* 34.8 (2022) (cit. on pp. 16–18).

[18] N. Benard, E. Moreau, and J. P. Bonnet. «Drag Reduction by Wall-Parallel Standing Wave with Plasma Actuator». In: *AIAA SCITECH 2024 Forum*. Orlando, FL: American Institute of Aeronautics and Astronautics, Jan. 2024 (cit. on pp. 18–20).

[19] Markus Raffel, Christian E. Willert, Steven T. Wereley, and Jürgen Kompenhans. *Particle Image Velocimetry: A Practical Guide*. 2nd. Experimental Fluid Mechanics. Springer, 2007 (cit. on pp. 23, 26).

[20] Eduardo Rodriguez-Lopez, Paul J. K. Bruce, and Oliver R. H. Buxton. «A robust post-processing method to determine skin friction in turbulent boundary layers from the velocity profile». In: *Experiments in Fluids* 56 (2015) (cit. on p. 32).

[21] Alessandro Gallo. «Characterization of dielectric barrier discharge plasma actuators for drag reduction». Master Degree Thesis in Aerospace Engineering. MA thesis. Torino, Italia: Politecnico di Torino, 2025. URL: `https://webthesis.biblio.polito.it/38552/` (cit. on pp. 33, 35).